Atomically Thin Spatial Light Modulators with Excitonic Nanomaterials

Thesis by

Melissa Li

In Partial Fulfillment of the Requirements for

the degree of

Doctor of Philosophy

CALIFORNIA INSTITUTE OF TECHNOLOGY

Pasadena, California

2025

(Defended February 3, 2025)

Melissa Li
ORCID: 0000-0003-1534-4191

ACKNOWLEDGEMENTS

This thesis would not have been possible without the support and guidance of many individuals. I am deeply grateful to be surrounded by incredible people who have profoundly shaped my scientific journey.

First and foremost, I would like to thank my advisor, Professor Harry Atwater, for being a constant source of inspiration throughout my PhD. His remarkable breadth and depth of knowledge across so many areas of science, combined with his creativity in approaching problems, have shaped my development as a researcher. His guidance, patience, and support have been invaluable at every step of my PhD.

Second, I would like to thank Professor Vladimir Bulović, who was my undergraduate academic advisor and MEng thesis advisor at MIT. His mentorship sparked my early interest in research and helped lay the foundation for my academic pursuits.

I am incredibly thankful for the opportunities to be mentored by an exceptional group of colleagues in the Atwater Group. Several postdocs and graduate students generously shared their knowledge and time with me. A special acknowledgement goes to Claudio Hail, Lior Michaeli, Souvik Biswas, and Cora Went—I deeply appreciate their mentorship during my time at Caltech. Claudio and Lior have been excellent collaborators and I learned a great deal about optics and metasurfaces from them. Souvik and Cora guided me through the complexities (and frustrations) with 2D materials and I am grateful for their scientific and emotional support throughout my PhD. Cora's remarkable talent for story telling through visually engaging presentations and her dedication to advocacy are qualities I deeply admire and aspire to embody, both within and beyond the realm of science. Other senior colleagues I have also had the pleasure of learning from include Ruzan Sokhoyan, Phil Jahelka, Minseok Jang, Haley Bauser, Joeson Wong, Hamidreza Akbari, and others. I would also like to thank other current members of the 2D working group (Holland Frieling, Samuel Seah, Rachel Tham, Miles Johnson), metasurface working group (Jared Sisler, Prachi Thureja, Julie Belleville, Morgan Foley, Martin Thomaschewski), and the quantum nanophotonics working group (Komron Shayegan, Arun Nagpal, Kristina Malinowski, Ramon Gao, Yae-Chan Lim)

for fruitful discussions. I am also grateful for my officemates Cora Went, Areum Kim, Laura Kim, Lily Shiau, and Susana Torres-Londono for making Watson 252 such a fun and lively place to work.

I would like to thank the administrative assistants, both in and outside of the Atwater group, who keep Watson running, specifically Kamaljit Flower, Thomasine Murphy, Christine Jenstad, and Jennifer Blankenship. Beyond the lab, I am grateful to the people I worked with across Caltech: my fellow members of the Graduate Student Council, my colleagues in the Resident Associate program, and administrators that I collaborated with on various advocacy efforts.

Finally, I would like to thank my family for their unconditional love, support, and encouragement. My mom, who is also my best friend, is the kindest, most selfless person I know, and I am so fortunate to have her as my role model throughout my life. I would also like to thank my dad and Roger, my husband, for their relentless efforts in keeping my mind sharp, whether I wanted them to or not. I'll never forget the fond childhood memories of mental math quizzes with my dad that always ended in tears; Roger has now taken over that role, though it only occasionally ends in tears. They never let me give up on solving a problem, instilling perseverance and critical thinking while also keeping me humble. Last, but not least, I would like to thank my rambunctious dog, Brownie, who's been by my side for over 15 years. I am incredibly blessed to have a family whose love and unwavering support continue to uplift and inspire me every day.

ABSTRACT

Achieving active control of light at the ultimate thickness limit—a single atomic layer—offers unprecedented opportunities for next-generation optoelectronic devices. The quest for ultrathin spatial light modulators has long relied on integrating tunable materials with plasmonic or high-index nanoantennas that serve as small, but three-dimensional optical resonators. As structures for controlling light become increasingly complex and compact, the geometrical constraints of these three-dimensional resonators will ultimately limit their scalability and versatility. A new avenue for device miniaturization emerges when harnessing electrically tunable resonances that are intrinsic to atomically thin materials.

This thesis explores how exciton resonances, specifically in two-dimensional (2D) van der Waals materials, can serve as the central building blocks for future spatial light modulators that are as thin as atoms. We start by characterizing the gate-tunable optical properties of a monolayer molybdenum diselenide ($MoSe_2$), a 2D transition metal dichalcogenide. By tuning the exciton resonances with voltage, we demonstrate over 200% modulation in the real and imaginary part of the complex refractive index. We attribute this large tunability to the interplay between radiative and nonradiative decay channels of the excitons. The index modulation gives rise to amplitude and phase modulation of the scattered light, which is then used to engineer an electrically tunable phase gradient across a single monolayer $MoSe_2$ flake to dynamically steer the reflected beam.

Next, we present a theoretical analysis of the complex frequency response of a generalized excitonic heterostructure. We show how the spectral positions of the phase singularities, e.g. zeros and poles, can be dynamically controlled, their impacts on the real frequency phase response, and how they can be used in active metasurface design. Finally, we evaluate excitons in quantum dots as an alternative platform for room temperature optical modulators and show how they present different challenges in designing phase modulators.

Overall, our work highlights the novel functionalities enabled by exciton resonances for advanced light manipulation, underscoring their potential for atomically thin light modulators.

PUBLISHED CONTENT AND CONTRIBUTIONS

Portions of this thesis have been drawn from the following publications:

*indicates equal contribution

1. **M. Li**, Q. Li, M. L. Brongersma, H. A. Atwater. Optical devices as thin as atoms. *Science* 386, 1226-1228 (2024). DOI:10.1126/science.adk7707
   All authors conceived the project and contributed equally. All authors wrote the manuscript.

2. **M. Li**, L. Michaeli, H. A. Atwater. Electrically tunable topological singularities in excitonic two-dimensional heterostructures for wavefront manipulation. *ACS Photonics* 11 (9), 3554-3562 (2024). DOI: 10.1021/acsphotonics.4c00397
   ***M.L.** performed the simulations, led the data analysis and modelling, and wrote the manuscript.*

3. **M. Li***, C. U. Hail*, S. Biswas, H. A. Atwater. Excitonic beam steering in an active van der Waals metasurface. *Nano Letters* 23 (7), 2771-2777 (2023). DOI:10.1021/acs.nanolett.3c00032
   ***M.L.** fabricated the samples, carried out the measurements, performed the simulations, led the data analysis and modelling, and wrote the manuscript.*

4. **M. Li**, S. Biswas, C. U. Hail, H. A. Atwater. Refractive index modulation in monolayer molybdenum diselenide. *Nano Letters* 21 (18), 7602-7608 (2021). DOI:10.1021/acs.nanolett.1c02199
   ***M.L.** fabricated the samples, carried out the measurements, performed the simulations, led the data analysis and modelling, and wrote the manuscript.*

In preparation

5. **M. Li**, J. Sisler, H. A. Atwater. Excitons in colloidal quantum dots for emission and phase modulation. *In preparation* (2025)
   ***M.L.** fabricated the samples, carried out the measurements, performed the simulations, led the data analysis and modelling, and wrote the manuscript.*

TABLE OF CONTENTS

LIST OF ILLUSTRATIONS AND/OR TABLES

CHAPTER 1: INTRODUCTION

Spatial Light Modulators with Metasurfaces

Controlling light propagation has guided human innovation for centuries. The seemingly simple act of bending light through a curved piece of glass introduced the lens, which opened up new scientific frontiers. Lenses soon evolved into microscopes that unveiled the previously hidden cellular world and telescopes that gave us a glimpse of distant galaxies. Over time, these optical technologies have become increasingly complex, yet dramatically smaller, driving researchers to push beyond the traditional limits of bulky lenses. Now, as we enter an era of extreme miniaturization, the question naturally arises in optics: *Is there a limit to how far we can push the thickness of optical devices? Can they be reduced down to a few layers of atoms?*

Conventional optical elements, such as lenses, are governed by light refraction and propagation over a bulk media in order to shape the flow of light. Therefore, the functional properties of these traditional optical structures are linked to their inherent three-dimensional (3D) shape. In contrast, metasurfaces employ patterned nanostructures that interact strongly with light and alter the optical properties over a subwavelength thickness (Figure 1.1a).

The governing principles of metasurfaces can be traced back to Huygens principle, which states that every point on a wavefront can be treated as a source of spherical waves and the interference from these different points form a new wavefront (Figure 1.1b). When the interface between two media is artificially structured in order to introduce a phase discontinuity along the light path, the equations for Snell's law need to be modified to account for the phase shift that is a function of the position along the interface. Conventionally, the equations for reflection and refraction based on Snell's law are given by

$$\sin\theta_r - \sin\theta_i = 0$$

$$n_t \sin\theta_t - n_i \sin\theta_i = 0$$

where θ_i, θ_r, and θ_t are the incident, reflected, and refracted angles of propagation and n_i and n_t are the refractive indices of the two media. With the introduction of a phase gradient along the interface, we rewrite this equation account for the accumulated phase as a function of position. This yields the generalized Snell's law for reflection and refraction:

$$\sin\theta_r - \sin\theta_i = \frac{\lambda_0}{2\pi n_i}\frac{d\Phi}{dx}$$

$$n_t \sin\theta_t - n_i \sin\theta_i = \frac{\lambda_0}{2\pi}\frac{d\Phi}{dx}$$

where $\frac{d\Phi}{dx}$ is the phase gradient along the interface (Figure 1.1b). In order to realize this phase gradient, resonant nanophotonic elements are required. In the seminal work by Yu et al.[1] (Figure 1.2), different v-shaped metallic structures are used to create different phases of light based on the angle between arms of the resonator. The array of these metallic nanostructures then redirects the transmitted light to a desired angle that satisfies the generalized Snell's law.

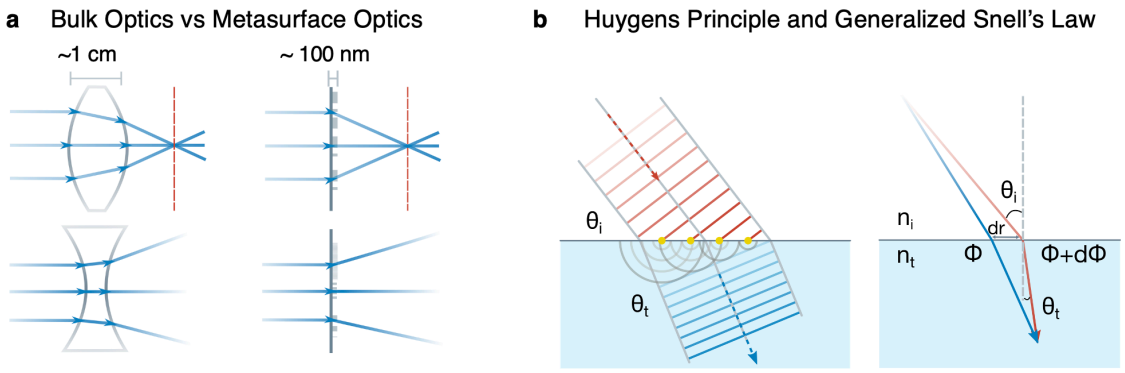

Figure 1.1. Principles of bulk optics and metasurface optics. (a) Conventional bulk optics (lens) relies on refraction to bend light, while metasurface based optics bends light to do the scattering of patterned nanoparticles. While both enable focusing or defocusing of light, metasurfaces are many orders of magnitude thinner. (b) The governing principles of metasurface based flat optics derives from Huygens principle and generalized Snell's law.

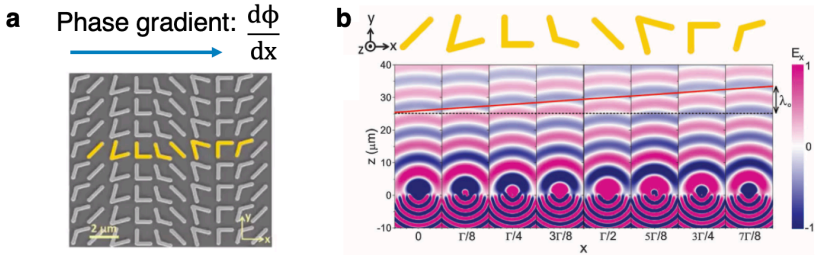

Figure 1.2. Phase gradient metasurface for beam deflection. (a) Nanoantenna array of a plasmonic metasurface consisting of a unit cell of eight v-shaped nanostructures, giving rise to a phase gradient along the x-direction. (b) Following Huygen's principle, the superposition of the spherical waves scattered by the antennas results in a refracted beam to a desired angle that satisfies the generalized Snell's law. The tilted red line is the envelope of the projections of these spherical waves. Adapted from Yu et al.[1]

Most metasurfaces currently employ geometrical plasmon and Mie resonances in metal and semiconductor nanostructures whose shapes are carefully engineered to control their light scattering properties[1,2]. By exciting their optical resonances, one can control the amplitude, phase, wavelength, and polarization of the scattered light. However, a major challenge arises when attempting to dynamically tune their scattering behavior because their shapes are fixed after fabrication and typically only weak index modulation are available for tuning.

To achieve truly complete control of radiation, there is need to develop active nanophotonic structures that can control the different properties of light, all as a function of time. A number of emerging nanophotonics and metasurface applications need to deliver dynamic wavefront control. For example, electrically tunable phased array metasurfaces can enable high-speed beam steering and focusing for light detection and ranging (LiDAR) systems, reconfigurable holography, virtual and augmented reality, visible light-based wireless communication (Li-Fi), and thermal radiation management. The tunability limitations of geometrical resonances in realizing dynamic metasurfaces raise the intriguing question whether there are other equally strong, but intrinsically more tunable resonances we can harness. Fortunately, new opportunities emerge when the structural dimensions of

scattering elements are pushed to the ultimate atomic-scale limit, where quantum size effects significantly alter their optical properties. Several very strong resonances arise from intrinsic material properties that can be utilized in the design of metasurfaces to achieve conceptually new ways to structure and dynamically manipulate optical wavefronts.

Van der Waals Materials for Active Metasurfaces

2D van der Waals materials—stacked atomically thin sheets of semimetals, semiconductors or insulators—host a variety of intriguing phenomena and exotic optical properties that are not found in bulk materials. Counterintuitively, these ultrathin layered materials can strongly interact with light, as they support a variety of material resonances whose nature can be traced back to their quantum-confined electronic and phononic states. These states can provide resonances spanning from the ultraviolet to the mid-infrared and are highly tunable by external stimuli, such as electric and magnetic fields, strain, carrier injection, electrochemical potential, and other environmental features that affect the refractive index. This realization has prompted the question whether it is advantageous to create dynamic metasurfaces from van der Waals materials.

Among them, 2D semiconductors, such as monolayer transition metal dichalcogenides (TMDCs) and black phosphorus[3], have gained prominence by offering more comprehensive light-field control beyond absorption (Figure 1.3)[4–7]. They support exciton resonances (i.e., tightly bound electron-hole pairs) at room temperature due to their large binding energy that results from a reduced dielectric screening and enhanced quantum confinement[8]. The large oscillator strength of excitonic resonances and the ability to reduce carrier-carrier scattering enable efficient coherent light manipulation, leading to near-unity reflection at cryogenic temperatures[9,10]. Given the rapid advances in the large-scale synthesis and patterning of these materials, it is now possible to fashion van der Waals materials into practical metasurfaces.

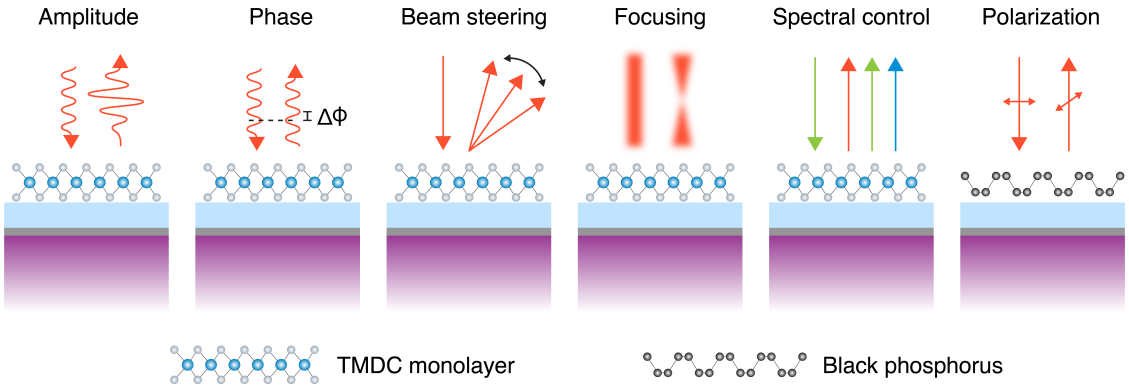

Figure 1.3. Schematic of 2D heterostructures enabling dynamic wavefront shaping. Optical functions enabled by 2D heterostructures include control of amplitude, phase, active beam steering, focusing, wavelength selectivity, and polarization conversion.

Atomically-thin metasurfaces follow different design principles than their conventional 3D counterparts. Rather than manipulating the geometric shape of scatterers and controlling the way light resonates inside, the focus here is on understanding the electronic or phononic bandstructure of the 2D sheets and the relevant excited electronic states. Figure 1.4a illustrates a simplified exciton band diagram for TMDC monolayers in which relevant decay channels for excited excitons are depicted. Similar to the photons trapped inside optical nanoresonators, excitons can decay either radiatively (γ_{r}) or non-radiatively (γ_{nr}). The latter is the sum of contributions from exciton-electron scattering ($\gamma_{\mathrm{nr-e}}$), intravalley and intervalley exciton-phonon scattering ($\gamma_{\mathrm{nr-KK}}$ and $\gamma_{\mathrm{nr-KQ}}$), as well as the defect-assisted decay ($\gamma_{\mathrm{nr-def}}$). Here, the quasiparticle energy gap $E = \hbar\omega$ and the total decay rate $\gamma_{\mathrm{tot}} = \gamma_{\mathrm{r}} + \gamma_{\mathrm{nr}}$ determine the resonant frequency ω and the "quality factor" of the optical resonance $Q = \omega/\gamma_{\mathrm{tot}}$ used for structuring the wavefront, while the scattering efficiency of the "resonator" is dictated by the ratio between the desired radiative and total decay rates $\eta = (\gamma_{\mathrm{r}}/\gamma_{\mathrm{tot}})^2$.

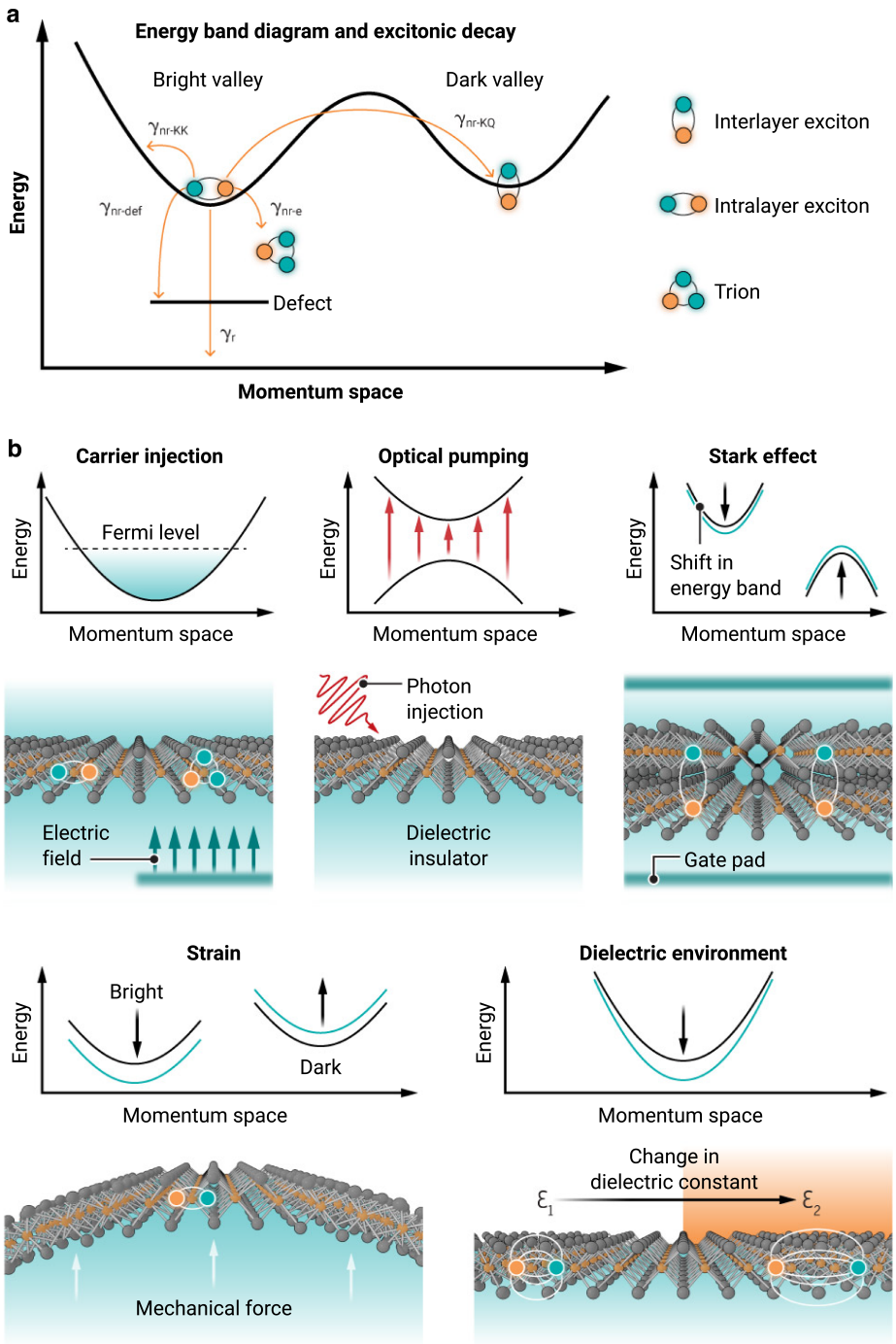

Figure 1.4. Exciton tuning mechanisms. (a) Simplified exciton (quasiparticle) band diagram showing the different radiative (γ_r) and nonradiative (γ_{nr}) decay rates that can be engineered through various tuning mechanisms. (b) Band diagram and schematic of the electro-optic effects available for tuning in TMDCs.

Tuning Exciton Resonances

The real excitement comes in identifying the various ways to dynamically tune the resonant frequencies and linewidths of these exciton resonances, which enable creation of ultra-compact and energy-efficient dynamic platforms for manipulating light fields at unparalleled speeds. Based on their dimensionality and sub-nanometer thickness, 2D semiconductors are much more easily tuned since external electric fields are unscreened at the material surface, resulting in very sensitive responses to changes in the surrounding environment. Thus, a range of externally stimulated dynamic light-matter interaction phenomena can be explored (Figure 1.4b). First, excitonic resonances can be electrically damped by free carrier injection, which results from the enhanced non-radiative decay via electron-exciton scattering or trion formation. Free carrier injection can also reduce radiative decay as the carriers can also screen the electron-hole attraction efficiently. The linewidth broadening, intensity reduction, and spectral shifts of exciton resonances induced by the presence of free carriers can give rise to large refractive index modulation near their resonant frequencies[11] at gigahertz speeds[12], showing great potential for amplitude and phase modulation and dynamic optical wavefront shaping, including beam steering and focusing. The tunable excitonic birefringence in black phosphorus can further add polarization to the controllable degrees of freedom, allowing for comprehensive control of light[3].

The Scope of this Thesis

In Chapter 1, we provide the necessary context and background information for understanding this thesis, including the basics of phased-array metasurfaces, van der Waals materials, and excitons. We introduce ways that exciton resonances in 2D materials can be tuned and how the tunability can enable dynamic wavefront shaping, highlighting their potential for ultrathin light modulators.

In Chapter 2, we demonstrate over 200% modulation in the real and imaginary part of the refractive index of a TMDC by electrically gating the monolayer flake. We also show how

this large index modulation gives rise to both amplitude and phase modulation of the reflected light.

In Chapter 3, we introduce an atomically thin beam steering device based on a monolayer TMDC operating at cryogenic temperatures. Building on the work presented in Chapter 2, we show how we can apply an electrically tunable phase gradient across a single monolayer flake, allowing us to dynamically steer the reflected beam. We note that the phase tunability and beam steering were achieved in absence of nanoantennas or other geometrical optical cavities and resulted purely from the strong intrinsic exciton resonances in the TMDC.

In Chapter 4, we provide an analysis of the complex frequency amplitude and phase response of a generalized excitonic heterostructure for metasurface applications. We present the link between spectral positions of topological phase singularities in the complex frequency plane and their effects on the real frequency phase. We then demonstrate how these singularities corresponding to zeros and poles can be actively tuned with voltage by using a material with tunable exciton resonances. These results are then extended to study beam steering configurations, where we show how complex frequency analysis can provide valuable insight in device design considerations.

In Chapter 5, we evaluate quantum dots as an alternative platform for room temperature emission and phase modulators. While we observe high PLQY and notable emission modulation, we see limited reflectance amplitude and phase modulation. We then highlight key differences between excitons in quantum dots and TMDCs and how these differences play an important role in designing phase modulators with quantum dots.

In Chapter 6, we present an outlook for the emerging field of nanomaterials for active metasurfaces, discuss ongoing challenges, and suggest future research directions.

The synergy of 2D materials and metasurfaces remains largely unexplored and their potential is just starting to be uncovered for new scientific discovery. This thesis explores how tuning the exciton resonances in these atomically thin materials will play a pivotal

role in defining a new frontier towards achieving versatile wavefront control at the ultimate thickness limit.

CHAPTER 2: REFRACTIVE INDEX AND PHASE MODULATION IN MONOLAYER MOLYBDENUM DISELENIDE

Two-dimensional transition metal dichalcogenides are promising candidates for ultrathin light modulators due to their highly tunable excitonic resonances at visible and near-infrared wavelengths. At cryogenic temperatures, large excitonic reflectivity in monolayer molybdenum diselenide ($MoSe_2$) has been shown, but the permittivity and index modulation have not been studied. In this chapter, we demonstrate large gate-tunability of complex refractive index in monolayer $MoSe_2$ by Fermi level modulation and study the doping dependence of the A and B excitonic resonances for temperatures between 4 K to 150 K. By tuning the charge density, we observe both temperature and carrier dependent epsilon-near-zero response in the permittivity and transition from metallic to dielectric near the A exciton energy. We attribute the dynamic control of the refractive index to the interplay between radiative and nonradiative decay channels that are tuned upon gating. Our results suggest the potential of monolayer $MoSe_2$ as an active material for emerging photonics applications.

Introduction

Two-dimensional (2D) materials have attracted a great deal of attention over the past decade due to the new physics that emerges as the materials transition from bulk to monolayer[13,14]. Particularly, transition metal dichalcogenides (TMDCs) such as $MoSe_2$ exhibit fundamentally distinct electronic and optical properties as the material evolves from indirect to direct band gap in the monolayer limit. As a result, the optical response of TMDC monolayers is dominated by strong excitonic resonances[8,15,16], which are highly tunable with external electric field or doping[17,18], dielectric environment engineering[17,19], and strain[20,21].

Recently, there has been considerable interest in studying active nanophotonic structures by combining tunable materials with resonant structures such as Mie resonators and phase gradient metasurfaces[22–27]. The ability to dynamically tune the complex index of an active

material in metasurfaces enables comprehensive control of the scattered wavefront. For example, transparent conducting oxide-based metasurfaces have demonstrated electrically tunable amplitude and phase modulation of reflected light[28–30]. However, these devices operate at wavelengths above 1500 nm, which limits their applications to short wavelength infrared (SWIR) optoelectronics. Extending the operating wavelengths to the visible range enables new applications to digital holography, imaging, cloaking, and virtual reality. Two-dimensional transition metal dichalcogenides are promising candidates for visible and near infrared (NIR) light modulators due to their strong tunable excitonic resonances in the visible and NIR spectral range. The suppression of the excitonic response has previously been shown to modulate the refractive index of WS_2 at room temperature, but the non-radiative broadening at room temperature limits the achievable tunability[11]. By encapsulating TMDCs with hexagonal boron nitride (hBN) to produce high quality heterostructures and operating at cryogenic temperatures, the excitonic linewidths can be narrowed by over an order of magnitude[9,31–33].

Here, we study the optical response of monolayer $MoSe_2$ at different carrier densities and cryogenic temperatures. Compared to other TMDCs, the optical properties of $MoSe_2$ at low temperatures have significantly less contributions from defects, allowing more accurate characterization of changes in the optical response. We exploit the narrow linewidths of the excitons at low temperatures and show that Fermi level control via electrical gating of carrier density gives rise to large refractive index modulation at both the A exciton and B exciton energy. At temperatures between 4 K to 150 K, we observe an epsilon-near-zero (ENZ) like regime and hence a transition from metallic to dielectric near the A exciton energy, resulting in large changes in reflectance amplitude and phase. We note that while the temperature and voltage-dependent reflectance have been previously shown[9,10], the gate-tunability of the complex refractive index has not been studied in these TMDCs at cryogenic temperatures. In applications where electro-optic modulation is used to tune the scattering response of nanophotonic structures near excitonic and geometrical resonances, it is important to characterize the complex refractive index changes accompanying the observed reflectance modulation[4,34]. Our demonstration of refractive index tunability

indicates the possibility to manipulate light with monolayer 2D materials for ultra-thin optical modulators.

Experimental Measurements of $MoSe_2$ Gate-Dependent Reflectance and Photoluminescence

We measure the gate-dependent reflectance spectra of a monolayer $MoSe_2$ device at cryogenic temperatures using a broadband white light source. The schematic and microscope image of the device are shown in Figure 2.1a and b, respectively. The device consists of an $MoSe_2$ monolayer encapsulated between top hBN (5.2 nm) and bottom hBN (25 nm), which passivates the $MoSe_2$ monolayer to enhance the carrier mobility and reduces the linewidth[31–33,35]. A bottom few layer graphene flake serves as the back electrode to control the carrier density in the $MoSe_2$. The entire heterostructure, fabricated with an all-dry transfer technique, is placed on an SiO_2/Si substrate with pre-patterned gold electrodes to contact the $MoSe_2$ and graphene. The carrier density in $MoSe_2$ is tuned by applying a gate voltage across the bottom hBN, which acts as the capacitor between the graphene and $MoSe_2$. To obtain the absolute reflectance of the TMDC heterostructure, the spectra is normalized to that of an optically thick gold layer adjacent to the sample.

The gate-dependent excitonic features of $MoSe_2$ are shown in both photoluminescence (PL) and reflectance spectra in Figure 2.1c and d, respectively. At 4 K, we observe two main features in PL that are associated with the A exciton and trion resonances at wavelengths of 757 nm and 769 nm, respectively. However, in reflectance, we observe three features associated with the A exciton, trion, and B exciton resonances. The presence of A and B excitons is attributable to the spin-orbit coupling induced valence and conduction band splitting[36]. We note that our PL spectrum does not contain a prominent B exciton feature presumably because the PL quantum yield is lower than the A exciton. Moreover, we observe two main differences in the trion features when comparing the PL and reflectance measurements. First, at 0V, we observe a stronger PL signal from the trion compared to the A exciton, whereas in reflectance, the A exciton feature is dominant. This difference is commonly seen at 4 K in $MoSe_2$ and can be explained by the low oscillator

strength of trions[37,38]. While the oscillator strength of a transition is intimately related to the radiative lifetime and PL intensity, the one-to-one correspondence is not typically observed due to the band structure and additional relaxation channels. The trion exists at a lower energy than the A and B exciton and the PL emission favors the lowest energy state. Therefore, even though the trion has low oscillator strength, and hence low absorption, when the sample is excited above the A and B exciton energy with a 532 nm laser, we see strong trion PL contribution from the relaxed A and B exciton states.

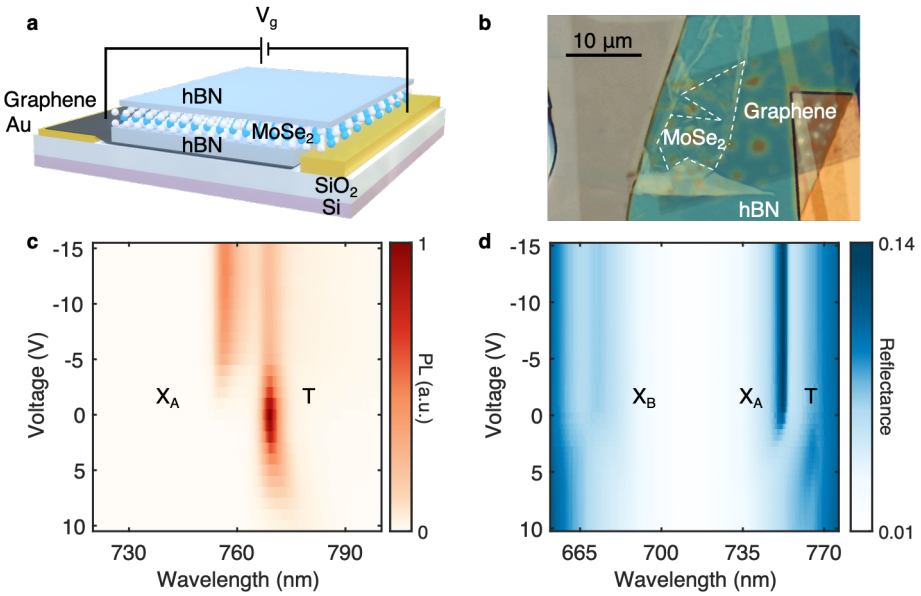

Figure 2.1. Electro-optic characterization of $MoSe_2$ heterostructure at T = 4 K. (a) Schematic of heterostructure. Carrier density in $MoSe_2$ is tuned by applying a voltage V_g across the bottom hBN. (b) Optical microscope image of the device with the monolayer region enclosed in dashed lines. (c) Gate-dependent PL spectra with a 532 nm laser showing two distinct peaks corresponding to the A exciton (X_A) and trion (T). (d) Gate-dependent reflectance spectra on the same device with three peaks corresponding to the A exciton (X_A), B exciton (X_B), and trion (T). The change in PL and reflectance can be observed in the electron-doped regime (positive voltages). To obtain the reflectance, we normalize the reflected intensity to the measured reflectance of a gold electrode.

Furthermore, we observe a difference in the energy shift direction of the trion when the sample is electron doped, which corresponds to positive voltages in our electrostatic gating scheme. In reflectance, we see that the peak energy of the trion feature blueshifts, but in PL, the peak energy redshifts. To understand this finding, we consider the different

mechanisms that can influence the reflectance and PL spectra[39–41]. Reflection can be affected by Pauli blocking upon doping, leading to an increase in the effective optical gap which results in a blueshift. However, PL involves recombination of electron-hole pairs that relax to the band edges, resulting in the Stokes shift which increases with doping[36]. Another possible explanation for this difference in the energy shifts in PL and reflectance is that the quasiparticle associated with the lower energy peak is potentially an attractive polaron instead of a trion[37,42]. However, here, we will refer to the lower energy feature as the trion for consistency.

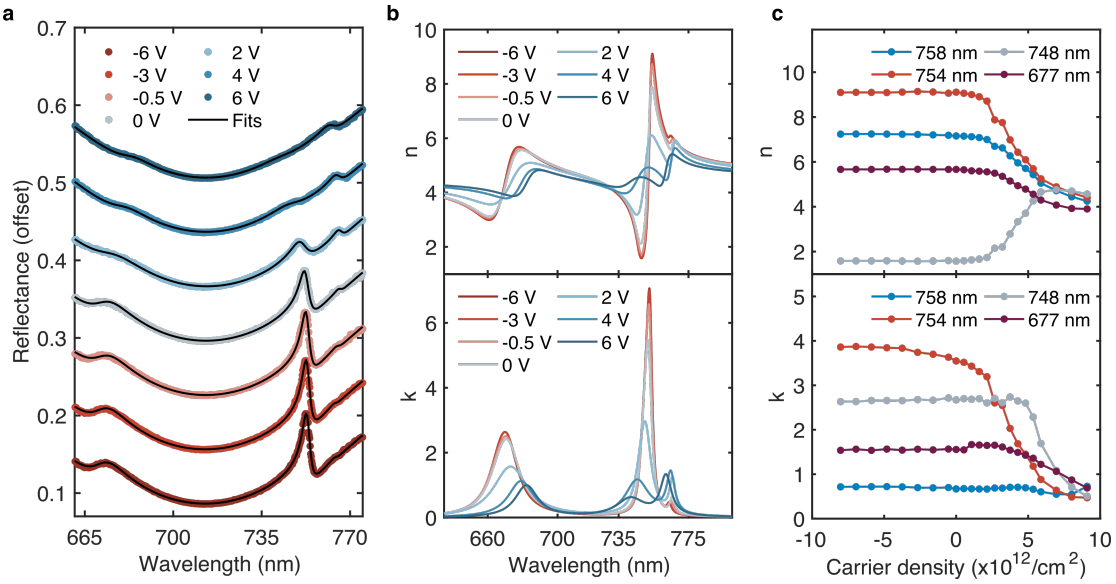

Figure 2.2. Gate-dependent reflectance spectra and refractive index at T = 4 K. (a) Reflectance spectra of monolayer $MoSe_2$ at 4 K for different gate voltages. The colored points are experimental data from line cuts of different voltages from Figure 2.1d. The solid black lines are fits from transfer matrix calculations where the $MoSe_2$ dielectric function is modeled using the multi-Lorentzian model. The spectrum corresponding to -6V shows the absolute reflectance values and the spectra at higher voltages are offset for clarity. (b) Fitted real (n) and imaginary (k) part of the refractive index with different voltages. (c) Change in the real and imaginary part as a function of electron carrier density for four different wavelengths.

Complex Refractive Index Modulation with Voltage and Carrier Density

We obtain the complex refractive index for $MoSe_2$ by using a Kramers-Kronig consistent analysis and fitting the reflectance spectra of our entire heterostructure stack with the

transfer matrix method to account for interference effects. We begin our analysis by modeling the dielectric function of the monolayer as a sum of Lorentz oscillators[43]:

$$\tilde{\epsilon} = \epsilon_1 + i\epsilon_2 = \epsilon_\infty + \sum_j \frac{f_j}{E_j^2 - E^2 - iE\gamma_j}. \quad (1)$$

Here ϵ_∞ is the background $MoSe_2$ dielectric constant and f_j, E_j, and γ_j are the oscillator strength, resonant energy, and linewidth of the j^{th} oscillator, respectively. In our analysis, each oscillator represents an individual excitonic or trionic feature. The complex refractive index is then calculated from the fitted dielectric function as follows: $\tilde{n} = n + ik = \sqrt{\tilde{\epsilon}}$. We note that this method of obtaining the refractive index has been previously demonstrated to give accurate results for TMDC monolayers from reflectance measurements at room temperature[43]. In Figure 2.2a, we see three prominent asymmetric features in the reflectance that exhibit a local minimum and maximum near the A exciton, trion, and B exciton resonances. At 4 K, the linewidths of these three oscillators are much narrower than their linewidths at room temperature[9,43]. Thus, their oscillator contribution dominates and we can approximate the dielectric function as a sum of these three oscillators since the resonance features from the other oscillators associated with the A2s and A3s states are not observed in our measurements. To account for oscillators outside of our measurement window, we add a background dielectric constant, $\epsilon_\infty = 20$, which is an intrinsic property that depends on all the higher energy optical resonances of the material[43].

The gate-dependent real and imaginary part of the refractive index are shown in Figure 2.2b. By comparing the experimental results with the corresponding fitted gate-dependent reflectance, we see that modeling the $MoSe_2$ dielectric function with 3 oscillators yields an excellent fit to the data (Figure 2.2a). The refractive index near both the A exciton and B exciton energy show extremely large gate tunability. At 748 and 754 nm, both the real and imaginary part can be tuned by over 200% compared to their values at the charge neutral point where the gate voltage V = -2.5V maximizes the exciton signal (Figure 2.2c). We note that this refractive index modulation is over 5 times larger than previously reported for both the real and imaginary part in TMDCs[11].

To better understand the mechanisms for the large refractive index modulation, we study the effects of carrier density on the oscillator strength, linewidth, and peak energy of the three oscillators. The resulting fitting parameters for each oscillator as a function of carrier density are shown in Figure 2.3a. For negative voltages, the change in the oscillator strength, linewidth, and peak energy are negligible since the hole doping is less efficient and presumably the semiconductor resides in a more "intrinsic" regime. However, for electron doping, we see an exchange of oscillator strengths between the A exciton and trion and a reduction in the oscillator strengths for both the A and B excitonic features. For the linewidth and peak energy behaviors, the A exciton and trion features are noticeably different from the B exciton feature. Figure 2.3a shows that the while linewidths of the A exciton and trion both broaden monotonically with carrier density, the B exciton initially broadens up to a certain doping density and then narrows. Moreover, the peak energies for both the A exciton and trion blueshift while the B exciton redshifts.

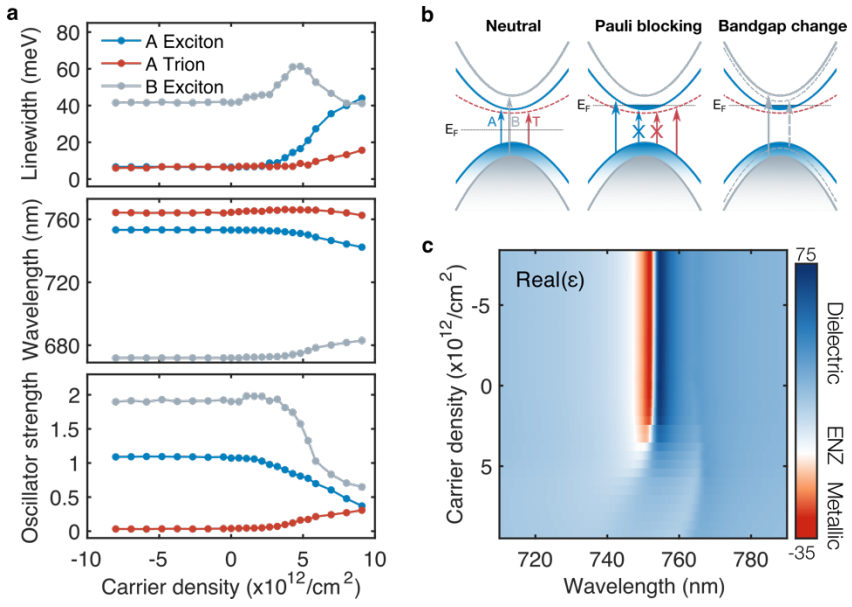

Figure 2.3. Gate-tunability of exciton parameters and ENZ response at T = 4 K. (a) Change in oscillator strength, resonance wavelength, and oscillator linewidth for the A exciton, B exciton, and trion as a function of electron carrier density. (b) Schematic of electronic band structure, allowed transitions and competing electronic effects for different Fermi levels. (c) Real part of the dielectric permittivity as a function of wavelength and carrier concentration. Near the A exciton resonance (754 nm), the $MoSe_2$ undergoes a transition from optically metallic to optically dielectric.

The striking differences in linewidth variation and energy shifts can be explained by considering the electronic band structure of $MoSe_2$ along with the effects of Coulomb scattering, screening, and Pauli blocking (Figure 2.3b). First, the screening of the electric field due to increased free carriers reduces the strength of the Coulomb interaction for the exciton. This leads to an overall decrease in the oscillator strength for both the A exciton and B exciton, attributable to a reduction in the binding energy. We note that while the trion oscillator strength increases due to a higher probability of formation in the presence of excess charges, the overall sum of A exciton and trion oscillator strength decreases, which is consistent with the effects of screening and reduced Coulomb interactions. Second, for the A exciton and trion, the Coulomb scattering leads to a decrease in the coherence lifetime, resulting in spectral broadening of both transitions. The behavior at the B exciton energy is likely due to an emergence of charged B excitons at low electron densities, where the total linewidth initially broadens due to contributions from both the neutral and charged B excitons. At higher electron densities, the neutral exciton vanishes, leading to a decrease in the total linewidth. However, the energies of the neutral and charged B excitons are close and are not spectrally resolved in the measurements, so only the combined contribution is considered in Figure 2.3a[36]. Finally, Pauli blocking typically leads to a decrease in the binding energy due to the occupation of electronic states and fermionic nature of electrons. Therefore, when the Fermi level is between the conduction bands, the A exciton and trion features will blueshift. However, the B excitons are only influenced by screening effects, which lead to redshifts from the renormalization of the bandgap to lower energies.

Tunable Epsilon-Near-Zero

Next, we explore the tunability of the ENZ and negative ϵ_1 behavior of $MoSe_2$ at low temperatures. We note that in previous reports of gate-dependent index modulation in TMDCs, the real part of the dielectric functions have been strictly positive[11,44] and the negative permittivity and ENZ properties in $MoSe_2$ have not been examined or observed in both monolayer or multilayer $MoSe_2$[43,45]. In Figure 2.3c, we observe that near the A exciton resonance, the real part of the dielectric function becomes negative when the

sample is hole doped or near intrinsic. As the electron density increases, the dielectric function approaches the ENZ regime and becomes positive over the entire spectral range. Moreover, we observe a spectral shift of the ENZ regime that results from the blueshift of the A exciton resonance.

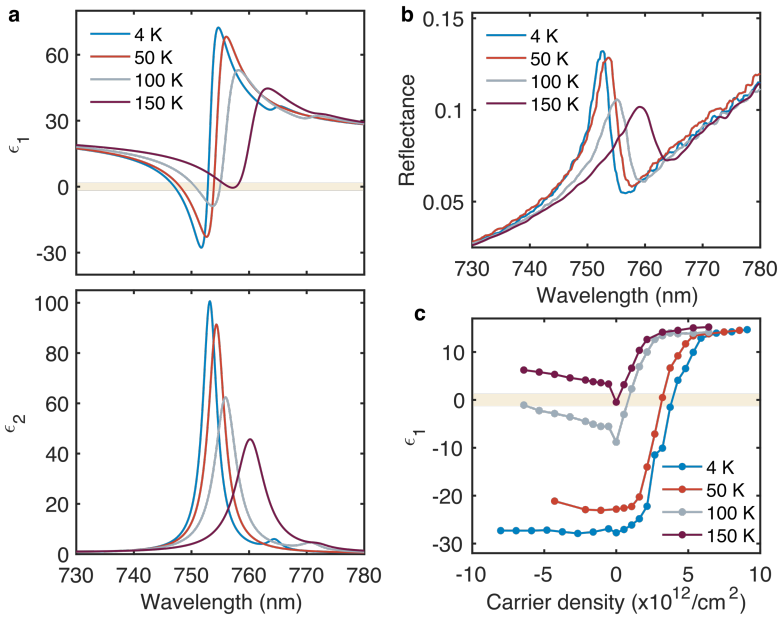

Figure 2.4. Gate dependence of dielectric function at different temperatures. (a) Temperature-dependent real and imaginary part of the dielectric function near the A exciton at charge neutrality for each temperature. (b) Measured temperature-dependent reflectance spectra at charge neutrality. (c) Minimum value of the real part of the dielectric permittivity near the A exciton resonance for different carrier densities and temperatures. The shaded region shows the ENZ regime.

Whether ϵ_1 takes positive or negative values can be attributed to three main factors. As mentioned previously, the first attribute is the background dielectric constant (ϵ_∞) that shifts ϵ_1 to a higher positive value. This is primarily dependent on the bulk properties of $MoSe_2$ and does not depend on the A exciton properties. The second and third factors are the oscillator strength and the linewidth of the exciton resonance where larger oscillator strengths and narrower linewidths result in a significant increase in ϵ_2 and allow ϵ_1 to become negative. This can be shown through comparing the carrier-density dependent exciton properties in Figure 2.3a with the corresponding ϵ_1 in Figure 2.3c. When the electron density reaches around 4x10^{12}/cm^2, the A exciton oscillator strength noticeably

decreases and the linewidth broadens, which also corresponds to the doping density where ϵ_1 becomes positive.

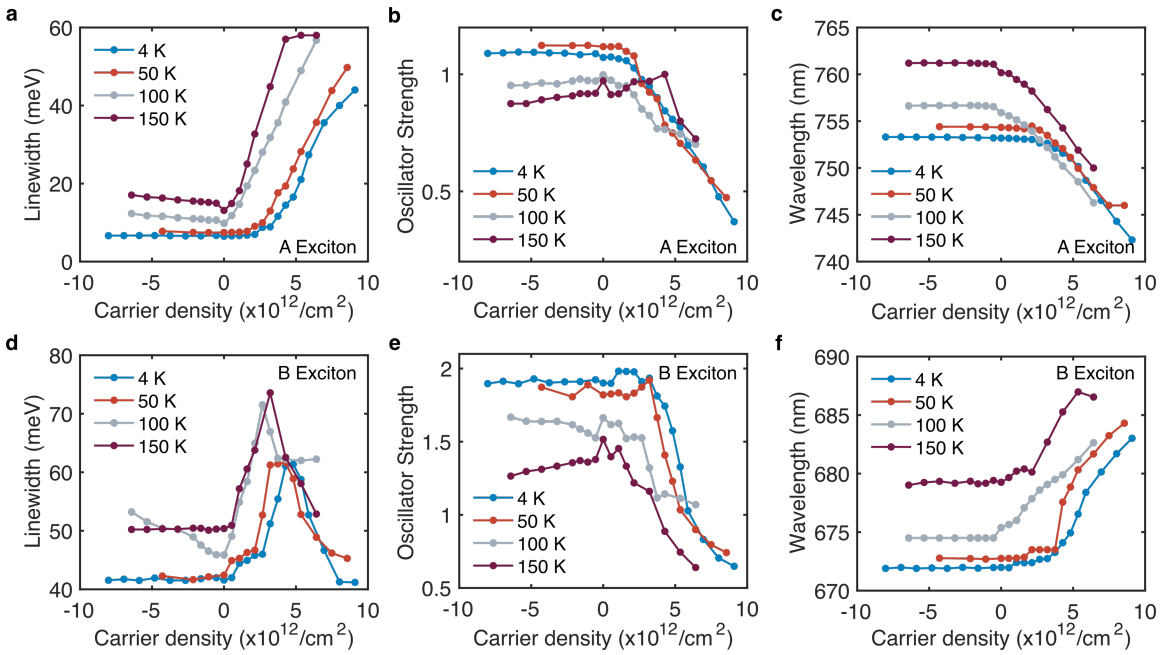

Figure 2.5. Carrier density and temperature dependence of A exciton (a,b,c) linewidth, oscillator strength, and resonance wavelength, and B exciton (d,e,f) linewidth, oscillator strength, and resonance wavelength

Temperature Dependence on Refractive Index Modulation

We perform the same gate dependent measurement and analysis at higher temperatures of 50 K, 100 K, and 150 K (Figure S1.1-S1.5). The temperature dependent real and imaginary part of the dielectric function and the corresponding reflectance spectra at the charge neutral point is shown in Figure 2.4a and 2.4b, respectively. While the increase in temperature allows for an additional linewidth broadening mechanism, even at these higher temperatures, ϵ_1 can attain negative values if the A exciton linewidth is around 13.2 meV or lower (Figure 2.4c and 2.5a). At 150 K, the linewidth is around 13.1 meV at charge neutrality, corresponding to a small negative value of $\epsilon_1 = -0.4$. Furthermore, by comparing Figure 2.4c and Figure 2.5a, we see that at each temperature, the carrier density

that gives rise to linewidths broader than 13.2 meV also corresponds the carrier density where ϵ_1 crosses the ENZ regime and switches from negative to positive.

Phase Modulation Calculations for Freestanding Monolayer

From the gate-dependent change in the complex refractive index, we can calculate the corresponding change in the phase of the reflected light off an isolated monolayer $MoSe_2$. For normally incident light, the complex reflection coefficient r of a thin layer with thickness d placed upon a semi-infinite substrate can be written as[46]:

$$r = \frac{(1-n_s)cos\phi - i(n_s-(n+ik)^2)\phi_0\left(\frac{\sin((n+ik)\phi_0)}{(n+ik)\phi_0}\right)}{(1+n_s)cos\phi - i(n_s+(n+ik)^2)\phi_0\left(\frac{\sin((n+ik)\phi_0)}{(n+ik)\phi_0}\right)} e^{-2i\phi_0} = |r|e^{i\Phi} \quad (2)$$

where n_s and $n+ik$ are the refractive index of the substrate and $MoSe_2$, respectively and ϕ_0 is the vacuum phase shift $\phi_0 = \frac{2\pi d_{MoSe_2}}{\lambda}$. Note that the phase Φ describes the optical field reflected off the sample while ϕ_0 is the phase evolution in vacuum. For a freestanding monolayer of $MoSe_2$, we set $n_s = 1$. For each temperature, a working wavelength that maximizes the phase difference is chosen and the calculated changes in phase from the charge neutral point $\Delta\Phi = \Phi(\mathrm{n_e}) - \Phi(\mathrm{n_e} = 0)$ are shown in Figure 2.6a. The resulting phase modulation as a function of wavelength, carrier density, and temperature are shown in Figure 2.6. We observe the largest overall change in the phase at 4 K, where $\Delta\Phi = 115°$. We attribute this large tunability as a result of the narrower linewidths at lower temperatures, which gives rise to a larger refractive index change around the resonance energies.

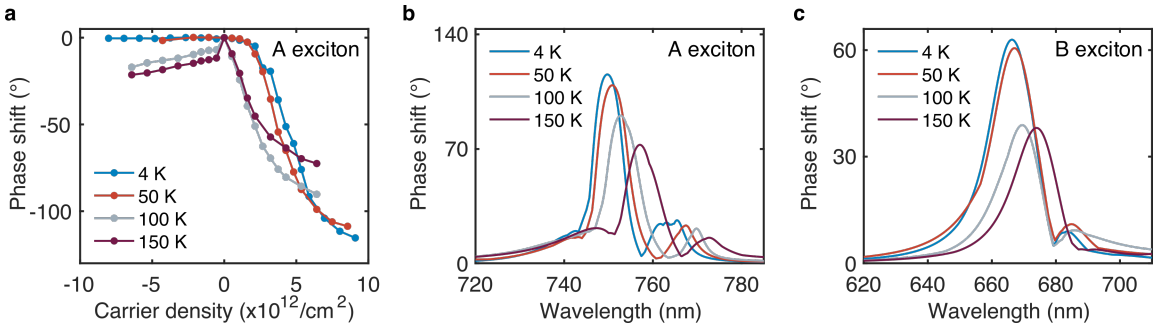

Figure 2.6. **Phase modulation of a freestanding $MoSe_2$.** Change in phase as a function of (a) carrier density and (b,c) wavelength around the A exciton and B exciton energy, respectively, for 4 K, 50 K, 100 K, and 150 K.

Experimental Measurements on Phase Modulation with Voltage

As a proof-of-concept demonstration of phase modulation, we directly measure the phase shift of the reflected light under applied bias by using an interferometer measurement where the laser light illuminates the edge of our monolayer flake. Therefore, a portion of the incident beam is reflected from the monolayer flake, while another portion is reflected from the substrate, which acts as a built-in phase reference. We then analyze interference fringes recorded by a CCD camera on and off the monolayer flake (Figure 2.7a). To analyze the phase shift of the light reflected from our flake, we process the images captured by the camera under different applied biases. In these images, we select one spatial cross-section from the flake interference fringes and another one from the substrate reference fringes area. The intensity values at the cross sections are then interpreted as the curves which are then smoothened by a moving average filter (Figure 2.7b). Figure 2.7c shows the sinusoidal functions fitted to the two mentioned fringe regions. Considering the offset between these two sinusoidal functions, one can calculate the phase shift for each applied bias via $\frac{\Delta p}{p_0}$ where Δp is the distance between the two peaks of sinusoidal functions that correspond to the flake fringes and reference fringes, and p_0 is the period of the sinusoidal wave. Accordingly, the measured interference fringe displacements are converted into a relative phase shift.

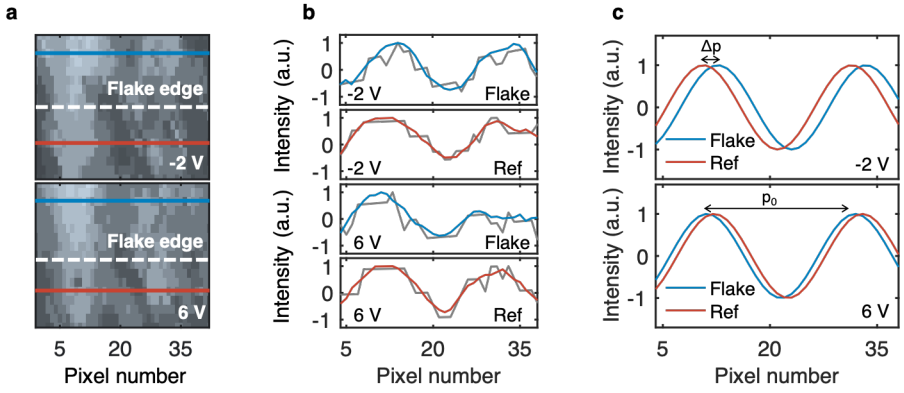

Figure 2.7. **The interferometer measurements for phase shift under applied bias.** (a) The interference fringe patterns captured by the camera. The white dashed lines shows the flake edge, and the blue and red line is the line cut of the interference fringe on the flake and on the reference, respectively. (b) Extracted intensity data (gray) from the flake and reference fringe and their smoothened curves (blue for flake, red for reference). (c) Fitted sinusoidal waves for flake and reference fringe cross-sections. Here, Δp is the distance between the two fixed peaks of the sinusoidal functions fitted from flake and reference fringe cross-sections, and p_0 is the period of the sinusoidal wave.

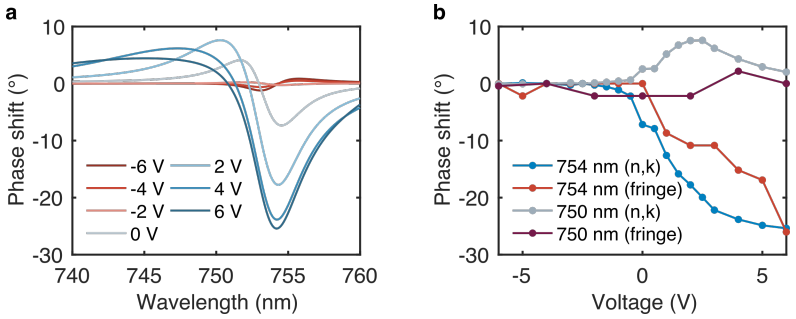

Figure 2.8. **Change in phase as a function of wavelength and voltage for 4 K.** (a) Calculated phase shift spectra from V = -2.5V using extracted n,k values around the A exciton energy. (b) Comparison between calculated phase shift from n,k and measured phase shift from fringe shift measurements for 754 nm and 750 nm.

Our measured phase shifts obtained directly from fringe shift measurements are in good agreement with the phase shift extracted from the refractive index values both at wavelengths corresponding to the excitonic resonance and off resonance (Figure 2.8a and b). At 754 nm, where the change in refractive index is maximal, we observe over a 25° phase shift. We note this phase shift is observed in the absence of coupling to antennas or

cavities, which is an important quantity for applications such as active metasurfaces[29,30,47]. By integration of gated monolayer $MoSe_2$ with a cavity or metasurface, we find that the phase shift can be increased to over >270° as illustrated in Figure 2.9.

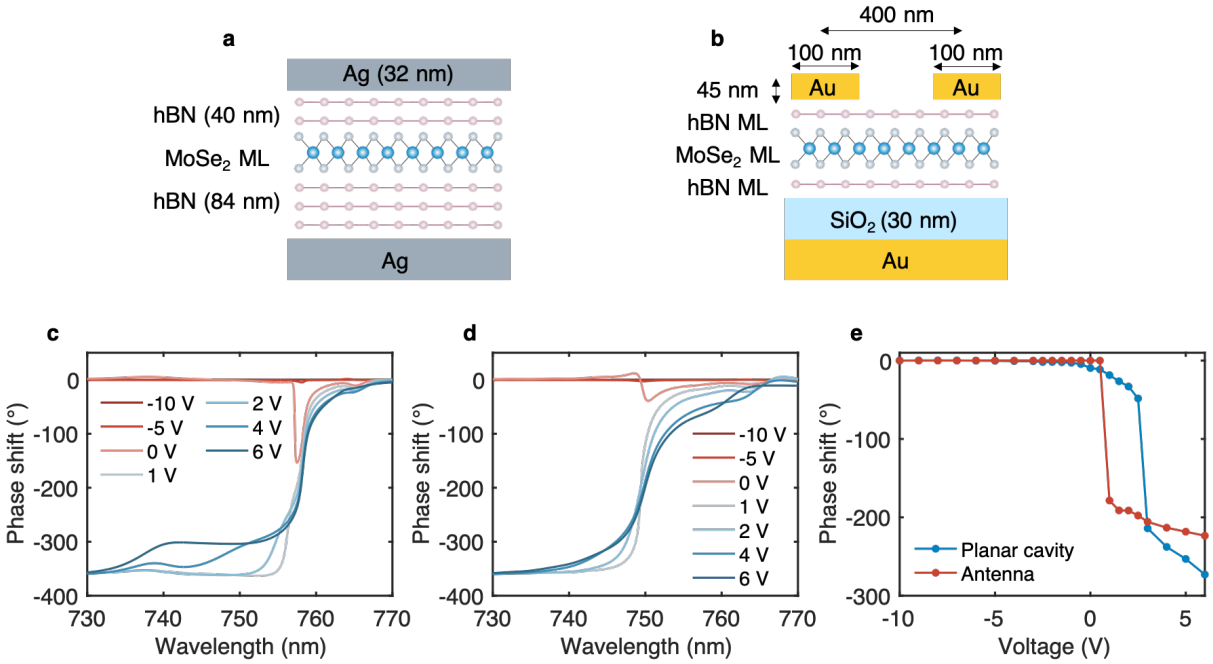

Figure 2.9. Phase shift for monolayer $MoSe_2$ coupled to cavity and metasurface antennas under applied bias. (a) Schematic of cavity structure with planar silver reflectors. (b) Schematic of metasurface used in FDTD Lumerical simulations with gold back reflector and antennas. (c) Phase shift spectra for reflected light off of the silver cavity. The phase modulation is maximized at around 760 nm. (d) Phase shift spectra for reflected light off of the gold metasurface antennas. The phase modulation is maximized at around 750 nm. (e) Voltage dependent phase modulation for both the cavity and metasurface for a fixed wavelength (λ = 760 nm for cavity, λ = 750 nm for metasurface).

Enhancing Phase Modulation in $MoSe_2$ Through Photonic Engineering

To demonstrate the potential of using $MoSe_2$ as an active material for tunable device applications, we propose two structures that would both give a gate-tunable phase shift of over 220° of the reflected light. We first design a planar cavity structure where we place a monolayer $MoSe_2$ encapsulated between 40 nm top hBN and 84 nm bottom hBN in a silver cavity (Figure 2.9a). The thickness of the top silver layer is 32 nm. To calculate the gate-dependent phase shift of the planar structure, we use the transfer matrix method and model

the $MoSe_2$ with the refractive index at 4 K. As shown in Figure 2.9c and 2.9e, the phase shift can be tuned above 270°.

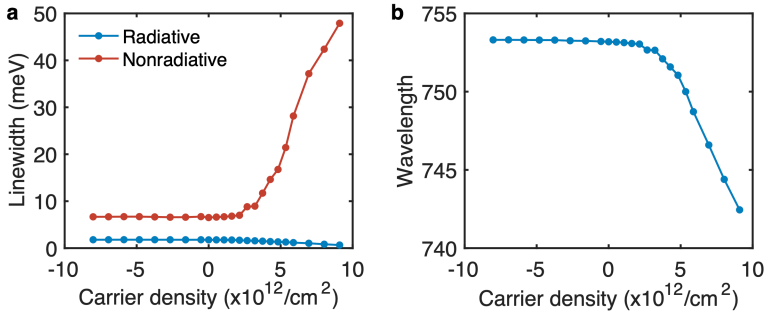

Figure 2.10. **Gate-dependent A exciton fitting parameters at T = 4 K.** (a) Fitted radiative and nonradiative linewidths and (b) A exciton resonance wavelength.

In order to calculate the gate dependent optical response of the $MoSe_2$ coupled to metasurface antennas (Figure 2.9b), we use full-wave electromagnetic calculations using finite difference time domain (FDTD) in Lumerical. In our simulation, the $MoSe_2$ monolayer is encapsulated between two hBN monolayers. The heterostructure is placed on top of a gold back reflector with a 30 nm thick SiO_2 spacer layer. Directly on top of the heterostructure is an array of gold antennas that are 45 nm thick and 100 nm wide placed 400 nm apart. The metasurface is illuminated by a normal-incidence plane-wave with an electric field along the direction of the antennas. When performing electromagnetic calculations, the mesh sizes are adjusted in different layers and the $MoSe_2$ is modelled using the refractive index data for 4 K. Figure 2.9d shows the phase shift spectra of the metasurface under different applied biases. Here, the phase shift is defined as a difference between the phases of the reflected and incident plane-waves calculated at the same spatial point. As seen in Figure 2.9d and e, we observe a phase modulation of over 220° near the A exciton resonance.

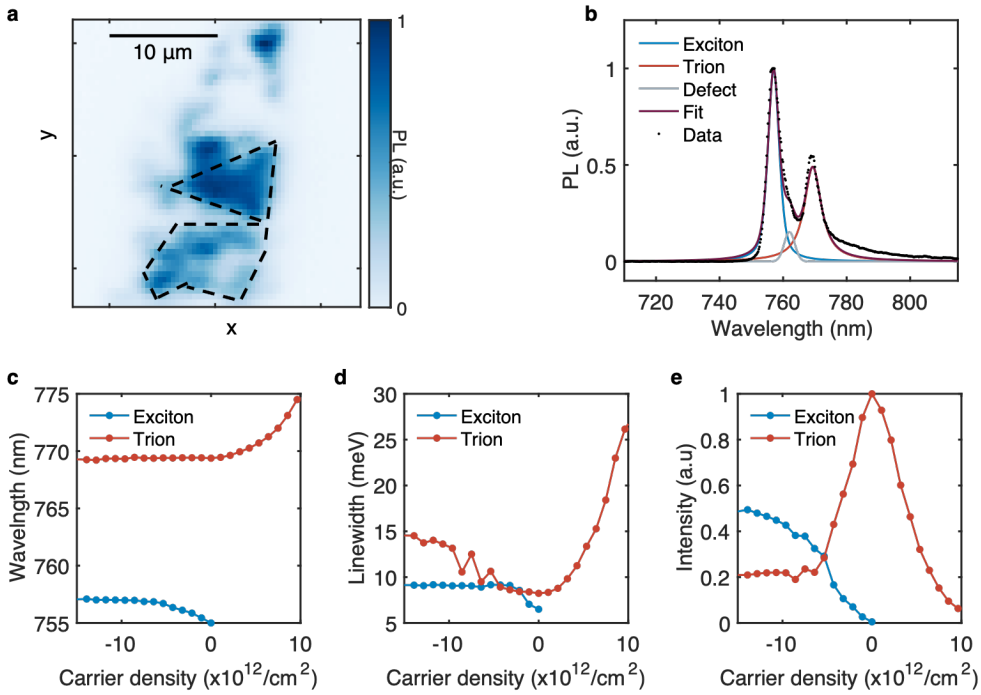

Figure 2.11. Photoluminescence of the monolayer $MoSe_2$ at T = 4 K. (a) Spatial PL map of graphene/hBN/$MoSe_2$/hBN heterostructure. Region of the monolayer device is enclosed in the dashed lines. (b) PL spectra and resulting double Voigt fit. (c,d,e) Gate-dependent double Voigt fit parameters for the A exciton and trion.

Effects of Radiative Efficiency and Quantum Yield on Index Modulation

So far, we have considered how the oscillator strength and linewidth change as a function of carrier density and temperature. However, these parameters can be directly related to the radiative γ_r and nonradiative decay rates γ_{nr} of the excitons by rewriting the dielectric function to take the form[9]:

$$\epsilon = \epsilon_1 + i\epsilon_2 = \epsilon_\infty - \frac{\hbar c}{d_{MoSe_2}} \sum_j \frac{\hbar \gamma_{r_j}}{E_j(E - E_j + i\hbar\gamma_{nr_j}/2)}. \quad (3)$$

In Figure 2.10, we plot the extracted radiative and nonradiative decay rates as a function of carrier density as well as temperature. At 4 K, the linewidth resulting from the radiative rate of the A exciton is extremely narrow, corresponding to a radiative linewidth of 1.8 meV. When the $MoSe_2$ is intrinsic, the total decay rate of the A exciton, $\gamma_T = \gamma_r + \gamma_{nr}$,

is around 6 meV, which is in good agreement with a Voigt-like line profile of the A exciton PL (Figure 2.11). As both the temperature and the carrier density increase, the nonradiative linewidth broadens while the radiative rate remains roughly constant. This implies that the gate tunability of the refractive index or dielectric function is primarily dictated by nonradiative decay mechanisms. On resonance, the dielectric function in Equation 3 diverges as $\gamma_{nr} \rightarrow 0$, suggesting that by suppressing the nonradiative pathways in the system, we can potentially achieve even larger refractive index modulation. While the index modulation has not been directly reported, previous studies have demonstrated narrow reflectance linewidths approaching the homogeneous linewidth limit where $\gamma_{nr} \ll \gamma_r$ [9,10,48]. We believe even larger tunability can be achieved using these near-homogeneous linewidth heterostructures that are optimized to observe the coherence properties of $MoSe_2$.

Conclusions

In summary, we show remarkable tunability in the complex refractive index of $MoSe_2$ at both the A and B exciton energy, highlighting its potential for use as a reconfigurable active element in optoelectronic systems, including modulators and active metasurfaces. We find that both temperature and Fermi level modulation leads to an ENZ behavior, resulting in a transition from dielectric to metallic, accompanied by large changes in reflectance amplitude and phase. The large permittivity and index modulation result from Pauli-blocking, Coulomb scattering, and screening, which directly influence the radiative and nonradiative channels, oscillator strengths, and resonance linewidths. Our findings of large electrical tunability provide a route for exploring novel phenomena and device applications based on monolayer TMDC excitons.

CHAPTER 3: DYNAMIC BEAM STEERING IN AN ATOMICALLY THIN EXCITONIC METASURFACE

In this chapter, we demonstrate dynamic beam steering by an active van der Waals metasurface that leverages large complex refractive index tunability near excitonic resonances in monolayer molybdenum diselenide ($MoSe_2$). Through varying the radiative and nonradiative rates of the excitons, we can dynamically control both the reflection amplitude and phase profiles, resulting in an excitonic phased array metasurface. Our experiments show reflected light steering to angles between -30° to 30° at different resonant wavelengths corresponding to the A exciton and B exciton. This active van der Waals metasurface relies solely on the excitonic resonances of the monolayer $MoSe_2$ material rather than geometric resonances of patterned nanostructures, suggesting the potential to harness the tunability of excitonic resonances for wavefront shaping in emerging photonic applications.

Introduction

Optical metasurfaces enable powerful light manipulation by controlling the amplitude, phase, polarization, and frequency of light at the subwavelength scale with an array of point-like scatterers at an interface[1]. This principle has been used to achieve versatile wavefront manipulation on platforms such as beam deflectors[49,50], ultra-high numerical aperture lenses[51,52], and on-chip holograms[53,54]. However, due to their static nature, the functions performed by these structures are fixed at the time of fabrication. Reconfigurable functions can be achieved by introducing a material with dynamically tunable optical properties[27]. This is done in active metasurfaces, where a reconfigurable material changes the scattering properties of an array of identical metasurface unit cells through applying an external stimulus, such as electrical gating or mechanical actuation[55,56]. Active metasurfaces based on co-integration of scatterers and active materials have been realized with transparent conducting oxides[28,29,57], liquid crystals[58], phase-change materials[59–61], thermo-optic materials[62], and graphene[63], which led to demonstrations of dynamic beam scanning[29,64,65], varifocal lenses[66], and polarization conversion[67]. However, these concepts

rely on critical coupling of tunable materials with resonant nanostructures, cavities, or antennas that are highly sensitive to geometric parameters and typically only operate over a single wavelength range. As structures for controlling the propagation of light become increasingly complex and compact, the need for new materials that can exhibit unique, strong light-matter interactions in the ultra-thin limit is growing rapidly.

Excitonic materials, such as two-dimensional (2D) van der Waals materials, are especially attractive as their resonant properties are intrinsic to the material and do not rely on coupling to cavities or antennas[13,15]. In the monolayer limit, the optical response of 2D transition metal dichalcogenides (TMDCs) is dominated by excitonic resonances[8,15,16,68], which are highly tunable with external electric field or doping[11,14], dielectric environment engineering[17,19], and strain[20,21]. The strong light-matter interactions from these excitonic resonances provide opportunities to design active optical devices where a single monolayer TMDC can act as both the resonant scatterer and the tunable material. Among different TMDCs, molybdenum diselenide ($MoSe_2$) exhibits especially large tunability of its optical properties at cryogenic temperatures. Without external enhancement or coupling to optical cavities, excitonic reflectivity of over 80%[9,10] and tunability of over 200% in the real and imaginary part of the refractive index[5] have been shown by modifying the radiative and nonradiative rates in $MoSe_2$. These rapid advances in understanding exciton resonances have stimulated thinking about active metasurfaces that exploit the excitonic modulation phenomena to enable van der Waals active metasurfaces[3,69]. For example, excitonic resonances have been used to demonstrate an intensity-tunable lens with a fixed focal length[4] or to steer a focused beam at an edge of three $MoSe_2$ flakes[12]. However, despite much progress, the dynamic control thus far has been limited to amplitude modulation or local point control of an edge, and versatile wavefront control of reflected light from a single atomic layer has remained an outstanding challenge.

Here, we show that tunable exciton resonances in $MoSe_2$ can be harnessed to design an excitonic phased array metasurface for dynamic beam steering. We can model the gate-tunable refractive index by modifying the radiative and nonradiative rates of the excitons with applied potential, which gives rise to large amplitude and phase modulation of the

scattered light. We also experimentally show how under varying voltage configurations, the reflected light can be steered to different angles at wavelengths corresponding to the A exciton and B exciton resonances. The observation of the beam steering at distinct excitonic wavelengths in the absence of coupling to antennas or gratings reveals the steering is independent of geometric resonances. Our results can be extended to other classes of ultra-thin materials that exhibit tunable excitonic resonances such as black phosphorus[3,70], semiconductor quantum dots[71,72], and layered perovskites[73,74], opening a new path for designing atomically-thin, reconfigurable metasurfaces.

Design of an Atomically Thin Metasurface

Figure 3.1 illustrates an atomically thin metasurface consisting of a monolayer of $MoSe_2$ encapsulated in hexagonal boron nitride (hBN) on subwavelength-spaced, lithographically patterned gold electrodes, supported on a thermally oxidized silicon substrate. Light impinges at normal incidence polarized along the y direction, and is reflected after passing through the heterostructure. The refractive index in the $MoSe_2$ layer is periodically modulated along the x direction at a subwavelength scale via a gate voltage V(x) applied to the periodically arranged gold electrodes. The application of gate voltage V(x), renders this structure an excitonic metasurface, where the material resonances in an atomic layer are modulated at a subwavelength scale to control the wavefront of the reflected light. This local modulation of the $MoSe_2$ imparts an electrically tunable phase shift $\varphi(x)$ to the reflected wavefront. Imposing a constant phase gradient on the reflected wavefront then deflects the reflected beam to an angle. Figure 3.1b illustrates this electrically controlled light deflection at the A exciton wavelength with the electric field intensity in a cross-section of the surface as calculated by full wave electromagnetic simulations.

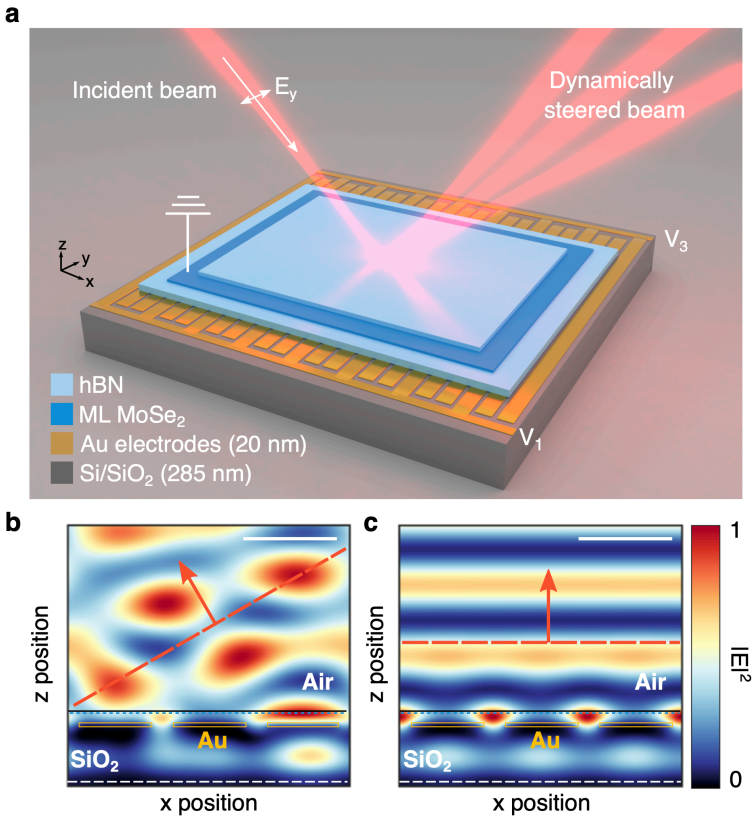

Figure 3.1. Dynamic beam deflection with a monolayer $MoSe_2$. (a) Schematic of the exciton based TMDC metasurface for dynamic beam steering. (b) Simulated electric field intensity cross section at the A exciton resonance of 757 nm under an applied voltage gradient. Top hBN and air interface shown in solid black line. $MoSe_2$ position shown in dotted blue line. Red arrow shows the reflected beam is steered. (c) Simulated electric field intensity cross section at 757 nm under a constant applied voltage. Red arrow shows the beam is specularly reflected. For (b) and (c) the voltage profile applied at the electrodes is [-5 V,0 V, 5 V] and [5 V, 5 V, 5 V], respectively. Scale bars: 500 nm.

In designing our metasurface, we first consider the voltage dependent optical response of monolayer $MoSe_2$ at 6 K. At cryogenic temperatures, the optical response of $MoSe_2$ is dominated by the A exciton, trion, and B exciton resonances where the linewidths of these three oscillators are much narrower than their linewidths at room temperature[9]. By exploiting the narrow excitonic linewidths at low temperatures, combined with Fermi level control via electrical gating of the carrier density, the refractive index of $MoSe_2$ can be modulated by over 200%[5]. The dielectric function of $MoSe_2$ takes the form of a sum of Lorentz oscillators[9,75]:

$$\epsilon = \epsilon_1 + i\epsilon_2 = \epsilon_\infty - \frac{\hbar c}{d_{MoSe_2}} \sum_j \frac{\hbar \gamma_{r\,j}}{E_j(E - E_j + i\hbar\gamma_{nr\,j}/2)}.$$

Here, ϵ_∞ is the background $MoSe_2$ dielectric constant, d_{MoSe_2} is the thickness of the monolayer, and E_j, γ_{r_j}, and γ_{nr_j} are the resonant energy, radiative, and nonradiative emission rates of the j^{th} oscillator, respectively. In our analysis, we model the dielectric function with two oscillators corresponding to the A exciton and trion and add a background dielectric constant, $\epsilon_\infty = 21$, to account for oscillators corresponding to higher energy optical resonances of the material outside of our measurement window[43]. The photoluminescence quantum yield is defined as $\eta = \gamma_r / (\gamma_r + \gamma_{nr})$, where the rates correspond to the intrinsic radiative and nonradiative emission rates of the A exciton at the charge neutral point. Since our $MoSe_2$ sample is n-doped, we set the charge neutral point to be -5 V, which is consistent with the voltage value that maximizes the neutral exciton resonance features in reflectance[5]. Electrical gating of the carrier density then modifies the radiative and non-radiative emission rates, yielding the gate tunable refractive index from the effects of Coulomb scattering, screening, and Pauli blocking from increased carrier density (see Figure S2.1, S2.2 and Supplementary Note S2.2). Depending on η, the $MoSe_2$ dielectric function takes a negative or positive value on resonance, yielding an epsilon-near-zero response and a tunable transition from metallic to dielectric near the exciton energy, resulting in large changes in reflectance amplitude and phase.

Effects of Radiative Efficiency and Quantum Yield on Beam Diffraction Efficiency

Figure 3.2a and 3.2b illustrate the simulated gate voltage dependent reflection amplitude and phase of our atomically thin metasurface. Here we choose a η = 0.5, and a top and bottom hBN thickness of 6 nm and 60 nm, respectively, with gold electrodes that are 20 nm thick, 380 nm wide and spaced at 120 nm apart (simulated reflectance and phase spectrum for η = 0.25 are shown in Figure S2.3). The reflection spectrum is dominated by the gate-tunable A exciton resonance and thin film interference from the substrate and heterostructure. With the incident light polarized along the gold contacts, tunable reflection originates only from the A exciton of $MoSe_2$, as the local surface plasmon mode of the

electrodes is not excited (the corresponding analysis and discussion for illumination with the perpendicular polarization are shown in Figure 3.3). The gate voltage induced reflected light phase shift is maximized near the A exciton resonance wavelength of 757 nm, and reaches up to a range of 240°. Figure 3.2c and d show the voltage dependent amplitude and phase of the reflected light at the A exciton resonance for $\eta = 0.25$, 0.5 and 0.75. Notably, the available gate voltage-induced phase modulation range strongly depends on the quantum yield of the $MoSe_2$, with a higher η resulting in an increased tuning range. While large values of η of up to 90% have been reported, it is important to note that there can be a significant variation between different monolayer flakes, and also variation within the same flake due to charge and strain inhomogeneities[10]. Hence, for larger area structures, such as the one proposed here, the effective averaged quantum yield is reduced compared to the reported peak values. However, even with moderate quantum yields ranging between 25-50% a significant phase modulation range is attained. Setting the gate voltage along the metasurface to produce a constant phase gradient (according to the look up table in Figure 3.2d), allows steering the reflected beam to arbitrary angles θ. Figure 3.2e and f show the far field intensity pattern of seven different periodic voltage configurations $V(x)$ that steer the reflected beam between –30° to 30° for $\eta = 0.25$ and $\eta = 0.5$. The seven different voltage configurations generate a phase gradient as required for deflecting the light to the specified angle. Even with the reduced quantum yield of 25%, light can be deflected to varying angles with 8% diffraction efficiency, although the specular reflection remains intense. With a quantum yield of 50%, most light is steered into the desired direction with up to 65% diffraction efficiency, and relatively little intensity is specularly reflected or coupled to the opposite direction. As the quantum yield approaches unity (Figure 3.4), diffraction efficiencies up to 84% could be achievable with a single $MoSe_2$ layer. However, the theoretical efficiency will be limited through the covariation in amplitude and phase modulation with voltage and can be further improved through introducing a second $MoSe_2$ layer for two independent control parameters[57].

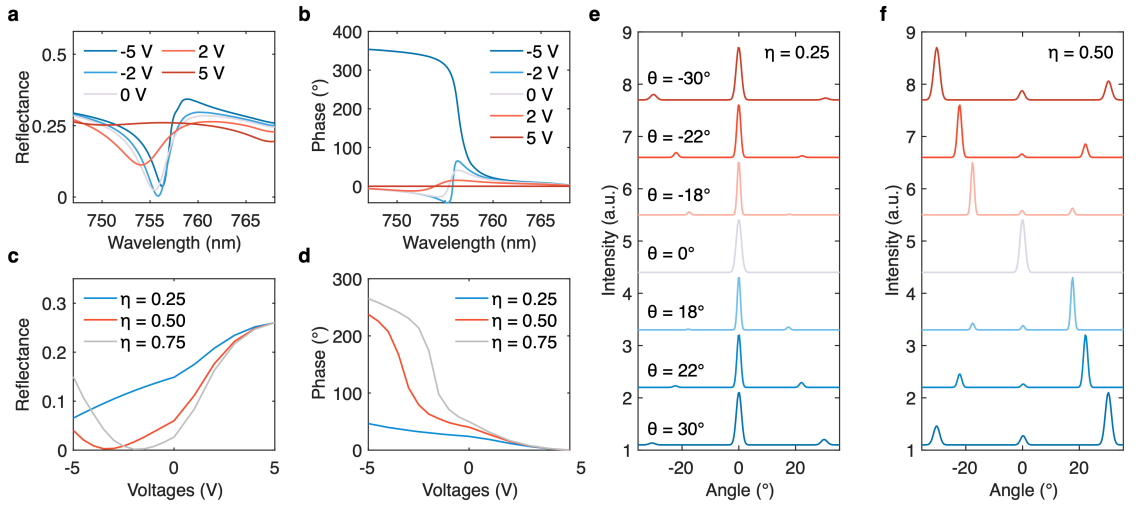

Figure 3.2. Simulated voltage-dependent reflectance amplitude, phase, and beam steering for y-polarization. (a) Reflectance spectra and (b) phase for different voltages for an $MoSe_2$ sample with photoluminescence quantum yield $\eta = 0.5$. (c) Voltage-dependent reflectance and (d) phase at the A exciton wavelength of 757 nm for different radiative efficiencies. (e,f) Simulated reflected angular far field intensity for $\eta = 0.25$ and $\eta = 0.5$, respectively, under different applied voltage gradient profiles and corresponding steered angle. The phase periodicities for the angles 30°, 22° and 18° are 1.5, 2 and 2.5 μm, respectively, where the periodicity was varied by changing the number of electrode elements in each period.

Polarization Dependence on Steering

In the previous section, we consider the incident light polarized along the gold contacts where the tunable reflection originates purely from the A exciton of $MoSe_2$, as the local surface plasmon mode of the electrodes is not excited. Here, we consider the corresponding analysis for illumination with the perpendicular polarization. Figure 3.3a and 3b shows the simulated gate voltage dependent amplitude and phase of the reflected light off the metasurface for $\eta = 0.5$. At a working wavelength of the A exciton resonance near 757 nm, the change in the reflectance amplitude and phase as a function of voltage is shown in Figure 3.3c and 3d, which shows the similar modulation range as the parallel polarization (Figure 3.2c and 2d). By applying a voltage gradient across the electrodes, we can also steer the reflected light to a desired angle (Figure 3.3e and 3f), with high directivity for $\eta = 0.5$ (Figure 3.3f).

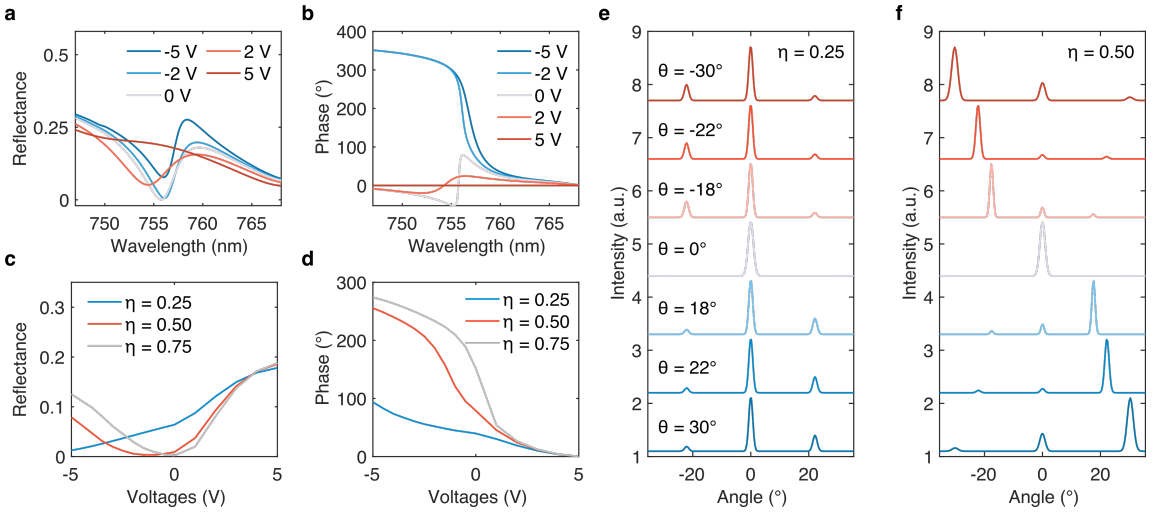

Figure 3.3. Simulated voltage-dependent reflectance amplitude, phase, and beam steering for x-polarization. (a) Reflectance spectra and (b) phase for different voltages for an $MoSe_2$ sample with $\eta = 0.5$ for x-polarized illumination. (c) Voltage-dependent reflectance and (d) phase at the A exciton wavelength of 757 nm for different radiative efficiencies. (e,f) Simulated reflected angular far field intensity for $\eta = 0.25$ and $\eta = 0.5$, respectively, under different applied voltage gradient profiles and corresponding steered angle. The gate dependent reflection, phase and beam deflection was simulated using periodic boundary conditions and a spatially coherent plane wave illumination.

Notably, there is a dynamic interplay between the $MoSe_2$ quantum yield, its refractive index modulation, and radiative decay rate enhancement dictated by its nanophotonic environment. This is expected to be more pronounced for the x-polarized illumination, due to the local surface plasmon resonance in the electrodes. The decay rate enhancement due to the Purcell effect, can increase the PLQY, and therefore enable larger phase modulation, as shown in Figure 3.3, compared to the same $MoSe_2$ metasurface structure operated under y-polarization (Figure 3.2). This also suggests that exploring resonant nanophotonic structures that offer large Purcell factors, in addition to the material resonances demonstrated here, is a viable path to realizing devices with improved efficiency.

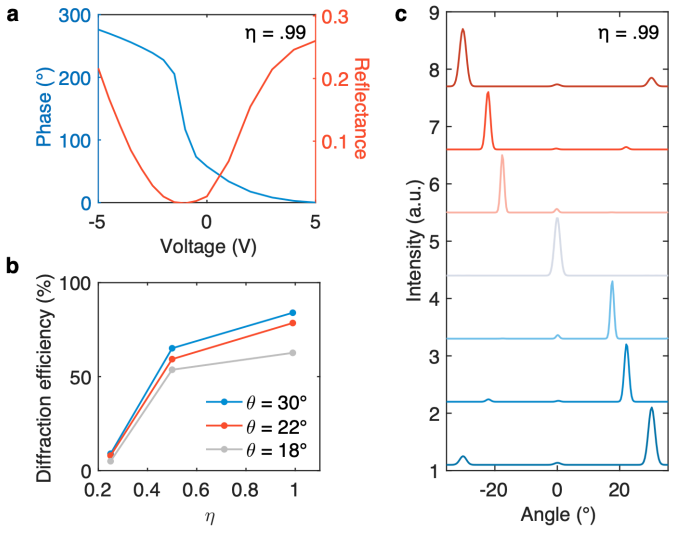

Figure 3.4. Simulated beam steering efficiency for near-unity quantum yield and y-polarization. (a) Voltage-dependent reflectance and phase at the A exciton wavelength of 757 nm for η = 0.99. (b) Simulated diffraction efficiency vs quantum yield for different steering angles corresponding to the first diffractive order. We note for smaller steering angles (e.g. 18° and 22°), the diffraction efficiency is lower due to the presence of higher diffraction order. (c) Simulated reflected angular far field intensity for η = 0.99 under different applied voltage gradient profiles.

Experimental Demonstration of Beam Steering with a Monolayer $MoSe_2$

To experimentally demonstrate beam steering with a monolayer $MoSe_2$ flake, we perform spectrally selective Fourier plane imaging using reflected light. For the measurement, we illuminate a large area of the surface (10 μm in diameter) with a near collimated beam. To avoid effects arising from surface nonuniformity, we limit light collection to an area of 4 μm in diameter, by means of spatial filtering with an aperture in the image plane (see Figure 3.5).

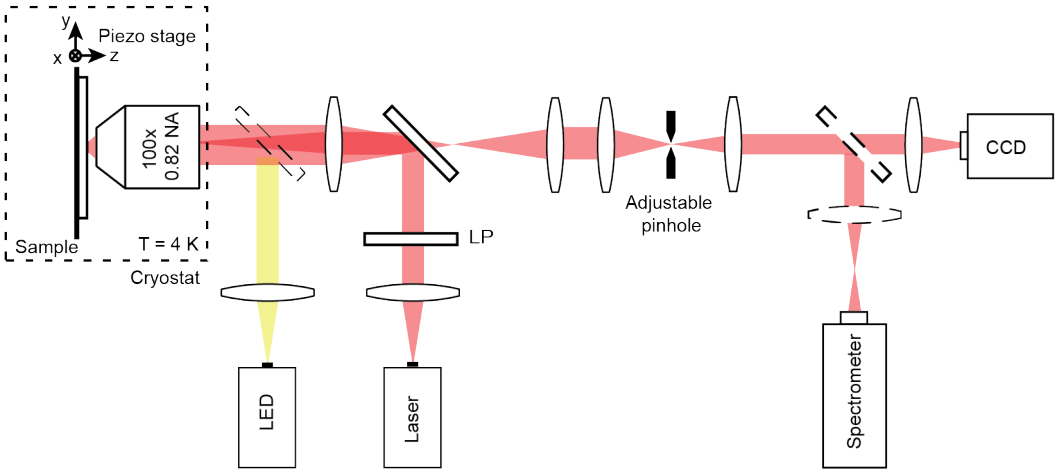

Figure 3.5. Experimental set-up. To characterize the fabricated samples, Köhler illumination in reflection was employed with light from a supercontinuum laser. The reflected light is collected by an imaging objective (100x, 0.82 NA) and projected onto a CCD camera through a set of lenses. With a flip mirror, the transmitted light can be sent either to the camera or to the spectrometer. In the detection path, an image plane is formed with an adjustable iris to limit the area that is projected on the camera or spectrometer. The lens in front of the spectrometer is switched to a different focal length to form a Fourier plane image on the spectrometer sensor.

Figure 3.6a shows a microscope image of the fabricated metasurface, which contains both a monolayer (blue) and bilayer (red) portion of a $MoSe_2$ flake encapsulated with hBN. We fabricate the metasurfaces by dry transfer of an hBN/$MoSe_2$/hBN heterostructure onto a lithographically patterned substrate with gold electrodes. The electrodes are patterned to allow setting a periodic three level voltage gradient, with the first set connected to an external voltage V_1 and the third set to V_3, and the second set of electrodes floating. The fabricated surfaces are characterized in a cryostat at a temperature of 6 K by performing widefield reflectance microscopy with a coherent broadband illumination. Figure 3.6b shows a spatial reflectance map of the ungated metasurface near the A exciton resonance at 757 nm. Figure 3.6c illustrates reflectance spectra measured on the monolayer and bilayer region at the positions marked in Figure 3.6b. In the monolayer region, a clear reflectance minimum is observed at 757 nm as expected due to the A exciton. We note the exciton in the bilayer is redshifted to 767 nm from interlayer hybridization effects and is broader than the exciton in the monolayers[76].

Figure 3.6d illustrates the measured spectral Fourier plane image on the monolayer portion of the sample for four different voltage configurations. For a constant voltage, $V_1 = V_3 = 0$ V, the incident beam is specularly reflected to $\theta = 0°$, with some light coupled to symmetric side lobes at $\theta = \pm 15°$ that arise from the finite imaging aperture. Imposing a symmetrically varying voltage profile, $V_1 = V_3 = -5$ V, on the surface couples light into the +1 and –1 diffraction order at $\theta = \pm 30°$ at the A exciton wavelength 757 nm. Notably, the two deflected beams are separate from the specular reflection and close to collimated, with an angular divergence of 16°. This is a stark contrast to previous demonstrations, where the deflected beam was highly divergent[12]. The asymmetry in the intensity of the +1 and –1 diffraction order likely is due to an asymmetric alignment of the finite size aperture used in the detection with the applied voltage profile. By applying a voltage gradient to impose a linear phase gradient along the interface, $V_1 = 5$ V and $V_3 = -5$ V, we show the asymmetric steering of light into the +1 diffraction order, and the suppression of the –1 order. Similarly, by applying an inverted voltage gradient, $V_1 = -5$ V and $V_3 = 5$ V, we steer light into the –1 diffraction order and suppress the +1 order. In all three cases, beam steering occurs selectively at the A exciton wavelength, which is further evidence of the exciton-induced tunability. The small asymmetry in steering light to the +1 and –1 is attributed to the finite sized aperture in the detection. Figure 3.6f shows a spatial map of the measured efficiency of coupling reflected light into the +1 diffraction order at various locations of the surface with $V_1 = 5$ V and $V_3 = -5$ V. On the monolayer flake, outlined in blue, there is strong spatial variation in the diffraction efficiency, which we attribute to the spatial inhomogeneity of the linewidth and quantum yield. The region with the highest diffraction efficiency is expected to concur with the region of highest quantum yield in the $MoSe_2$. In the bilayer region, the diffraction efficiency vanishes at 757 nm, but is observed at the redshifted bilayer exciton resonant wavelength of 767 nm (Figure S2.4).

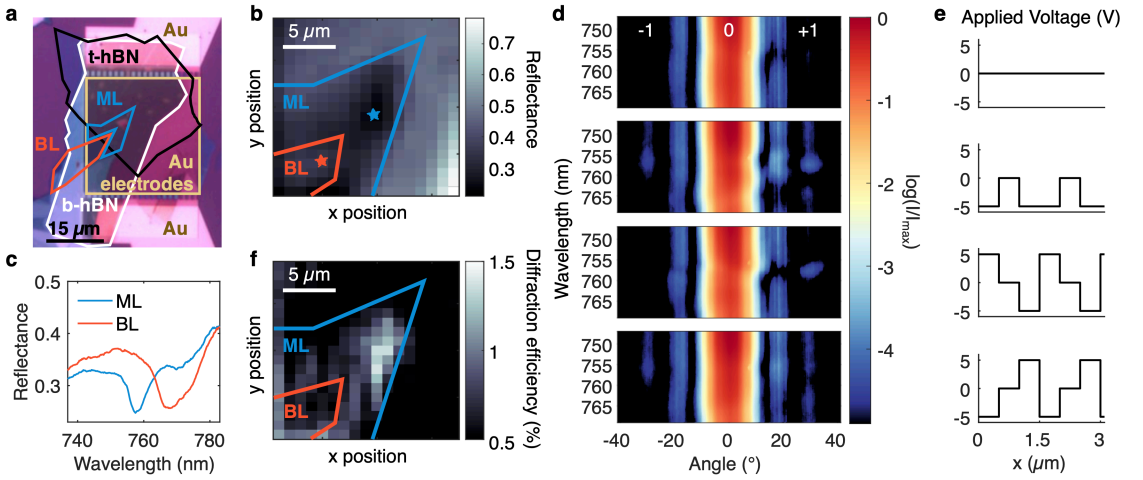

Figure 3.6. Fabrication and experimentally measured dynamic beam steering in monolayer $MoSe_2$. (a) Optical microscope image of the metasurface device. (b) Spatial reflectance map at 757 nm. (c) Reflectance spectra of the monolayer (blue) and bilayer (red) $MoSe_2$ region. (d,e) Measured spectral Fourier plane images of the monolayer $MoSe_2$ metasurface near the A exciton resonance under different applied voltage configurations to each electrode for dynamic beam deflection at ±30°. (f) Spatial map of the intensity of the steered light at the +1 diffraction order (+30°). In a, b, and f, the solid blue line outlines the monolayer region (ML) and the solid red line outlines the bilayer region (BL).

Voltage Dependence of the A Exciton Diffraction Efficiency

Next, we study the voltage dependence and spectral dependence for the different diffractive orders at the A exciton energy. In Figure 3.7a and 7b, we see the intensity at 30° is maximized near the charge neutral point of the $MoSe_2$ between -4 V to -5 V, where the A exciton linewidth is the narrowest. As the carrier density increases through either hole or electron doping, the intensity at 30° decreases due to lower oscillator strength and linewidth broadening from increase in nonradiative rates. We also observe the blueshift in A exciton resonance energy, which is consistent with previously observed blueshift by Pauli blocking upon doping. We note that the effects of exciton diffusion and drift do not play a significant role in the time scales of our metasurface operation, where at steady-state, the index contrast is given by the carrier concentration. The gate dependent diffraction efficiencies for the -1, 0, and +1 diffraction order with the corresponding simulation results are shown in Figure 3.4c, d, and e, respectively. Under the voltage gradient profile, we see an

exchange of the diffraction efficiency of the 0th order and +1 order, whereas the diffraction efficiency at the -1 order shows minimal dependence on the applied voltage. At -4 V, the diffraction efficiency is in good agreement with our simulated result of an averaged $\eta = 0.25$ (Figure 3.7c-e), which confirms the observed beam deflection arises from excitonic phase modulation in $MoSe_2$.

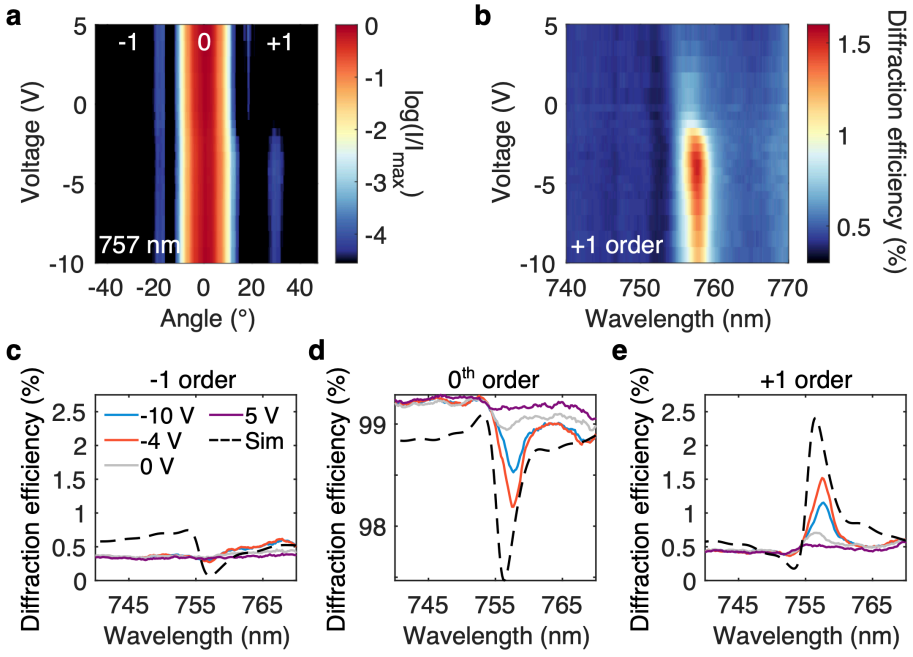

Figure 3.7. Voltage dependence of diffraction efficiency near the A exciton resonance. (a) Measured intensity in the Fourier plane for $V_1 = 5$ V and varying voltage V_3 at the resonant A exciton wavelength of 757 nm. Under the applied asymmetric voltage gradient, only the +1 diffractive order is observed. (b) Voltage and spectral dependence of the diffraction efficiency of the +1 order. The intensity is maximized near the charge neutral point of the $MoSe_2$ between -4 V to -5 V and blueshifts with increase in carrier density. (c-e) Measured (solid) and simulated (dashed) diffraction efficiency for the -1, 0, and +1 order, respectively. The $MoSe_2$ in the simulation is modeled with quantum yield $\eta = 0.25$. The intensity at the 0th order is primarily exchanged with the +1 order at the A exciton resonance.

Voltage Dependence of the B Exciton and Trion Diffraction Efficiencies

Aside from the A exciton resonance at 757 nm, we also observe resonances corresponding to the B exciton and trion in $MoSe_2$. The spectral Fourier plane images near the B exciton

wavelength are shown in Figure 3.8a. For $V_1 = V_3 = 5$ V, we see minimal beam deflection to the +1 order (26°) due to the suppression of the B exciton resonance. However, under an applied voltage gradient, with $V_1 = 5$ V and $V_3 = -5$ V, we observe an enhancement in the intensity at the +1 diffractive order. Figure 3.8b shows the voltage (V_3) dependent diffraction efficiency at the +1 order for wavelengths between 650 nm to 800 nm, where $V_1 = 5$ V and V_3 is varied. We observe three prominent features at 670 nm, 757 nm, and 770 nm that correspond to the resonances of the B exciton, A exciton, and trion, respectively, suggesting that the incident beam can be steered to a desired angle for different excitonic resonant wavelengths.

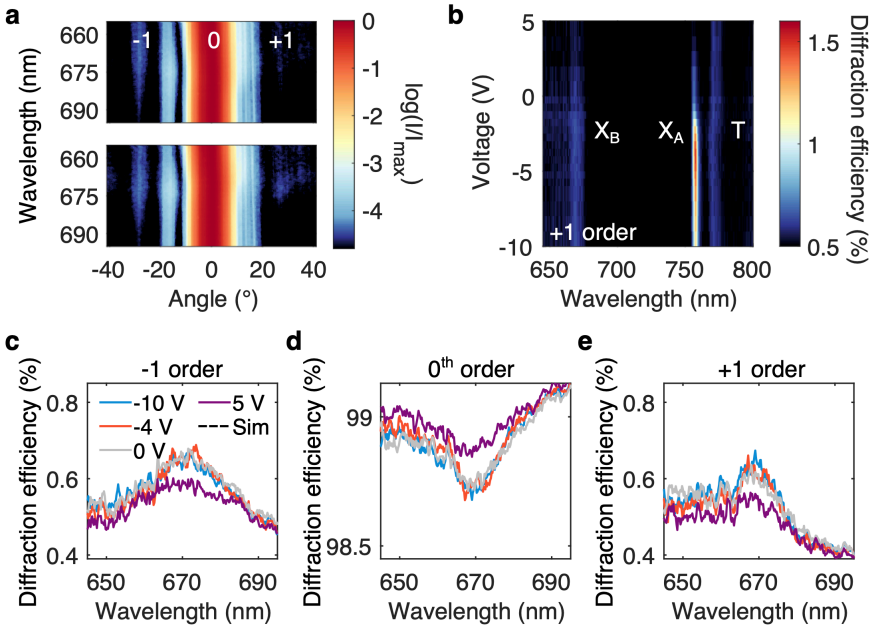

Figure 3.8. Voltage dependence of diffraction efficiency near the B exciton resonance. (a) Measured spectral Fourier plane images of the monolayer $MoSe_2$ metasurface near the B exciton resonance for $V_1 = V_3 = 5$ V (top) and $V_1 = 5$ V , $V_3 = -5$ V (bottom). (b) Voltage and spectral dependence of the diffraction efficiency of the +1 order between 650 nm and 800 nm. Three distinct peaks corresponding to the B exciton (X_B), A exciton (X_A), and trion (T) are observed. (c-e) Measured diffraction efficiency for the -1, 0, and +1 order, respectively. The intensity at the 0^{th} order is exchanged with both the -1 order and +1 order at the B exciton resonance.

Similar to the A exciton, the B exciton diffraction efficiency is also maximized near the charge neutral point. However, the deflection efficiency is lower for the B exciton since the linewidth is broader than the A exciton, resulting in lower refractive index modulation and phase shift. Moreover, the lower phase shift also results in less suppression of the -1 order, so the beam is deflected to both the -1 and +1 order even under an asymmetric voltage gradient (Figure 3.8c-e). The effect of lower phase modulation is also observed at the trion energy, where we see minimal variation in diffraction efficiency with gate voltage due to the low oscillator strength of trions. Nevertheless, the observation of steering at different wavelengths that correspond to excitonic resonances shows our design solely relies on tunable excitonic resonances in $MoSe_2$ -a material property- and not geometric antenna or grating resonances.

Modelling and Effect of the Finite Image Aperture

In the experiment, we reduce effects of surface nonuniformity, by spatial filtering in the image plane and limit the signal collection to an area of 4 μm in diameter, as shown in a sketch of the experimental set up in Figure 3.5. In our numerical model, we account for this finite imaging area and the finite numerical aperture of the imaging objective (NA=0.82) in the following manner. The reflected electric and magnetic field are recorded at a distance of 1 μm from the surface. By applying a far field projection, these near field components are decomposed into plane waves propagating to an azimuthal angle ϕ and a polar angle θ. To account for the finite numerical aperture of the imaging objective, all plane wave components at $\theta > \sin^{-1}\mathrm{NA}$ are set to zero. A chirped z-transform is applied to calculate an image with $\boldsymbol{E}(x, y)$, similar to the image plane in the detection path of the experimental set-up. The magnetic field $\boldsymbol{H}(x, y)$ is calculated by numerically approximating Maxwells equations in free space. To account for the finite imaging area, all electric and magnetic field components at > 2 μm are set to zero. Finally, to obtain a Fourier plane image, $\boldsymbol{E}(x, y)$, and $\boldsymbol{H}(x, y)$ are again decomposed to plane waves using a far field projection.

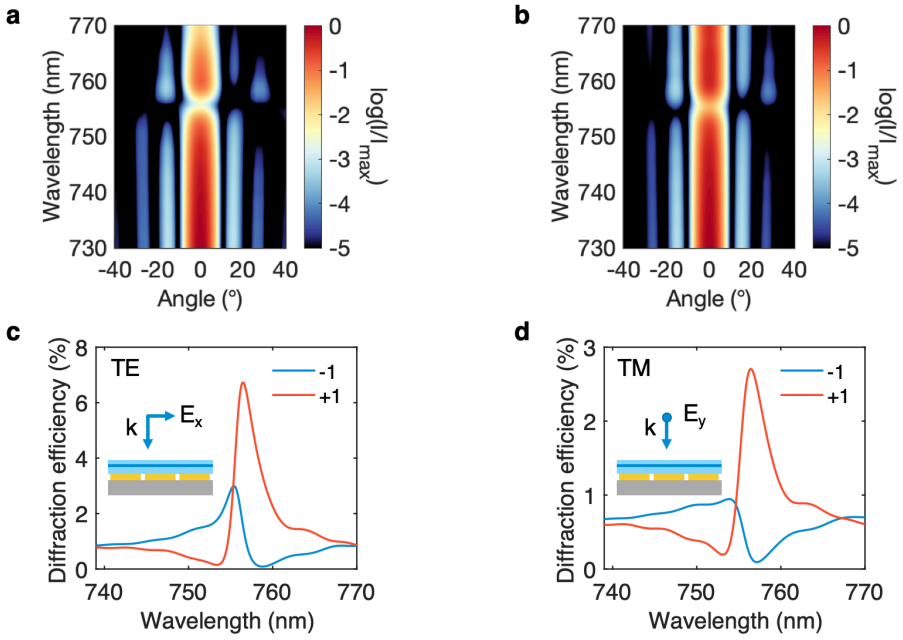

Figure 3.9. Simulated beam steering efficiency in monolayer $MoSe_2$ for x- and y-polarized illumination with finite aperture size. Simulated spectral Fourier plane images of the $MoSe_2$ metasurface with an applied voltage gradient V_1 = 5 V and V_3 = -5 V for (a) x-polarized illumination and (b) y-polarized illumination. Simulated diffraction efficiency for the -1 and +1 order of the $MoSe_2$ metasurface with (c) x-polarized illumination and (d) y-polarized illumination. To account for the finite aperture size in the comparison between simulations and experiments, a gaussian illumination with a 24 μm beam diameter and perfectly matched layer boundary conditions were used. The effect of the numerical aperture of the imaging objective lens and the finite imaging aperture was accounted for through a set of Fourier transforms and spatial filtering in the Fourier and image plane.

Figure 3.9 shows the diffraction efficiency for lower PLQY of $\eta = 0.25$ and taking into account the finite imaging aperture for both perpendicular and parallel polarization illumination. We see with the same voltage configuration, both polarizations show similar intensity at the +1 diffractive order (at 30°). However, the diffraction efficiency for the perpendicular direction is slightly higher due to the stronger absorption from exciting the plasmon mode of the gold electrodes that results in a lower 0^{th} order intensity that is specularly reflected.

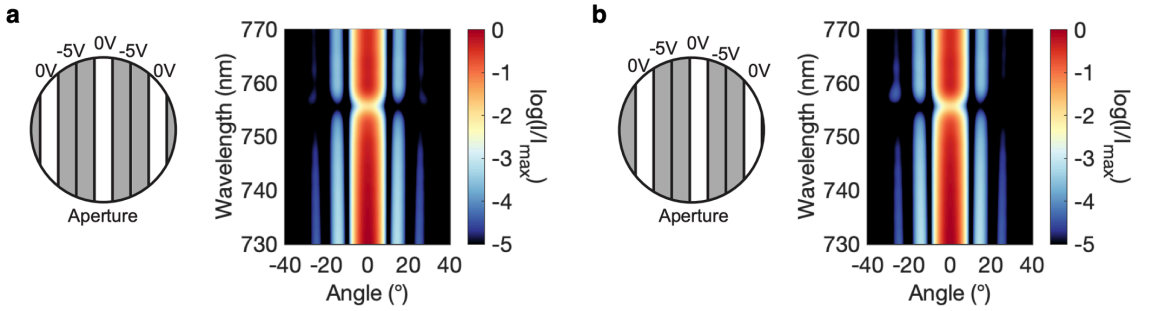

Figure 3.10. Simulated effect of imaging aperture on beam steering on a symmetric voltage-imposed grating. (a) Simulated spectral Fourier plane images of the $MoSe_2$ metasurface with an applied voltage gradient V_1 = -5 V and V_3 = -5 V for y-polarized illumination and a symmetric alignment of the metasurface with the imaging aperture as indicated in the schematic. Symmetric alignment leads to a symmetric beam deflection in the Fourier plane. (b) Simulated spectral Fourier plane images of the $MoSe_2$ metasurface with the same applied voltage gradient and illumination but with an asymmetric alignment of the metasurface with the imaging aperture. Asymmetric alignment leads to an asymmetric beam deflection in the Fourier plane especially around the exciton wavelength.

The finite imaging area and its alignment with sample electrodes and imposed voltage gradient, can result in an asymmetric distribution of light in the Fourier plane. This is observed in Figure 3.6d in experiment, where a symmetric grating shows a small asymmetry in the Fourier plane. To provide further understanding of this observation, we performed numerical simulations of the corresponding grating structure with two different alignment positions of the grating with respect to the image aperture, as shown in Figure 3.10. A symmetric alignment of the imaging aperture with the grating (Figure 3.10a) leads to a symmetric beam deflection in the Fourier plane. An asymmetric alignment of the imaging aperture with the grating (Figure 3.10b) leads to an asymmetric beam deflection in the Fourier plane, especially around the exciton wavelength. This effect is likely contributing to the asymmetry observed in the experiment, as reported in Figure 3.6d.

Conclusions

We employ tunability in the complex refractive index of monolayer $MoSe_2$ near excitonic resonances to enable multi-wavelength excitonic beam steering at the nanoscale. We find the steering efficiency and directivity are limited by the homogeneity in the radiative

efficiency over the metasurface aperture, here comprising a few microns across the flake. While our demonstration of excitonic beam steering was performed on a 15 μm flake at 6 K, large aperture area room temperature metasurface operation could potentially be achieved through methods of gold assisted exfoliation[77,78] and through suppression of nonradiative decay mechanisms at higher temperatures, such as superacid treatments[79] or strain[80]. Advances in large area fabrication of 2D materials would enable more complex device operations, such as multifunctional excitonic metasurface that demonstrate both tunable focal length and beam steering, or space-time modulated metasurface based on the nanosecond response time of excitons. Our findings provide a route for exploring arbitrary wavefront shaping based on the tunability of excitons.

CHAPTER 4: ELECTRICALLY TUNABLE TOPOLOGICAL SINGULARITIES IN EXCITONIC HETEROSTRUCTURES FOR WAVEFRONT MANIPULATION

Analysis of non-Hermitian photonic systems by the spectral positions of their topological singularities plays a central role in their design. Recently, the link between topological phase singularities and existing schemes for wavefront manipulation revealed that the full-2π phase control of light scattering from non-Hermitian metasurfaces is associated with branch cut crossing on the complex frequency plane. In this chapter, we report on controlling the spectral positions of topological singularities for electrically-tunable monolayer transition metal dichalcogenide (TMDC) heterostructures so as to actively change their scattering parameters. We use the complex frequency plane trajectories to demonstrate full-2π phase modulation with uniform reflectance, enabling dynamic beam deflection with near-unity diffraction efficiency, and to explore in-plane coupling effects at the surface. Our results can be further extended to explore effects of excitonic resonances on tunable topological platforms for arbitrary wavefront manipulation and exceptional point-based sensing as new directions for active two-dimensional nanophotonics.

Introduction

Over the past decade, substantial advances have been made in artificial materials for active control of light. Optical metasurfaces composed of two-dimensional (2D) arrays of subwavelength scatterers, are particularly promising for light manipulation as they offer control over the amplitude, phase, polarization, and spectrum of light at the subwavelength scale[81–84]. Recently, active metasurfaces are being explored to reconfigurably shape the optical wavefront at high speeds by modulation of the optical permittivity with electrical, optical, thermal, and mechanical mechanisms[27,85–89]. Dynamic wavefront manipulation has been shown with various active materials such as transparent conducting oxides, liquid crystals, phase-change materials, thermo-optic materials, and 2D materials, enabling dynamic beam steering, varifocal lensing, and polarization conversion[6,12,29]. These active

nanophotonic platforms hold promise for comprehensive control of the constituent parameters of light, and hold potential for applications including LiDAR, holographic displays, communication, and computation at optical frequencies. To arbitrarily shape the light wavefront in active devices, dynamic phase modulation over the full 2π-phase range is needed to fully determine the wavefront spatial phase profile. Different physical phenomena and modulation mechanisms have been explored to span the full 2π-phase range in active metasurfaces by exploiting the resonant phase profile of one or coupled modes[90], via gradual phase accumulation in subwavelength waveguides[91,92], and by accumulating Pancharatnam-Berry phase by using anisotropic resonant elements[50,93–95].

Recently, a unified picture for the origin of the 2π-phase modulation in non-Hermitian photonic systems was proposed in the framework of topological phase singularities on the complex frequency plane[96]. It was shown that pairs of zeros and poles of the reflection and transmission matrices are bridged by branch cuts, which when crossing the real frequency axis are associated with the 2π-phase accumulation across the resonance frequency. This observation elucidated the typically observed dynamics in nanophotonic devices close to the critical coupling condition, where the amplitude approaches zero and the phase abruptly jumps across the resonant wavelength[97,98]. For systems whose dynamics can be effectively projected on to the complex frequency plane, these principles provide a valuable roadmap for the exploration of topological singularities and design for optical phase engineering. However, this type of complex frequency analysis approach thus far has mainly focused on passive elements that require modification of their geometry to alter their optical response, with only a few studies of reconfigurable devices that take advantage of external stimuli to actively control the scattering properties[99].

Excitonic materials, such as two-dimensional transition metal dichalcogenides (TMDCs) are promising candidates for exploring gate-tunable topological phenomena in resonant photonic systems. Monolayer TMDCs host exciton resonances that are intrinsic to the material[13,15] and are highly tunable with external electric field or doping[5,100], dielectric environment[17,19], and strain[20,21]. For example, large excitonic reflectivity[9,10], near-unity photoluminescence quantum yield (PLQY)[80], and tunability in the complex refractive

index have been shown by modifying the radiative and nonradiative rates in TMDCs, leading to demonstrations of tunable lensing and dynamic beam steering with patterned monolayer heterostructures[6].

Here, we explore dynamic phase modulation in excitonic TMDC heterostructures, focusing on monolayer molybdenum diselenide ($MoSe_2$), by the projection of their reflectance onto the complex frequency plane. We show how the spectral positions of the topological phase singularities can be actively tuned with gate voltages and carrier density modulation, changing from on- to off-resonant response that completely alter their reflection amplitude and phase. Furthermore, we show that moderate voltage values of ±5 V are sufficient to modulate the branch cuts across the real frequency axis, enabling the full 2π-phase range. By exploring heterostructure configurations composed of two and three $MoSe_2$ monolayers, and gating each monolayer separately, we identify contours of uniform reflectance with full 2π phase coverage. We use these concepts to demonstrate periodic arrays for dynamic beam deflection with near-unity diffraction efficiency. We further explore coupling effects of the unit cells and show how the complex frequency perspective sheds light on preferable voltage configurations to suppress coupling.

Complex Frequency Response of an Excitonic Heterostructure

We first consider a simple structure composed of a monolayer $MoSe_2$ separated from a silver back reflector by an 80 nm hBN spacer layer (Figure 4.1a). To gain insight into the effects of the $MoSe_2$ on the spectral positions of the singularities, we model the complex frequency response of the system to normally incident light tuned to frequencies close to the A exciton resonance. Since only a single exciton resonance is relevant over the frequency range of interest, the dielectric function can be described by a single oscillator parameterized by the exciton resonant energy, radiative, and nonradiative decay rates (see Figure S3.1 and Supplementary Note 3.1). Figure 4.1b shows how the zeros and poles of the system are affected by tuning the individual $MoSe_2$ parameters. For the case of a nearly lossless configuration with negligible radiative and nonradiative losses, the zero and pole will lie close to the real frequency axis. Increasing the radiative rate results in separation

of the zero and pole across the real frequency axis. A blueshift in the exciton resonant frequency will result in a blueshift in the positions of both the zero and pole along the real frequency axis. As nonradiative losses are introduced to the system ($\gamma_{nr} > 0$), the imaginary part of the zero and pole both decreases, and adding gain ($\gamma_{nr} < 0$) increases their imaginary parts.

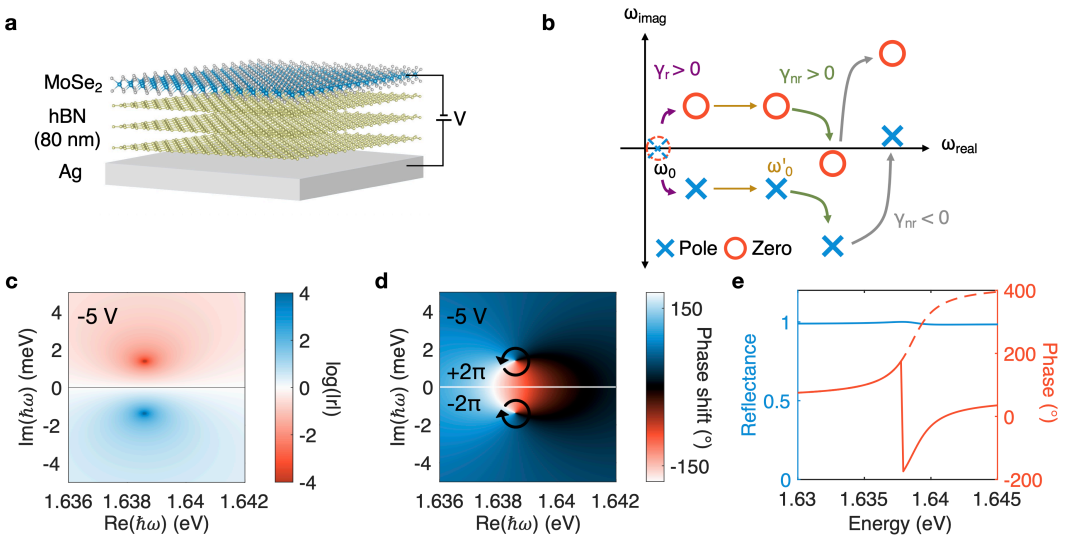

Figure 4.1. Effects of $MoSe_2$ exciton parameters on the complex frequency plane. (a) Schematic of the structure where a monolayer $MoSe_2$ is placed 80 nm on top of a silver back reflector. The 80 nm hBN serves as the spacer layer and gate dielectric. (b) The effects of individually tuning each exciton parameter on the spectral positions of the zeros (red) and poles (blue) in the complex frequency plane. (c) The logarithmic map corresponding to the reflectance amplitude as a function of the real and imaginary parts of the complex frequency. The zero (red) and pole (blue) are on opposite sides of the real frequency axis. (d) The corresponding phase as a function of real and imaginary parts of the complex frequency. Topological phase singularities at the same positions of the zero and pole have opposite winding numbers, resulting in the branch cut crossing the real frequency axis. (e) The real frequency projection of the reflectance amplitude and phase, showing the wrapped (red solid line) and unwrapped (red dashed line) 2π phase difference across the exciton resonance energy.

The spectral positions of the zeros and poles have significant influence over the amplitude and phase profile of the scattered light. Figure 4.1c and 1d show the complex frequency response of the reflectance amplitude and phase, respectively, for $\gamma_{nr} = 0$. We note that the

zeros and poles of the system, shown in red and blue in Figure 4.1c, respectively, are logarithmic branch points where the phase becomes singular. This can be seen in Figure 4.1d where the phase spirals as vortices at the singular spectral positions. In absence of nonradiative loss, the zeros and poles are located on each side of the real axis and the topological charge, q, can be calculated by evaluating the winding number along the contour encircling the singularity $q = \frac{1}{2\pi}\oint_{C_l} \frac{d\phi(\omega)}{d\omega} d\omega$, where q = +1 for the zero and -1 for the pole, corresponding to a phase that varies by 2π around each singularity point with opposite sign. Here, where the zeros and poles are on opposite sides of the real axis, near-unity reflectance with full 2π phase accumulation is obtained as a function of real frequency, shown in Figure 4.1e.

Tunability of Phase Singularities with Carrier Density Modulation

Next, we consider the effects of gating on the positions of the zeros and poles. Previous studies have shown that the refractive index of a monolayer TMDC can be tuned by over 200% by increasing the carrier concentration in $MoSe_2$ heterostructures with gate voltage[20]. This carrier concentration increase results in a combination of Pauli blocking, which blueshifts the exciton energy, and Coulomb scattering, which leads to linewidth broadening from increase in nonradiative processes. Figure 4.2a shows the contour plot of the real frequency phase spectra for varying gate voltages and corresponding electron densities. We note the charge neutral point is set to be -5 V, which is consistent with the voltage values that maximize the neutral exciton reflectance from previous reports of n-doped $MoSe_2$ monolayer flakes (see Figure S3.1 and Supplementary Note 3.1)[5]. For a gate voltage of around -3.8 V (electron density n_e = 3.7 x $10^{11}/cm^2$), we see a topological phase singularity on resonance where the phase is undefined. Line cuts for the reflectance amplitude and phase are shown in Figure 4.2b and 2c, respectively, which show that phase singularity occurs at a voltage value where the reflectance is zero and the phase spectra switches from monotonically increasing to an asymmetric line shape. The corresponding voltage-dependent complex frequency response (Figure 4.2d-2f) elucidates these dynamics observed for real frequencies. Figure 4.2d shows the effects of increasing the voltage and

carrier density on the positions of the zeros and poles of the system, where the exciton resonance blueshifts and the increase in nonradiative losses shifts the imaginary part of the zeros and poles toward the lower half of the complex frequency plane. Figure 4.2e and 2f are the complex frequency phase responses that correspond to voltages of -3.8 V (gray) and -2.5 V (dark blue, n_e = 7.6 x 10^{11}/cm^2), respectively, from Figure 4.2b-2d. Notably, in Figure 4.2f, the singularity lies below the real axis, resulting in minimal phase accumulation for real frequency, shown in dark blue in Figure 4.2c.

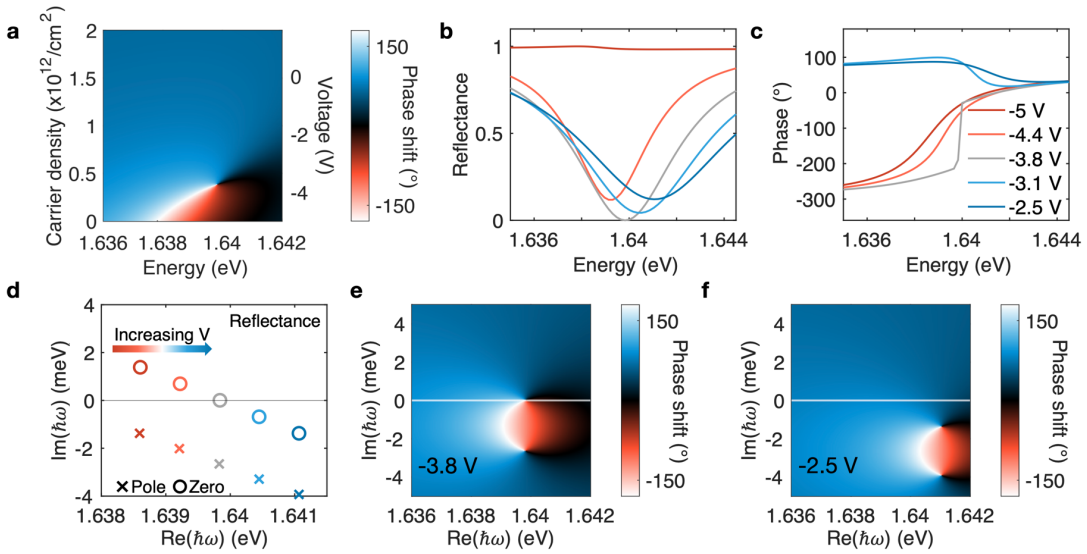

Figure 4.2. Effects of increasing carrier concentration with voltage in monolayer $MoSe_2$. (a) Voltage and spectral dependence of the phase for real frequencies. (b,c) Line cuts for the reflectance and phase profiles, respectively, for different voltages. For V = -3.8 V, the reflectance dip goes to zero and the phase transitions from monotonically increasing to an asymmetric lineshape. (d) The effects of increasing the carrier concentration on the position of the zeros and poles in the complex frequency plane. The color of each pair corresponds to the same voltage values from Figure 4.2b. (e,f) The phase as a function of real and imaginary parts of the frequency for V = -3.8 V and V = -2.5 V, respectively.

It is important to note that in our analysis, we assume the intrinsic photoluminescence quantum yield, defined as $\eta = \gamma_r / (\gamma_r + \gamma_{nr})$, at the $MoSe_2$ charge neutral point is unity. While near unity quantum yields have been reported, there can be a significant variation between different monolayer flakes, and also variation within the same flake due to charge

and strain inhomogeneities[10]. For lower quantum yield where $\eta < 0.4$, the achievable phase modulation range for a single monolayer $MoSe_2$ flake will be limited to π since both the zero and pole will start off in the lower half of the complex frequency plane and increasing carrier concentration will further lower the zero and pole. Thus, in order to achieve above π phase modulation, the quantum yield of the $MoSe_2$ at charge neutral needs to be $\eta > 0.4$, where the zero and pole are on opposite sides of the real frequency axis. Various methods such as superacid treatments or strain engineering have been shown to suppress nonradiative decay mechanisms and improve the quantum yield in TMDCs. We note this balance between radiative and nonradiative rates in exciton resonances is similar to plasmonic resonances in meta-reflectarrays, where the 2π phase shift across the resonant wavelength occurs when the radiative losses exceed absorption losses[101,102]. These observations underscore the valuable insights gained from studying the evolution of zeros and poles in the complex frequency plane and how gate-tunable excitonic systems such as $MoSe_2$ heterostructures may be able to provide a promising platform for studying these behaviors.

Phase Singularities in Multilayer Heterostructures and >2π Phase Modulation

While a single monolayer is sufficient for tuning the singularities, the large covariation of amplitude and phase with voltage is undesirable and the achievable phase shift at a given wavelength will be less than 2π (Figure S3.3). These challenges can be mitigated through introducing additional $MoSe_2$ layers. Similar to plasmonic metasurfaces where uniform reflectance and 2π phase modulation are realized by changing two tunable parameters, each $MoSe_2$ layer introduces an additional pair of singularities that can be individually tuned to facilitate independent control of phase and amplitude[57].

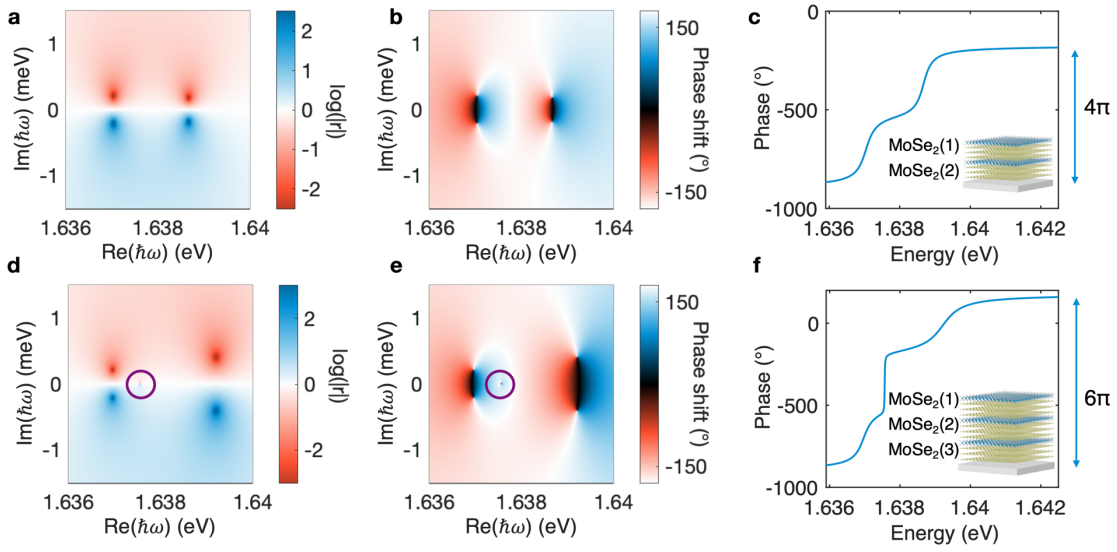

Figure 4.3. Two- and three-layer $MoSe_2$ heterostructures in absence of nonradiative loss. (a) The logarithmic map of the reflectance amplitude and (b) phase for two-layer $MoSe_2$ as a function of the real and imaginary parts of the complex frequency, showing two distinct pairs of zeros and poles. (c) The real frequency phase projection showing 4π phase difference across the resonance. (d) The logarithmic map of the reflectance amplitude and (e) phase for three-layer $MoSe_2$ as a function of the real and imaginary parts of the complex frequency, showing three distinct pairs of zeros and poles. (f) The real frequency phase projection showing 6π phase difference across the resonance. The inset of (c) and (f) show the layer-dependent heterostructure, where the two hBN thicknesses for (a-c) are both 80 nm and the three hBN thicknesses for (d-f) are all 50 nm.

We consider two device heterostructures, one with two $MoSe_2$ layers (Ag / hBN (80 nm) / $MoSe_2$ / hBN (80 nm) / $MoSe_2$), and one with three $MoSe_2$ layers (Ag / hBN (50 nm) / $MoSe_2$ / hBN (50 nm) / $MoSe_2$ / hBN (50 nm) / $MoSe_2$). In the absence of nonradiative loss, a system with two $MoSe_2$ layers has two symmetric pairs of zeros and poles corresponding to each $MoSe_2$ layer, shown in Figure 4.3a. The phase response in the complex frequency plane and the real frequency projection are shown in Figure 4.3b and c, respectively, where we see a 2π phase jump across each resonance. Similarly, by introducing a third $MoSe_2$ layer, the interactions among the three pairs of zeros and poles (Figure 4.3d and e), each associated with an individual $MoSe_2$ layer, result in an additional integer multiple of 2π phase accumulation across the resonant frequency. By comparing Figure 4.3c and 3f, we see a total cumulative 4π phase difference across the resonance for

two layers, and 6π phase difference for three layers, suggesting the potential for beyond 2π phase modulation with varying carrier densities (Figure 4.4). Interestingly, we note that in the three-layer case, the location of the second zero-pole pair (outlined in purple) lies very close to the real axis, corresponding to a steep phase variation and extremely narrow resonance linewidth. This corresponds to a bound mode where interference of the radiation channels gives rise to a high quality factor.

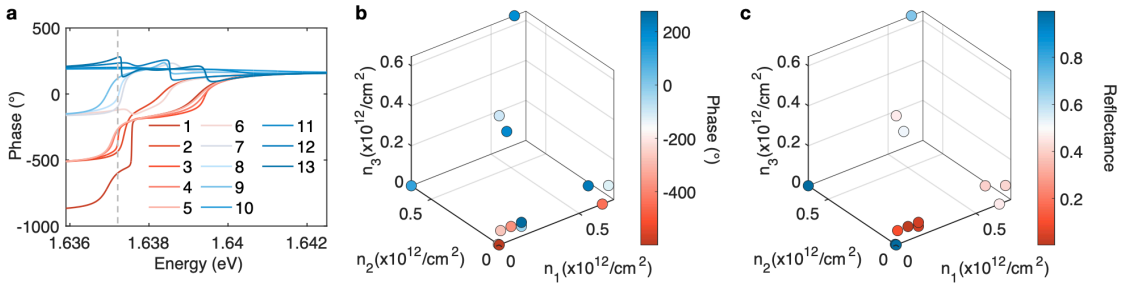

Figure 4.4. Carrier-dependent scattering response for three-layer $MoSe_2$ heterostructure. (a) Phase spectra for different combinations of carrier concentrations in three $MoSe_2$ layers, showing the phase on resonance (E_0 = 1.6372, indicated by the gray dashed line), spanning over 2π. (b) Corresponding reflectance phase and (c) amplitude values on resonance for various carrier concentrations (n_1, n_2, and n_3).

Effect of Spacer Thickness on Energy Eigenmodes

We first consider a single-layer $MoSe_2$ structure, in absence of non-radiative losses, to study the effects of the hBN thickness on spectral positions of the zeros and poles. In the simplistic scenario, one can imagine a cavity formed by a monolayer $MoSe_2$ and silver back reflector separated by air. From Fabry-Perot cavities, we expect to have a reflectance dip when the spacing between the two layers is an integer factor of half the exciton resonant wavelength ($d = \lambda_0/2$), where the reflectivity of the $MoSe_2$ is maximized. Similarly, with the hBN spacer layer, where n_{hBN} = 2.1, we expect the condition at $d = \lambda_0/(2n_{hBN})$ where λ_0 = 756 nm. In Figure 4.5, we see the dependence of the spectral positions of the zeros and poles on the hBN thickness starting from d = 10 nm (black) to d = 225 nm (yellow). Notably, we see roughly around quarter wavelength thickness (purple), the distance between the zeros and poles is $2\gamma_r$. As the thickness increases from quarter-wavelength

thickness (purple) to half-wavelength thickness (orange), the zeros and poles converge onto the real axis, giving rise to a bound state in the continuum mode (BIC). As we continue to increase the thickness from half-wavelength thickness (orange to yellow), we see the positions of the zeros and poles separate and encircle the same trajectory.

We then consider a two-layer $MoSe_2$ structure, shown in Figure 4.6a. As mentioned in the main text, each $MoSe_2$ layer gives rise to a pair of zeros and poles. When the thickness of each hBN layer is roughly quarter-wavelength, the two $MoSe_2$ are strongly coupled (shown in blue in Figure 4.6b and 6c). We can view this as a strongly coupled exciton in a Fabry-Perot cavity system where the distance between the bottom silver back reflector and the top $MoSe_2$ layer are spaced half-wavelength apart, serving as the Fabry-Perot cavity coupled to the middle excitonic $MoSe_2$ layer. As we increase both hBN thicknesses from quarter-wavelength thickness (blue) to half-wavelength thickness (red), both pairs of zeros and poles converge onto the real axis (Figure 4.6d).

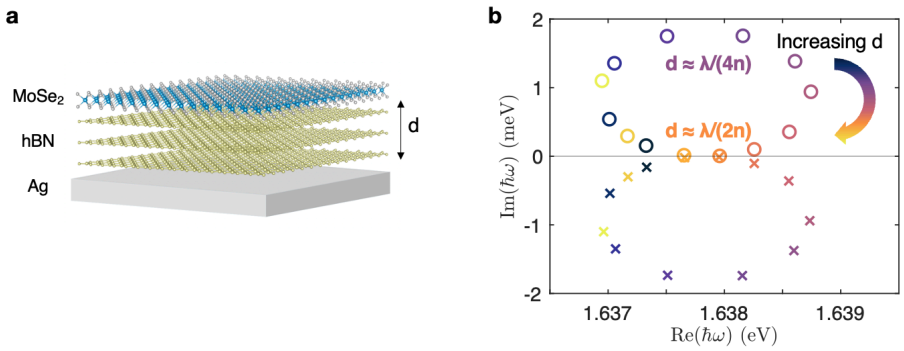

Figure 4.5. Effects of hBN thickness on zeros and poles. (a) Schematic of single-layer $MoSe_2$ structure with arbitrary hBN spacer thickness. (b) Spectral position of the zeros and poles in the complex frequency plane as the thickness increases from d = 10 nm (dark purple), to d = 225 nm (yellow).

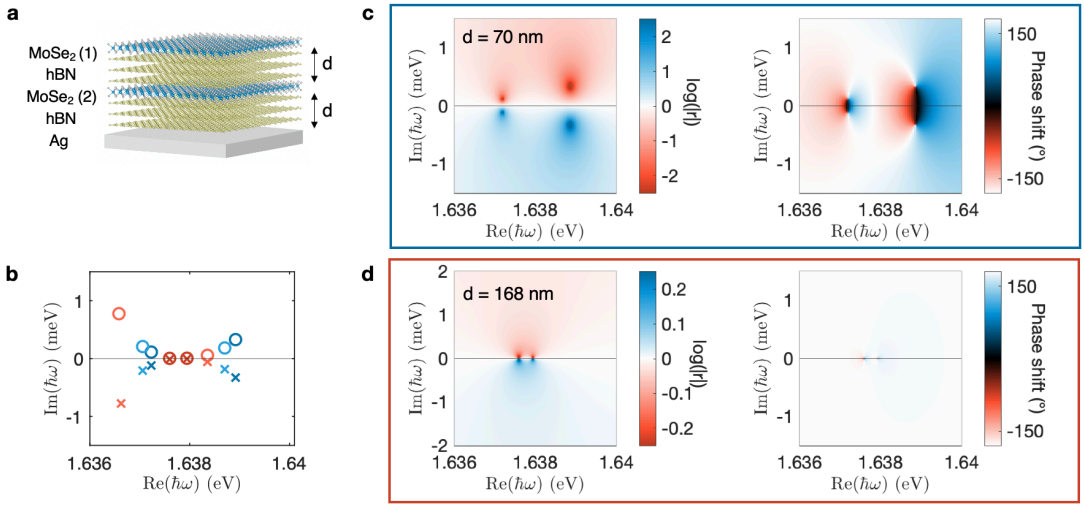

Figure 4.6. Effects of hBN thicknesses on zeros and poles in multi-layer $MoSe_2$ heterostructure. (a) Schematic of two-layer $MoSe_2$ structure with arbitrary hBN spacer thicknesses. (b) Spectral position of the zeros and poles in the complex frequency plane as the thickness increases from d = 70 nm (dark blue), to d = 168 nm (dark red). (c,d) The logarithmic map of the reflectance amplitude and the corresponding phase as a function of the real and imaginary parts of the complex frequency for d = 70 nm and d = 168 nm, respectively.

Far-field Beam Shaping using Multilayer Heterostructures

Following the introduction of the complex frequency behavior of two- and three-layer structures, we use the complex reflectance profiles to explore the associated far-field implications by examining the heterostructure performance for gate-tunable beam steering. Using the same structures from Figure 4.3, we introduce nonradiative losses to the system by increasing the carrier density through gating the $MoSe_2$ layers. Figure 4.7a and b show the reflectance amplitude and phase values on resonance for the two-layer structure as we vary the carrier densities in both $MoSe_2$ layers, which enables us to trace out trajectories of uniform reflectance and full 2π phase modulation. However, one major challenge with current active metasurface design principles is that they suffer from low total reflected power and high absorption losses from operating near resonance. This trade-off between achieving sufficient phase modulation and minimizing absorption loss presents a significant challenge in designing tunable metasurfaces. While Figure 4.7a and b show that

full 2π phase modulation is achievable for two $MoSe_2$ layers, the constant reflectance values are below 10%. However, by introducing a third $MoSe_2$ layer, we can significantly increase the total reflected power to 50% while maintaining the full 2π phase modulation (Figure 4.7c-d).

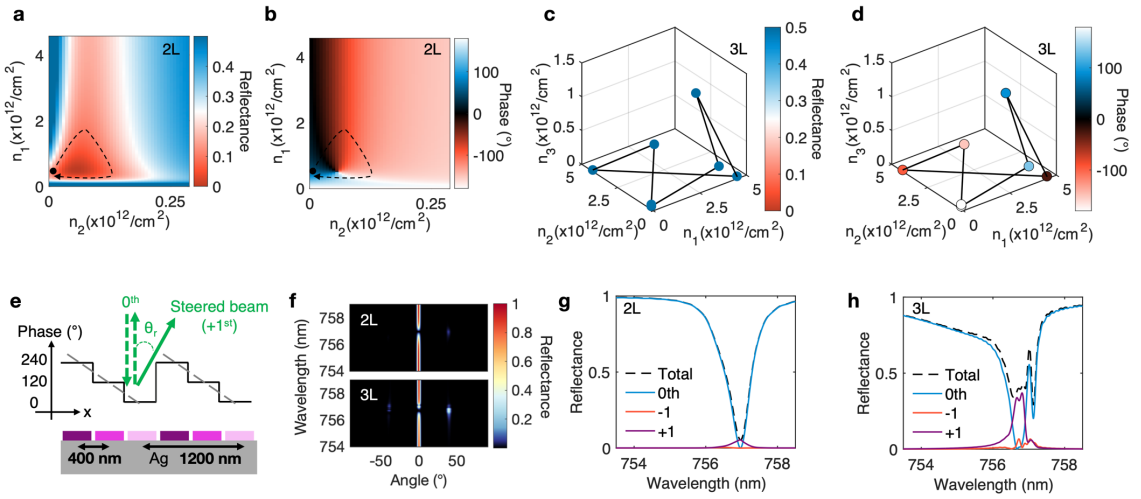

Figure 4.7. Gate-dependent two- and three-layer $MoSe_2$ heterostructures and beam steering. (a) Reflectance amplitude and (b) phase dependence through varying the carrier concentrations (n_1 and n_2) of two $MoSe_2$ layers. The dashed curve shows the trajectory for constant reflectance amplitude and 2π phase modulation. (c) Reflectance amplitude and (d) phase values through varying the carrier concentrations of three $MoSe_2$ layers where the reflectance is constant at 50% and the phase spans 2π. (e) Schematic of the simulated structure for dynamic beam steering. The different shades of purple correspond to different carrier concentration configurations in both the two- and three-layer structure where the phase shifts are spaced apart by 120°. The linearly decreasing phase gradient deflects the scattered light to the +1 order. (f) Simulated far-field response for two-layers (top) and three-layers (bottom) where the light is deflected to the +1 order (39°) at the exciton resonance λ = 756.7 nm. (g) The reflected power into the 0 (blue), -1 (red), and +1 (purple) orders for the two-layer and (h) three-layer structure. The total reflectance (black dashed line) indicates that near λ = 756.7 nm, most of the reflected light results from the +1 order for both the two-layer and three-layer structure, but the reflected power into the +1 order is significantly higher for the three-layer structure.

Using the carrier concentration values from Figure 4.7a-d, we performed full wave electromagnetic simulations (Lumerical FDTD) to identify phase conditions suitable for dynamic beam steering. The refractive index of the $MoSe_2$, which is determined by the carrier concentration and voltage, is periodically modulated in the x direction at a

subwavelength scale to control the wavefront of the reflected light. Imposing a constant phase gradient on the reflected wavefront then deflects the scattered light to a desired angle, as shown schematically in Figure 4.7e. Using a three-level blazed grating phase profiles with relative phase of 0°, 120°, and 240°, we demonstrated beam steering to angles of 39° at an operating wavelength of λ = 756.7 nm for both two layers and three layers $MoSe_2$ configurations (Figure 4.7f). Here, the spacing between adjacent $MoSe_2$ elements are p = 400 nm, with a super-cell period of d = 1200 nm. Comparing the diffraction steering efficiency and total reflected power of a tunable metasurface using two layers (Figure 4.7g) and three layers (Figure 4.7h), we can achieve over 90% efficiency for both configurations (Figure S3.5a). These high values are attributed to the phase profile covering the prescribed values of 0°, 120°, and 240°. However, the three layers system demonstrates notably higher total deflected power of over 35% (Figure 4.7h), compared to 5% for two layers (Figure 4.7g) due to the difference of reflection amplitudes.

Complex Frequency Analysis for Minimizing Coupling Effects

The design of metasurfaces for wavefront manipulation involves defining the local scattering properties along the surface by choosing the building blocks that possess the required amplitude and phase response. These building blocks are typically extracted from simulations of either isolated unit cells or periodic structures extended to infinity in-plane, as we have adopted in this paper. However, when placed in a different photonic environment, in-plane coupling affects the scattering properties and results in a modified optical response of the metasurface. In certain situations, the coupling effects are desired and can even give rise to a variety of highly attractive optical phenomena[66–74], but for wavefront control, they often distort the shaped wavefront and result in lower efficiencies of the structured far-field patterns. Different strategies have been employed to compensate for coupling effects, including inverse designs, local phase methods, and perturbative methods using the design viewpoint of nonlocal modes[84,103]. In the following, we use the complex frequency domain perspective to examine suppression of the wavefront distortion due to the in-plane optical interactions.

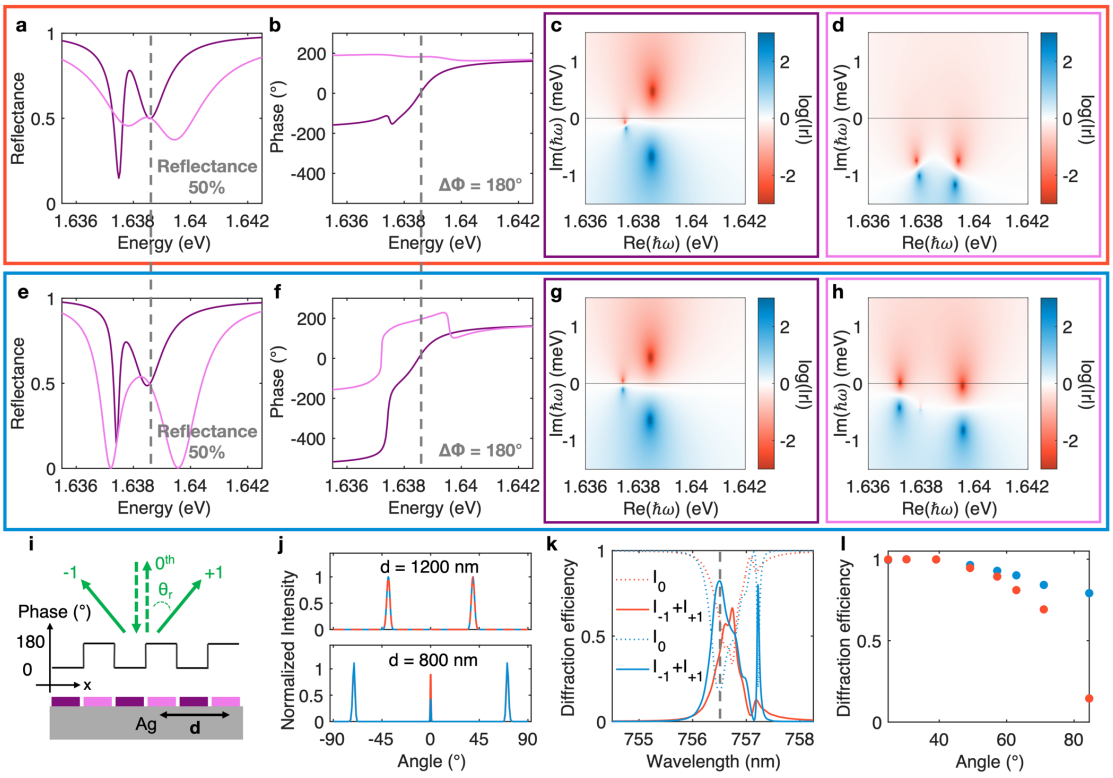

Figure 4.8. Beam deflection for two-level phase grating in three-layer $MoSe_2$ heterostructures. (a) Reflectance amplitude and (b) phase for the first set of carrier concentration configurations. At the resonance energy (gray dashed line), the two configurations give a reflectance value of 50% and a phase difference of 180° (c,d) The corresponding logarithmic map of the reflectance amplitude as a function of real and imaginary part of the complex frequency for the first set of configurations (dark purple and pink), respectively. (e) Reflectance amplitude and (f) phase for the second set of carrier concentration configurations. At the resonance energy (gray dashed line), this second set of configurations also gives a reflectance value of 50% and a phase difference of 180° (g,h) The corresponding logarithmic map of the reflectance amplitude as a function of real and imaginary part of the complex frequency for the second set of configurations (dark purple and pink), respectively. (i) Schematic of the simulated structure for beam deflection to ± 1 orders. The dark purple and pink corresponds to different configurations from Figure 4.8a-d and Figure 4.8e-h that give a phase difference of 180°. (j) Intensity of the electric field in the far field for a two-level phase grating for d = 1200 nm (top panel), and d = 800 nm (bottom panel). (k) Comparison of the spectrally resolved diffraction efficiency for the two sets of carrier concentration configurations for d = 800 nm. (l) Diffraction efficiency as a function of deflection angle, determined by the period d according to $\sin(\theta) = \lambda/d$. As the deflection angle increases (i.e., decreased period size), the diffraction efficiency decreases.

In our case, the coupling between different elements at the surface becomes particularly critical when selecting voltage-dependent carrier concentration trajectories for beam shaping. Specifically, in the case of the three-layer structure, different trajectories with identical complex reflectance values, but corresponding to different carrier concentration configurations, will exhibit the same far-field diffraction in the hypothetical case when no coupling effects are considered. However, they can display significantly different profiles when coupling is considered. To delve into this effect, we consider a two-level phase grating where the phase shift between neighboring elements is 180° but the amplitude is constant. Figure 4.8a and b show the reflectance amplitude and phase profiles for two distinct carrier concentration configurations in the three $MoSe_2$ layered structure (Figure 4.3f inset). The carrier concentration combinations are $n_1 = 45 \times 10^{11}/cm^2$, $n_2 = 0.13 \times 10^{11}/cm^2$, $n_3 = 0.46 \times 10^{11}/cm^2$ (shown in dark purple), and $n_1 = 1.9 \times 10^{11}/cm^2$, $n_2 = 45 \times 10^{11}/cm^2$, $n_3 = 3.3 \times 10^{11}/cm^2$ (shown in pink). At the targeted energy denoted by the gray dashed lines, E = 1.6386 eV (λ = 756.7 nm) the different configurations give rise to the same reflectance amplitude and phase shift value. The corresponding complex frequency planes for the reflectance amplitudes are shown in Figure 4.8c and d. In Figure 4.8e and f, we show the spectra for a different set of carrier concentration configurations, where $n_1 = 23 \times 10^{11}/cm^2$, $n_2 = 0.13 \times 10^{11}/cm^2$, $n_3 = 0.07 \times 10^{11}/cm^2$ (shown in dark purple) and $n_1 = 1.1 \times 10^{11}/cm^2$, $n_2 = 1.6 \times 10^{11}/cm^2$, $n_3 = 0.33 \times 10^{11}/cm^2$ (shown in pink), and the corresponding complex frequency plane in Figure 4.8g and h. Notably, this second set of configurations also gives rise to a phase difference of 180° and 50% reflectance on resonance (gray dashed line). Symmetry considerations suggest that a two-level phase grating with 180° phase shift between neighboring elements should create full suppression of all even diffraction orders, particularly the zeroth order.

To examine the effects of near-field coupling on the diffraction efficiencies, we perform full-wave simulations of the two-level phase grating metasurface. Specifically, the geometry was determined according to the studied three-layer structure and the voltage configurations used in Figure 4.8 (a)-(d) and (e)-(h). We varied the coupling influence by scanning the periodicity *d,* which determines the deflection angle θ according to

$\sin(\theta) = \pm\lambda/d$ for the ± 1 diffraction orders (see Figure 4.8i for a schematic diagram). For a periodicity of d = 1200 nm, where the diffraction angle is θ = 39°, we see both sets of configurations (shown in red and blue in top panel of Figure 4.8j) give rise to unity deflection efficiency. However, as the period size decreases and the deflection angle increases (d = 800 nm, θ = 71°), we observe a noticeable difference in the deflection efficiency between the different carrier concentration configurations. In the bottom panel of Figure 4.8j, the first set of configurations (red) gives rise to an undesired substantial 0^{th} order reflection with similar intensity as the +1 and -1 order beam, whereas the second set of configurations (blue) shows larger suppression of the 0^{th} order beam, corresponding to a 15% difference in the diffraction efficiency. The second configuration outperforms the first one over the entire spectral range of the resonance (Figure 4.8k). Hence, as the period of the metasurface decreases and the deflection angle increases, the coupling strength between neighboring elements increases and results in a noticeable decrease in the diffraction efficiencies. While this occurs for both sets of configurations, the effect is more prominent for the first configuration (red), as demonstrated by the plot of diffraction efficiency vs the angle (Figure 4.8l). Specifically, for small angles (<40°), the diffraction efficiency is near unity for both configurations, but at 84° the difference is 65%. The disparities are elucidated by considering the complex frequency planes of the different voltage and carrier concentration configurations of neighboring metasurface elements, i.e., between Figure 4.8c and d and between Figure 4.8g and h, where the change in the spectral positions of zeros and poles in Figure 4.8g and h appear less abrupt than the change in Figure 4.8c and d. This difference suggests that the effects of near-field coupling depend not only on the real frequency reflectance amplitude and phase values, but more importantly, the spectral positions of the zeros and poles in the complex frequency plane.

Conclusion

In summary, we explore active tunability of the spectral positions of topological phase singularities associated with excitonic resonances in two-dimensional materials heterostructures, specifically the zeros and poles, in the complex frequency plane and their impact on far-field beam shaping. We present one- to three-layer TMDC heterostructures

as platforms for dynamically controlling the topological singularities through tuning the TMDC exciton resonances with voltage and carrier concentration. Each TMDC layer introduces a pair of zeros and poles, and each branch cut crossing results in an additional 2π phase accumulation across the exciton resonance. By manipulating multiple pairs of singularities in the multi-layer TMDC structure, we enable 2π phase modulation with uniform reflectance, allowing for efficient beam steering. Moreover, we suggest how the complex frequency plane can be used for reducing effects of near-field coupling between neighboring elements in metasurfaces. The effects of the spectral positions of zeros and poles on the tunable phase coverage, steering efficiency, and near-field coupling underscore the need for the complex frequency response to be considered as an additional parameter in the design of dynamic nanophotonic devices.

CHAPTER 5: EXCITONS IN COLLOIDAL QUANTUM DOTS FOR EMISSION AND PHASE MODULATION

Colloidal quantum dots (QDs) are promising excitonic materials that exhibit bright, pure, and tunable photoluminescence, making them highly attractive for next-generation display, lighting, and sensing technologies. Their high photoluminescence quantum yield (PLQY) at room temperature and scalable fabrication processes with spin-coating enable their integration over large areas. However, the potential of QDs for metasurface-based applications, particularly for phase modulators, remains underexplored. This chapter investigates the optical properties of QDs and their potential for phase modulation, contrasting them with the previously explored excitonic materials like transition metal dichalcogenides. By examining the role of exciton linewidth and radiative efficiency, this chapter aims to provide insights into the advantages and challenges of using QDs for active metasurface applications.

Introduction

Excitons in low-dimensional materials such as transition metal dichalcogenides (TMDCs) have emerged as promising candidates as active materials for metasurface-based applications due to their tunable strong light material interactions. In previous chapters, monolayer molybdenum diselenide ($MoSe_2$) was explored for refractive index modulation, phase modulation, and beam steering. While excitons in TMDCs, such as $MoSe_2$, have demonstrated great potential for active control of light, their practical applications are limited by their low radiative efficiency at room temperature and small monolayer flake area.

Colloidal quantum dots provide a promising alternative as they exhibit high radiative efficiencies at room temperature. Moreover, their optical properties are tunable through size and chemical composition, and they can be spin-coated for large area, scalable fabrication. The photophysical properties of QDs have been studied extensively to support a wide range of technological applications beyond light emitting devices, including

biomarkers, environmental sensors, biomedical markers[104], environmental sensors[72], photodetectors[105], and photovoltaics[106]. Despite their advantages, achieving gate-tunable phase modulation with QDs presents remains unexplored. Here, we examine the voltage-controllable optical properties of QDs, investigate exciton gating mechanisms, and analyze theoretical and experimental limitations of using QDs for phase modulation.

Optical Properties of Quantum Dots

We first measure the photoluminescence (PL) spectrum and characterize the PLQY of our quantum dots. A microscope image of a drop casted QD film on a silicon substrate and the PL spectrum are shown in Figure 5.1a and 5.1b, respectively. The PL spectrum exhibits a peak emission at 615 nm with a 32 nm linewidth and an extracted PLQY of ~60% from normalizing the PL of the QD film to a barium sulfate sample. We note that while the PLQY of our quantum dots are not near-unity, they are higher than the room temperature quantum yields demonstrated in monolayer TMDs over a large area. Nevertheless, a number of factors can contribute to the low PLQY in our quantum dot film. Figure 5.2 shows a schematic illustration of the various radiative efficiency loss (quenching) mechanisms in a QD, some of which we can then leverage for tuning the exciton resonance through gating. Here we give an overview of these factors:

1. An electric field can reduce the electron-hole wavefunction overlap of the exciton, thus decreasing the radiative recombination rate.
2. Increased exciton dissociation rate at high electric fields.
3. A defect state can act as an intermediate center for nonradiative recombination.
4. Excess charges can lead to charged excitons which typically have low PLQY due to Auger recombination.
5. Energy transfer via Forster resonance energy transfer FRET can funnel excitons into dark states.

Each of these processes introduces nonradiative pathways that compete with radiative recombination, affecting the PL and optical properties under gating or external perturbations. By adjusting the oscillator strength in QDs, modifying nonradiative

relaxation pathways, or changing the local optical density of states, active control of the QD PL can be achieved.

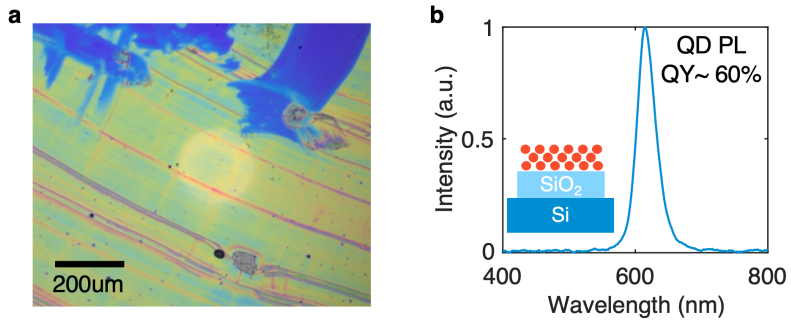

Figure 5.1. Photoluminescence quantum yield of colloidal quantum dots. (a) Microscope image of a drop-casted film of QDs. (b) Photoluminescence spectrum of a QD film with a measured quantum yield of 60%.

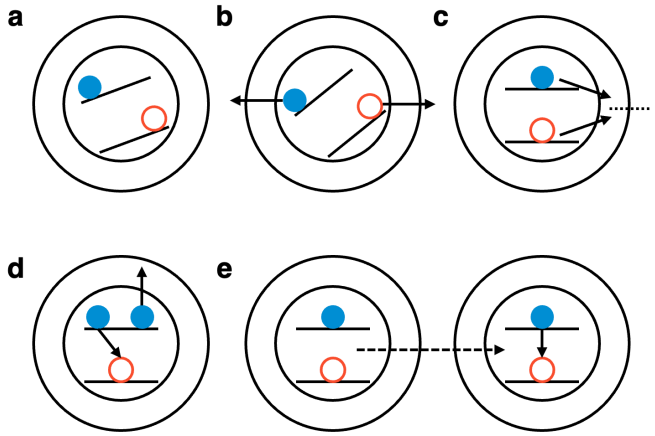

Figure 5.2. Schematic of different loss mechanisms in with QD excitons. (a) Reduced electron-hole wavefunction overlap with an applied electric-field. (b) Exciton dissociation at high electric-fields. (c) Defect-assisted nonradiative recombination. (d) Auger recombination. (e) Energy transfer to a "dark" sites via FRET.

Exciton Modulation from Field Induced Quenching

To explore the tunability of QD excitons, we first study a capacitor-like device stack which allows us to apply an electric field across the QD film without charge injection from

electrodes. The main effect of applying an electric field on the absorption and emission properties is the quantum confined stark effect (QCSE), which describes three closely related phenomenon. First, the electron and holes shift toward lower energies, which leads to a redshift in the exciton peak. Second, the wavefunction of the electron and hole becomes spatially separated, reducing the radiative recombination rate (longer lifetime) and the PLQY. Lastly, the nanocrystal symmetry is altered and can lead to new absorption and emission bands that are previously forbidden. In addition to the effects of QCSE, an application of an electric field can also result in inhomogeneous broadening due to distribution of QD orientation and anisotropic polarizability[107], Auger recombination, modified coupling between exciton and phonon modes, increased nonradiative recombination rates from coupling between delocalized band edge and surface trap states[108], reduced exciton binding energy[109], and exciton dissociation.

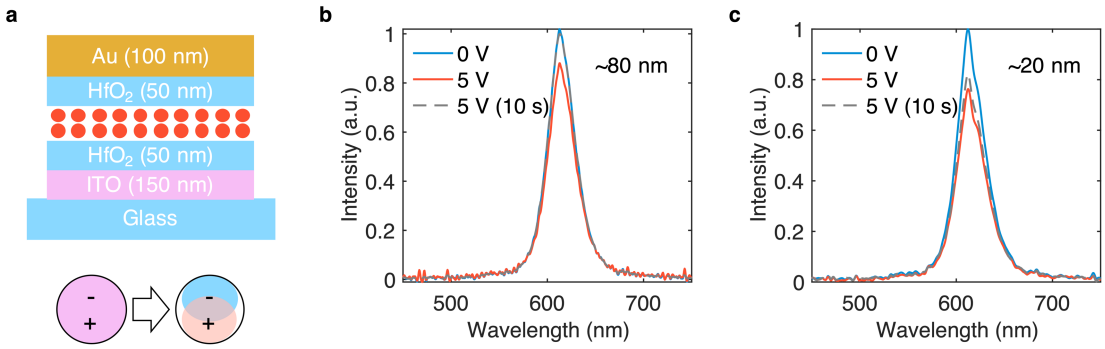

Figure 5.3. Photoluminescence modulation with voltage in a capacitor structure. (a) Schematic of the capacitor structure with a QD layer sandwiched between HfO_2 dielectric layers. (b,c) Photoluminescence of an 80 nm and 20 nm QD layer, respectively, with an applied voltage of 0 V (blue) and 5 V (red and gray). The red line indicates the PL spectrum taken immediately after applied voltage and the gray line is taken 10 seconds later, while still under applied bias.

Our device stack, shown in Figure 5.3a, consists of spin-coated layer of CdSe-CdS QDs sandwiched between two 50 nm hafnium dioxide (HfO_2) dielectric layers on a 150 nm ITO sputtered on glass substrate. Two QD film thicknesses, 80 nm and 20 nm, are studied in this section. The HfO_2 layers are deposited using atomic layer deposition (ALD), as it is important that the QD PL quenching is minimized during the fabrication process,

specifically when putting down the layers on top of the quantum dots. The ITO and 100 nm of evaporated gold are used as the bottom and top electrodes, respectively.

To study the PL quenching dynamics in the capacitor structure, we first perform steady-state PL measurements under 405 nm excitation and applying a bias to the device, from 0 V to 5 V. Figure 5.3b and 5.3c show the PL under 5 V bias for the 80 nm and 20 nm QD films, respectively. Unsurprisingly, we observe a lower amount of quenching for the thicker 80 nm QD device (12%) compared to the 20 nm QD device (22%) under the same applied bias. However, we note that while an immediate reduction in PL intensity is observed upon voltage application, a gradual recovery in the PL (gray dashed line) occurs over the time scale of seconds while the QD is under applied bias. Particularly for the thicker QD film, the PL spectra under 5 V after 10 s almost completely overlaps with the 0 V spectra (blue line), whereas this transient effect is less prominent in the thinner QD film. Since these dynamics occur on timescales of seconds, we suspect there is charge trapping in the device or photogenerated charges that may screen the external electric field, thereby reducing the amount of field induced quenching. In fact, even at zero field, previous works have shown single QD blinking due to photogenerated carriers that are formed on a localized state residing on the surface of the QD or the matrix surrounding it[110,111]. On an ensemble level, these excess charges could contribute to electric field screening[112,113].

Exciton Modulation from Direct Charge Injection

In addition to exciton modulation from field induced quenching, we can also control charge induced quenching through directly injecting charges into the QD layer[112]. Our full device stack, shown in Figure 5.4a, consists of a 20 nm spin-coated layer of CdSe-CdS QDs on a 150 nm ITO sputtered on glass substrate. Since the QD is in direct contact with the ITO conductor, we observe ~20% PL quenching in absence of an applied bias compared to the QD on glass (Figure 5.4b). We then ALD a 50 nm HfO_2 layer on top of the QD film as a gate dielectric, and evaporate 100 nm gold.

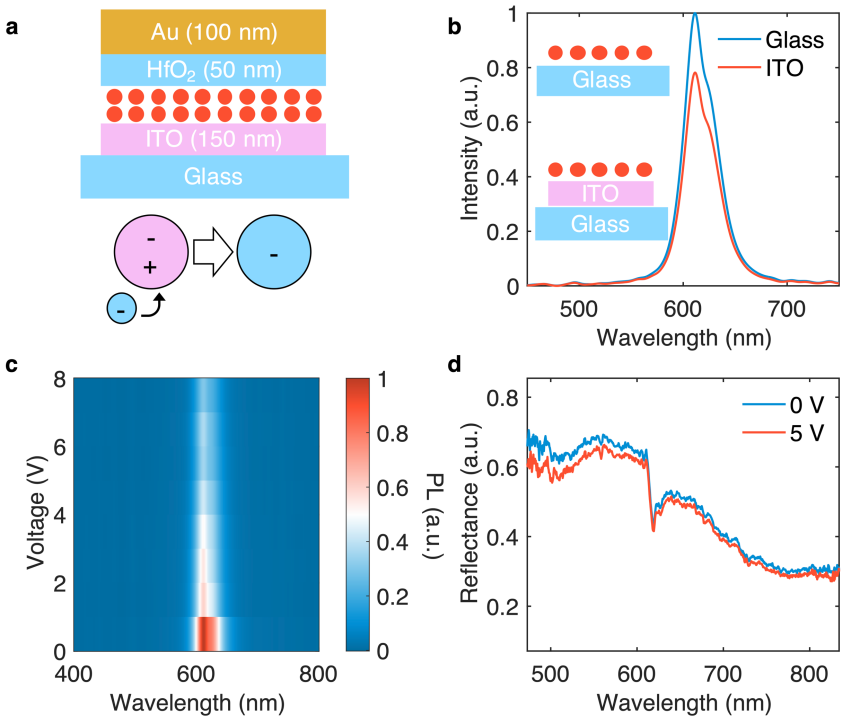

Figure 5.4. Photoluminescence modulation with voltage through charge injection. (a) Schematic of the structure with a QD layer directly on top of an ITO bottom electrode. (b) Photoluminescence with the QD on glass compared to the QD on ITO. (c) Modulation of the PL with applied voltage showing a reduction of the PL intensity down to 25%. (d) Reflectance spectrum with and without voltage, showing minimal reflectance change.

By applying a bias between the bottom ITO and top gold electrode, we can study the effects of direct charge injection to the quantum dot PL. Figure 5.4c shows the gate dependent PL as we apply a bias from 0V to 8V. Notably, we see a much stronger PL quenching of up to 75% in this configuration compared to the capacitor structure in the previous section. However, while the PL spectra show clear quenching under gating, the reflectance spectra (Figure 5.4d) remain largely unaffected by gating. It is important to note that the reflectance dip around 600 nm is due to the cavity interference effects, not the excitons in the QD, as this dip is also observed off the QD film.

Limitations of Excitons in Quantum Dots for Amplitude and Phase Modulation

The gated QD device structures studied in this chapter reveal that while PL modulation from excitons can be observed, reflectance modulation is minimal, suggesting limited

phase modulation despite the higher quantum yield compared to TMDCs. This is seemingly contradictory since in Chapters 2, 3, and 4, we showed how the achievable refractive index and phase modulation is directly tied to the quantum yield of the exciton in TMDCs, with a higher quantum yield resulting in larger reflectance amplitude and phase modulation range with applied voltage. While the PL from the excitons in TMDCs and QDs are both highly tunable, there are key differences in the exciton physics that could shed light on why we do not observe reflectance and phase modulation in the quantum dots despite the high PLQY.

First, we consider the origins of the excitons quantum dots and how they differ from excitons in TMDCs. One of the unique properties of colloidal QD is their size-tunable emission color due to physical confinement in all three-dimensions, governed by quantum confinement effect, as opposed to confinement in just the perpendicular direction in 2D TMDCs. Specifically, when the quantum dot radius is smaller than the material's Bohr radius, the energy levels can be approximated by considering the QD as a particle in a sphere with infinite potential walls (Figure 5.5a). As a result, only certain states that satisfy the boundary conditions are allowed, leading to the quantization of bulk energy levels. By applying the effective mass approximation and modeling the conduction and valence band as parabolic, the QD exciton energy is given by:

$$E_{exciton} = E_g + \frac{\hbar^2}{2a^2}\left(\frac{\beta^2_{n_e l_e}}{m_e} + \frac{\beta^2_{n_h l_h}}{m_h}\right) - \frac{1.8e^2}{4\pi\epsilon a}$$

where the first term E_g is the bandgap of the bulk semiconductor. The middle two terms account for the quantum confinement energies of the electron and holes and are dependent on the size of the QDs. As the dimension of the QDs decreases, the confinement becomes stronger, resulting in an increase in the exciton energy, corresponding to a size tunable emission wavelength from red to blue. The last term corresponds to the first order Coulomb interaction of the exciton, where the 1.8 factor assumes the electron and hole are in their lowest excited state. For CdSe, the bulk bandgap is E_g = 1.74 eV and the CdSe quantum dots has a size tunable exciton energy up to 2.8 eV (Figure 5.5b). However, we note that

the simple parabolic band approximation allows us to relate the QD size to exciton energy, it doesn't take into account the degenerate band-edge exciton states. This results in the lowest energy exciton state as a "dark" state[114], which is optically inactive, and the Stokes shift between the exciton absorption and emission energy.

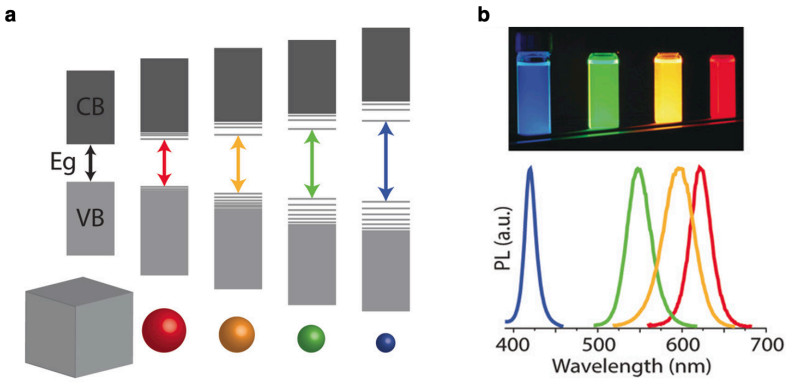

Figure 5.5. Quantum dot exciton resonance energy dependence on size. (a) Schematic of electronic band structures of nanocrystals from bulk to QDs with decreasing size. (b) Image of the fluorescence of the QDs with different sizes (top) along with their corresponding PL spectra (bottom). Adapted from Panfil et al.[115]

Moreover, unlike in TMDC samples where we are limiting our measurements to a monolayer region of a single flake, the QD sample is measured across an ensemble of dots. Variations in size of individual QDs inevitably leads to inhomogeneous broadening of the bandgap. Previous works have shown that the ensemble effects can broaden the linewidths by over 70 meV[116]. Even if this ensemble-level broadening is minimized by yielding monodispersed QD sizes, the single QD linewidths are broadened by exciton-phonon scattering, fine-structure splitting[116], and optical phonon scattering[117].

In addition to the inhomogeneous broadening from ensemble effects caused by variations in QD sizes, another difference between QD and TMDCs is that the dielectric function at the QD exciton energies cannot be modeled by just a simple Lorentz oscillator characterized by the radiative and nonradiative rate. While this model is a good approximation for TMDCs, an effective media approximation (EMA) is needed for modeling the QD dielectric function[118]. Figure 5.6 shows the real and imaginary part of a

CdSe/CdS film, adapted from Dement et al.[118] using both the Maxwell Garnett approximation and Bruggeman approximation models. In the Maxwell Garnet model, it is assumed the spheres are well-separate in a host material and is modeled by[119]:

$$\frac{\tilde{\epsilon} - \tilde{\epsilon}_s}{\tilde{\epsilon} - 2\tilde{\epsilon}_s} = f_{QD} \frac{\tilde{\epsilon}_{QD} - \tilde{\epsilon}_s}{\tilde{\epsilon}_{QD} - 2\tilde{\epsilon}_s}$$

where f_{QD} is the volume fraction of the QDs and $\tilde{\epsilon}_{QD}$, $\tilde{\epsilon}_s$, and $\tilde{\epsilon}$ are the complex dielectric functions for the QD, surrounding ligands and free space, and the overall composite, respectively. The Bruggeman approximation makes no distinction between the QD and surroundings, and is modeled by[120]:

$$f_{QD} \frac{\tilde{\epsilon}_{QD} - \tilde{\epsilon}}{\tilde{\epsilon}_{QD} - 2\tilde{\epsilon}} + f_s \frac{\tilde{\epsilon}_s - \tilde{\epsilon}}{\tilde{\epsilon}_s - 2\tilde{\epsilon}} = 0$$

where f_s is the volume fraction of the surroundings. Both approximations provide a good match to the refractive index obtained by ellipsometry. However, compared to the refractive index in TMDCs, the QD exciton oscillators features are broader and more "smeared out" due to the inhomogeneous broadening effects from the distribution of exciton energies and the combination with the host matrix.

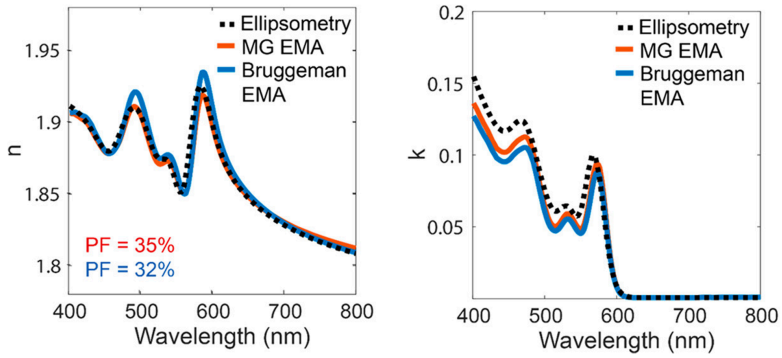

Figure 5.6. The real and imaginary part of the refractive index for a thin film of quantum dots. Adapted from Dement et al.[118]

While the ensemble effects may limit the potential for QD excitons to be independently used for reflectance and amplitude phase modulators (Figure 5.7a-c), we can embed the

QD film with optical resonators to enhance the light-matter interactions. To demonstrate the potential of using QD as an active material for tunable device applications, we propose a simple planar optical cavity where we place a 20 nm QD layer sandwiched between a 50 nm top SiO_2 layer and 58 nm bottom SiO_2 layer in a gold cavity (Figure 5.7d). The thickness of the top gold layer is 30 nm. To calculate the gate-dependent phase shift of the planar structure, we use the transfer matrix method and model the QD refractive index with the values provided in Figure 5.6 for the "Excitons On" (blue line in Figure 5.7e and 5.7f) and remove the oscillators for "Exciton Off" (red line). As shown in Figure 5.7f, we are able to obtain a phase shift of over 80° near the exciton wavelength.

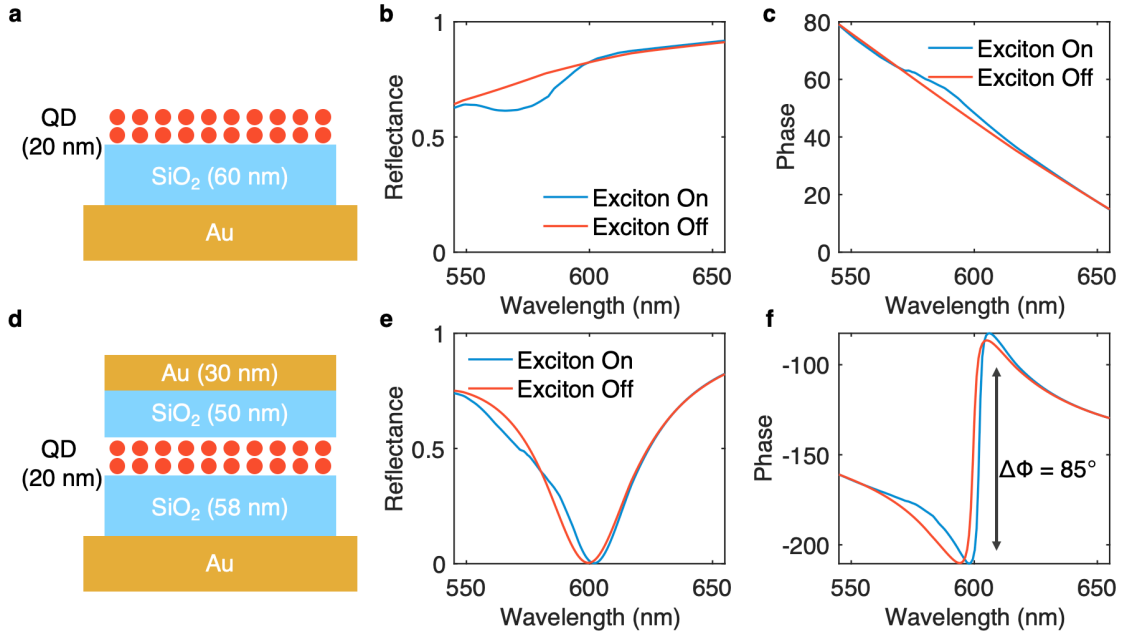

Figure 5.7. Quantum dots in a planar cavity. (a) Schematic of the calculated structure with a gold back reflector and a SiO_2 spacer layer. (b) Calculated reflectance spectra and (c) corresponding phase with and without the exciton oscillators showing minimal phase shift. (d) Schematic of the calculated structure with gold reflectors. The QD layer sandwiched between two spacer layers of SiO_2. (e) Calculated reflectance spectra and (f) corresponding phase with and without the exciton oscillators showing over 85° phase modulation.

Conclusion

In this chapter, we show how QDs offer advantages such as high radiative efficiency and scalable large area fabrication over TMDCs and demonstrate large tunability of 75% in the photoluminescence. However, their potential for reflectance amplitude and phase modulation is limited due to inhomogeneous broadening. We present a way to overcome these challenges by embedding the QD layer with an optical cavity to obtain 85° phase modulation. Further exploration of hybrid systems, for example combining QDs with TMDCs or other excitonic materials, could leverage the strengths of both material platforms, enabling a broader range of functionalities for active metasurfaces.

CHAPTER 6: CONCLUSIONS AND OUTLOOK

Summary

In this thesis, we demonstrate how novel light-matter interactions in excitonic nanomaterials, specifically transition metal dichalcogenides (TMDCs) and quantum dots, provide new mechanisms for controlling light at the nanoscale. We introduce ways that exciton resonances in these materials can be tuned and how the tunability can enable dynamic wavefront shaping, highlighting their potential for ultrathin light modulators. We start by characterizing the gate-tunable optical properties of a monolayer TMDC, specifically $MoSe_2$, and show 200% modulation in the real and imaginary part of the refractive index. This large index modulation gives rise to both amplitude and phase modulation of the reflected light, which is then used to apply an electrically tunable phase gradient across a single monolayer flake to dynamically steer the reflected beam. These experimental results are purely from tuning the strong intrinsic exciton resonances in the TMDC, without the need to couple to external optical resonators. We then present a theoretical analysis of the complex frequency amplitude and phase response of a generalized excitonic heterostructure for metasurface applications. We show how the spectral positions of the topological phase singularities, e.g. zeros and poles, of an excitonic heterostructure can be dynamically controlled, their impacts on the real frequency phase response, and how they can be used in active metasurface design. Finally, we evaluate quantum dots as an alternative platform for emission and phase modulators since they exhibit high radiative efficiencies at room temperature. We present key differences between excitons in quantum dots and TMDCs and how they present different challenges in designing phase modulators with quantum dots.

Future Research Directions

Building on the work presented in this thesis, here we present exciting avenues to explore that allows us to harness the full potential of excitonic materials for active metasurfaces.

Transmissive metasurface with cascaded excitonic heterostructure

Our demonstrations of tunable reflectance amplitude and phase in TMDCs suggest that next steps could focus on designing transmissive metasurface. In general, active metasurfaces in transmission face design challenges compared to reflection, where a reflective back mirror could help achieve larger phase shifts. However, in transmissive metasurfaces, the wave must pass through the metasurface, which requires more intricate amplitude and phase engineering in order to maintain reasonable transmission efficiency while obtaining sufficient phase modulation. Excitonic materials could be promising since tuning their intrinsic exciton resonances can give rise to phase modulation in transmission.

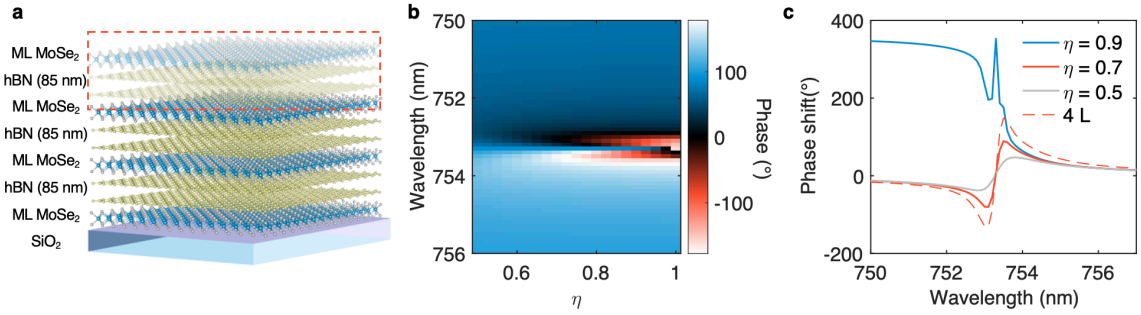

Figure 6.1. Cascaded $MoSe_2$ monolayers for phase modulation in transmission. (a) Schematic of the heterostructure showing multiple cascaded monolayers on a transparent substrate. (b) Transmittance phase spectra as a function of radiative efficiency for three cascaded monolayers. (c) Line cuts of the phase spectra for η = 0.5, η = 0.7, η = 0.9 for three monolayers (solid lines) and four monolayers (red dashed line) for η = 0.7.

Here we propose an excitonic heterostructure structure based on cascaded monolayers of $MoSe_2$ (Figure 6.1a). As shown in Figure 6.1, with radiative efficiencies η>0.5, we can observe noticeable phase modulation in transmission. Moreover, as we cascade additional monolayers of TMDs (red dashed line), we can further increase the achievable phase modulation range in transmission, which is in good agreement with what we have observed in reflection from (Chapter 4).

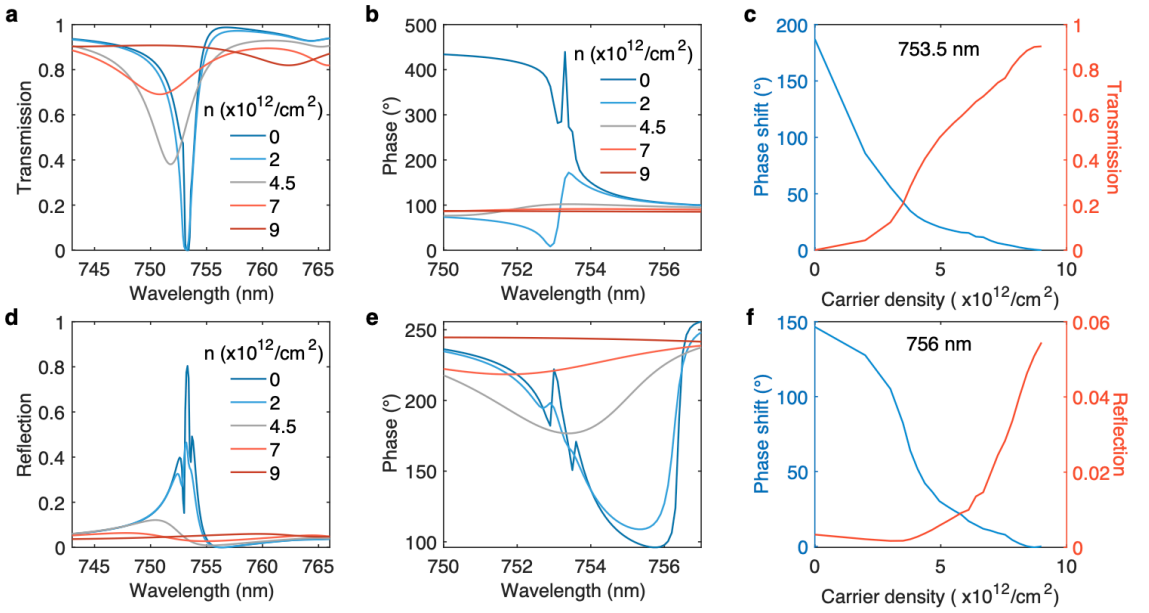

Figure 6.2. Transmission and reflection amplitude and phase modulation for three-layer heterostructure. (a) Transmission amplitude and (b) phase spectra for different carrier densities. (c) Amplitude and phase modulation with carrier density at a working wavelength of 753.5 nm for transmission. (d) Reflection amplitude and (e) phase spectra for different carrier densities. (f) Amplitude and phase modulation with carrier density at a working wavelength of 756 nm for reflection. Both transmission and reflection spectra are calculated with the same heterstructure.

Interestingly, in the case where η=0.9, we observe a large amplitude and phase shift of over 140° in both transmittance (Figure 6.2a-c) and reflectance (Figure 6.2d-f) even though our structure was designed to maximize transmittance phase shift. This unique property can be attributed to the fact that tuning a single exciton resonance in a TMDC sheet simultaneously gives both reflectance and transmittance phase modulation. To highlight the potential for wavefront shaping, we perform far-field simulation by applying a phase gradient across the TMDC heterostructure (Figure 6.3a). We see that under the same applied phase gradient, both the transmittance and reflectance beam can be steered (Figure 6.3b and 6.3c, respectively). We note that the reflectance steering efficiency is much lower since the phase gradient was applied to maximize the steering efficiency in transmission. Nevertheless, our preliminary results show the versatility of leveraging exciton resonances for wavefront shaping in both transmission and reflection.

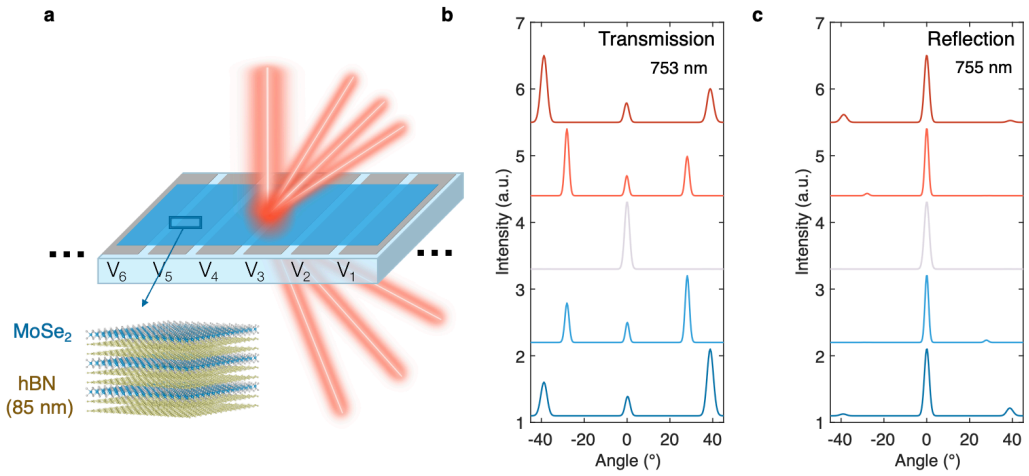

Figure 6.3. Beam steering in both transmission and reflection in a cascaded excitonic heterostructure. (a) Schematic of the metasurface structure used for FDTD simulations. (b) Demonstration of beam steering in transmission to angles ±39° at 753 nm. (c) Similarly, the reflected beam can also be steered to ±39° at a different wavelength, 755 nm.

Quasi-bound states in the continuum (Q-BIC) resonant enhancement of radiative rate in $MoSe_2$

While our previous studies involved leveraging the strong intrinsic material resonances in monolayer TMDCs in absence of coupling to external cavities, radiative decay engineering also emerges as a promising solution by enhancing the radiative decay rates of excitons via the Purcell effect. Given that 2D materials can be naturally integrated into various types of optical cavities without the constraints of lattice matching, the photonic environment can be optimized for enhancing the light-matter interactions. Here, we present the effects of enhancing exciton radiative emission rates in $MoSe_2$ coupled to high Q cavities on the gate-tunable reflectance amplitude and phase. Noting that the enhancement of an emitter scales as $\Gamma \sim Q/V$, where Q is the quality factor and V is the mode volume, there is often a trade-off between the two when designing a resonator. Recently, Q factors up to 1000 have been shown in a single subwavelength resonator that support quasi-BIC modes[121]. The resonant structure is based on a cylinder that utilizes the destructive interference between optical modes to obtain a significant increase in the Q factor of the nanoresonator. Thus, the

emission rate and linewidth of monolayer $MoSe_2$ can be enhanced by integration with a metasurface composed of subwavelength AlGaAs cylinders that support quasi-BIC modes.

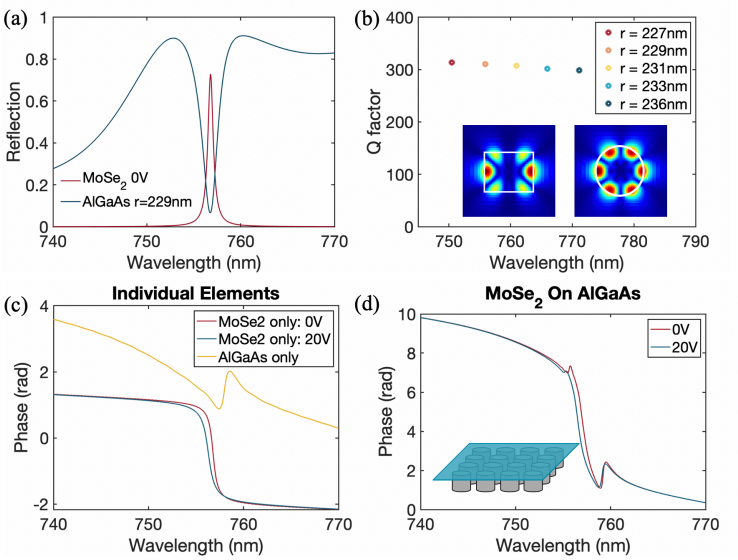

Figure 6.4. Effects of Purcell enhancement of $MoSe_2$ coupled to Q-BIC nanoresonators on phase modulation. (a) Reflection off the $MoSe_2$ (red) and $Al_{.20}Ga_{.80}As$ cylinder that supports a quasi-BIC mode (blue). (b) Quality factor of cylindrical resonators with a fixed height of 330 nm and different radii, corresponding to different resonant energy. (c) Reflection phase profile of the AlGaAs cylinder and $MoSe_2$ at 0V and 20V. (d) Reflection phase profile of the coupled system, showing a much larger phase difference across resonance.

We design a single $Al_{.20}Ga_{.80}As$ Mie resonators that supports a mode with a Q factor of over 300. While the Q factor is modest, the nanocylinder size is only 330 nm in height and 485 nm in diameter with a resonant wavelength of 755 nm, corresponding to a low size-to-wavelength ratio of 0.6. Through varying the radius of the cylinder, the resonant energy of the cylinder can be tuned to the A exciton energy of $MoSe_2$, as shown in Figure 6.4a and b. Then, with an $MoSe_2$ radiative efficiency of 80%, the achievable gate-dependent phase shift of the reflected light can be doubled by coupling the monolayer $MoSe_2$ to an array of these nanoresonators compared to a freestanding monolayer (Figure 6.4c and d). This work suggests that exploring resonant nanophotonic structures that offer large Purcell factors in addition to the intrinsic material resonances is a viable path to realizing devices with high efficiency.

Outlook

Despite rapid progress in manipulating light with 2D semiconductors, achieving high-performance optical functions remains a challenge, especially for large-area devices at room temperature. A few fundamental challenges emerge as compared to conventional metasurface building blocks. Since excitonic resonances play a key role in the light manipulation, these challenges can also be understood and analyzed from the exciton band diagram. First, the resonant frequency of the exciton resonance is dictated by the band structure of the chosen 2D semiconductors, and therefore is not designed at will. While band structure alterations can be achieved either chemically by chemical compound synthesis, physically engineering strain, or changing the dielectric environment, these are still limited to a specific wavelength range. An outstanding challenge for future research is harnessing materials design and preparation to tailor exciton resonances at desired frequencies over a wide range while also maintaining the pristine material quality needed to achieve coherent light-matter interactions at room temperature.

Second, in excitonic materials, the tunability is reduced rapidly when gradually increasing the operation temperature from cryogenic to room temperature, where undesired phonon-assisted nonradiative decay and dephasing processes start outpacing the radiative decay. Since the amplitude and phase modulation are directly linked to the optical resonances of the excitonic materials, the low radiative efficiencies observed at room temperature limit device performance, e.g. diffraction and focusing efficiencies. Thus, a key objective is to identify van der Waals materials and preparation methods with high radiative efficiency at room temperature or above. Engineering of phonon-assisted processes will be instrumental to achieve this. For example, it has been shown that the KK to KQ intervalley exciton-phonon scattering could be reduced significantly by relatively moving the Q valley up by applying a few percent strain to the material, and superacid treatments are reported to successfully improve the quantum efficiency of excitons by removing the defect states.

Photonic environment engineering also emerges as a promising solution to enhance the excitation and radiative decay rate of excitons by boosting the local optical density of states

(the Purcell effect). Creating environments that minimize carrier-carrier scattering while still enabling strong light-matter interactions require high areal densities of excitons that interact weakly to minimize decoherence. Nevertheless, attempts to harness these beneficial effects at the device level are still in their infancy. Finally, it is worth noting that the scattering pattern from the excitonic resonance is also limited to dipole/current sheet radiation due to its atomically-thin nature. More complicated scattered radiation distributions that give rise to highly directional scattering, for example, could possibly be realized in the future through the 3D integration of multiple 2D semiconductor sheets containing 'exciton pockets' that interact coherently.

A range of extrinsic challenges also come into view during the initial attempts to integrate 2D semiconductors in scalable solid-state devices. In order to achieve atomically thin flat optics with complete wavefront control, ongoing advances in scaling the production of high-quality 2D materials are needed to further improve the tuning performance. Although recent development of wafer-scale 2D semiconductor growth is encouraging, those works have mainly focused on optimizing the electronic charge transport properties of the material, while its optical properties still need to be improved to match the quality of the tape-exfoliated pristine materials. Critical electrical engineering challenges associated with 2D semiconductors also need to be addressed before approaching high-performance solid-state gating devices. For instance, the development of high-quality, uniform high-dielectric gate insulators that can be integrated with 2D semiconductors is central for obtaining robust and substantial carrier injection for efficient optical modulation. The defect generation in 2D semiconductors during gate insulator atomic layer deposition should be minimized to maintain the exciton scattering efficiency and avoid Fermi-level pining and hysteresis effects in the charge injection process. Alternatively, a more ambitious solution is to develop a wafer-scale multi-layer hBN growth technique and the associated robotic assembly of van der Waals solids. The contact resistance also needs to be minimized via properly choosing contact materials, such as semi-metals like bismuth and graphite, to fully realize the high-speed modulation potential of these platforms.

As structures for controlling light become increasingly complex, the need for new materials that can exhibit unique light-matter interactions in the ultra-thin limit is rapidly growing. The successful integration of 2D materials into scalable practical devices will allow a range of dynamic optical elements for light-field manipulation and information processing at the speed of light.

APPENDIX A: S1. SUPPORTING INFORMATION FOR CHAPTER 2

Material and Methods

Device Fabrication

Samples were fabricated by mechanically exfoliating hBN, graphene, and monolayer $MoSe_2$ from bulk crystals (hq-graphene and 2D semiconductors) onto polydimethylsiloxane (PDMS) stamps using blue Nitto tape. Electrical contacts on SiO_2(285nm)/Si(500 μm) were written with electron beam lithography at an acceleration voltage of 100 keV and a beam current of 1nA (area dosage of 1350μC/cm^2), developed in MIBK:IPA 1:3 for 1 minute and then rinsed in IPA for 30s (followed by blow dry with N2). Metal (Ti/Au 5nm/95nm) was evaporated at 0.5Å/s and 1Å/s respectively, at a base pressure of 7e-8 Torr. The graphene/hBN/$MoSe_2$/hBN heterostructure was then sequentially transferred from the PDMS to the SiO_2/Si using the all-dry transfer technique. Thicknesses of the flakes were estimated from the optical contrast and confirmed with atomic force microscopy (Asylum Research).

Carrier Density Calculation

We calculate the carrier density by using a simple parallel plate capacitor model. In the device, the bottom hBN is the dielectric capacitor, which enables the formation of a two-dimensional electron gas at the $MoSe_2$ monolayer. Hence, the capacitance is calculated as follows:

$$C = \frac{\epsilon_0 \epsilon_{hBN} A}{d} = \frac{Q}{\Delta V}$$

where, C = capacitance, ϵ_0 = vacuum permittivity, ϵ_{hBN} = relative dielectric permittivity of hBN[122] (ϵ_{hBN} = 4.7), A = area of the capacitor, d = thickness of the hBN flake, and Q is the charge. Thus, the charge density for electrons can be calculated from the capacitance per unit area between the graphene gate and the sample by:

$$n_e = \frac{Q}{A} = \frac{C}{A} * (V - V_{CNP})$$

where the charge neutral point, V_{CNP} = -2.5 V, is the gate voltage that maximizes the exciton absorption, which corresponds to a flat-band condition. In our gating schematic, shown in Figure 1, when $V_g < V_{CNP}$, the sample is hole doped and for $V_g > V_{CNP}$, the sample is electron doped.

PL and Reflectance Measurements

Temperature-dependent optical spectroscopy was performed using an attoDRY800 system, which allows for low temperature control. The sample was mounted on a piezo-stage using Apiezon thermal grease and the stage was cooled by closed-cycle circulating liquid helium. A vacuum and low temperature compatible attocube objective (LT APO VISIR, NA = 0.82) was used to focus a white light source (SLS 201L – Thorlabs) for reflectance measurements and a 532 nm fiber-coupled laser for PL measurements onto the sample. Both the reflectance and PL spectra were taken using a 150 grooves per mm grating-based spectrometer (Silicon CCD) from Princeton Instruments HRS300.

For the temperature and gate dependent reflectance measurements, we normalize the spectra of the monolayer to the spectrum off the gold electrode. The normalized spectra for 4K is shown in Figure 2 in the main text and the spectra for 50 K, 100 K, and 150 K are shown in Figure S1-S3, where the spectrum corresponding to -6V shows the absolute reflectance values and the spectra at higher voltages are offset for clarity.

Transfer Matrix Calculation for Reflectance and Phase

The reflectance and phase of multi-layer thin films can be treated with the transfer matrix method to account for the multiple reflections in our device. At normal incidence, we consider a single polarization of the electric field. The field in each layer can be decomposed into forward and backward traveling waves that form the basis and can be computed by matrix multiplication where each matrix describes the light propagation at an interface between two dielectrics. The $(i+1)^{th}$ amplitude can be related to the i^{th} amplitude by the relation:

$$\underbrace{\begin{pmatrix} e^{ik_i z_i} & e^{-ik_i z_i} \\ k_i e^{ik_i z_i} & -k_i e^{-ik_i z_i} \end{pmatrix}}_{M_1} \begin{pmatrix} A_i \\ B_i \end{pmatrix} = \underbrace{\begin{pmatrix} e^{ik_{i+1} z_i} & e^{-ik_{i+1} z_i} \\ k_{i+1} e^{ik_{i+1} z_i} & -k_{i+1} e^{-ik_{i+1} z_i} \end{pmatrix}}_{M_2} \begin{pmatrix} A_{i+1} \\ B_{i+1} \end{pmatrix}$$

$$\begin{pmatrix} A_{i+1} \\ B_{i+1} \end{pmatrix} = J_i \begin{pmatrix} A_i \\ B_i \end{pmatrix} \; where \; J_i = M_2^{-1} M_1$$

$$\Rightarrow J_i = \frac{1}{2} \begin{pmatrix} e^{i(k_i - k_{i+1}) z_i} \left(1 + \frac{k_i}{k_{i+1}}\right) & e^{-i(k_i + k_{i+1}) z_i} \left(1 - \frac{k_i}{k_{i+1}}\right) \\ e^{i(k_i + k_{i+1}) z_i} \left(1 - \frac{k_i}{k_{i+1}}\right) & e^{-i(k_i - k_{i+1}) z_i} \left(1 + \frac{k_i}{k_{i+1}}\right) \end{pmatrix}$$

where k is the wavevector, z is the thickness, and i is the layer index. The wavevector k_i is scaled by the complex index of refraction $\tilde{n}_i = n_i + i\kappa_i$ of the material so that $k_i = \frac{2\pi \tilde{n}_i}{\lambda}$. Then, for a stack consisting of N layers, we have:

$$\begin{pmatrix} t \\ 0 \end{pmatrix} = J_{N_{total}} \begin{pmatrix} 1 \\ r \end{pmatrix}, \quad where \quad J_{N_{total}} = J_N J_{N-1} \ldots J_2 J_1$$

and the reflectance and phase of the entire stack given by:

$$r = |r| e^{i\phi} \Rightarrow R = |r|^2.$$

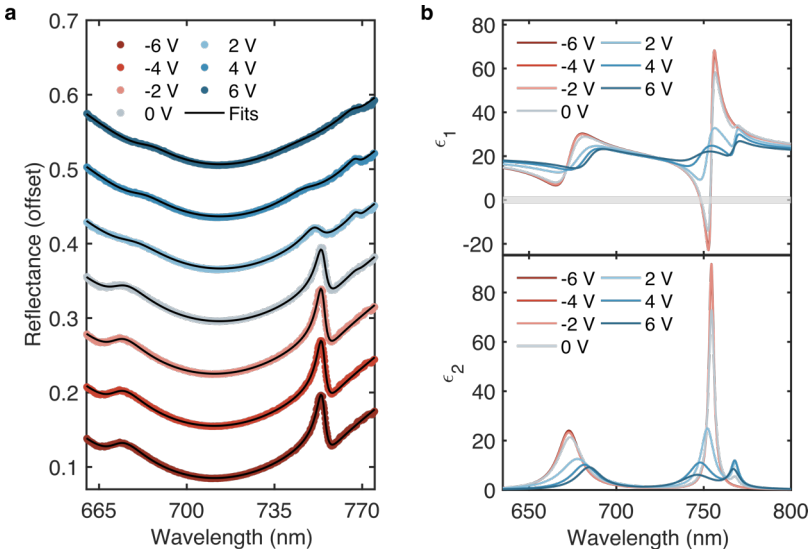

Figure S1.1. Gate-dependent reflectance spectra and refractive index at T = 50 K. (a) Reflectance spectra of monolayer $MoSe_2$ at 50 K for different gate voltages. The colored points are experimental data and solid black lines are fits from transfer matrix calculations where the $MoSe_2$ dielectric function is modeled using the multi-Lorentzian model. (b) Fitted real (ϵ_1) and imaginary (ϵ_2) part of the dielectric function at different voltages.

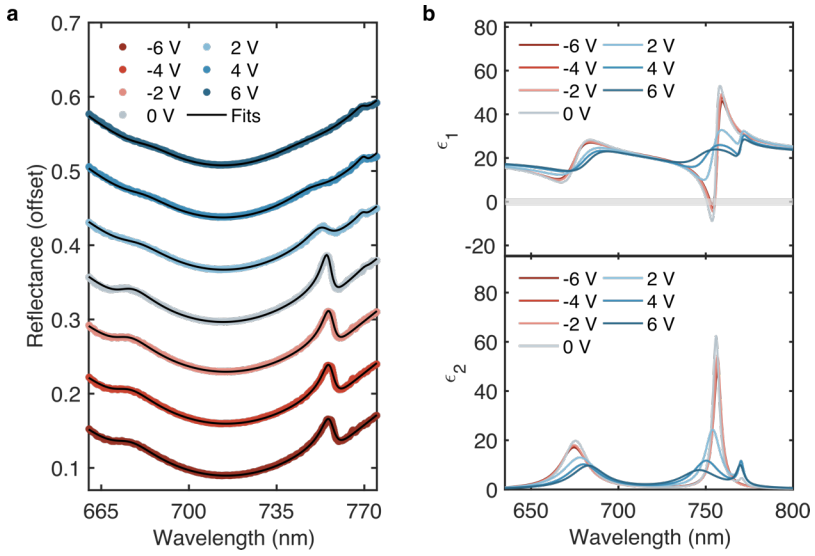

Figure S1.2. Gate-dependent reflectance spectra and refractive index at T = 100 K. (a) Reflectance spectra of monolayer $MoSe_2$ at 100 K for different gate voltages. The colored points are experimental data and solid black lines are fits. (b) Fitted real (ϵ_1) and imaginary (ϵ_2) part of the dielectric function at different voltages.

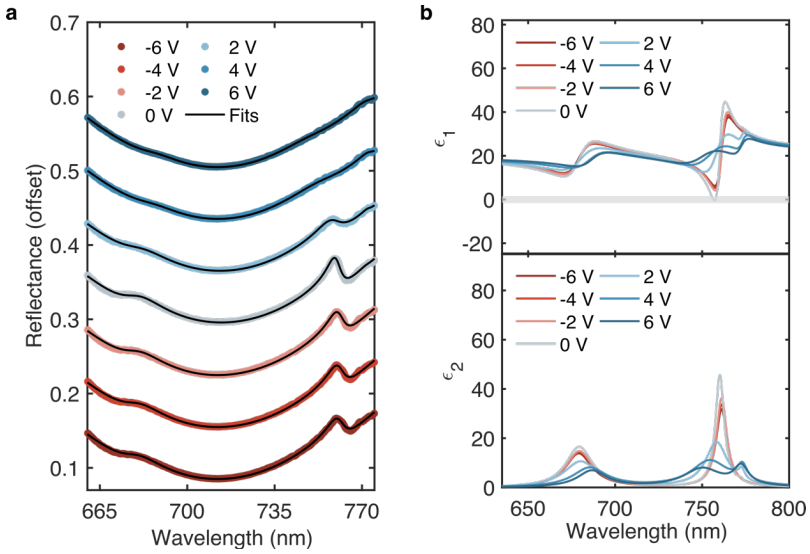

Figure S1.3. Gate-dependent reflectance spectra and refractive index at T = 150 K. (a) Reflectance spectra of monolayer $MoSe_2$ at 150 K for different gate voltages. The colored points are experimental data and solid black lines are fits. (b) Fitted real (ϵ_1) and imaginary (ϵ_2) part of the dielectric function at different voltages.

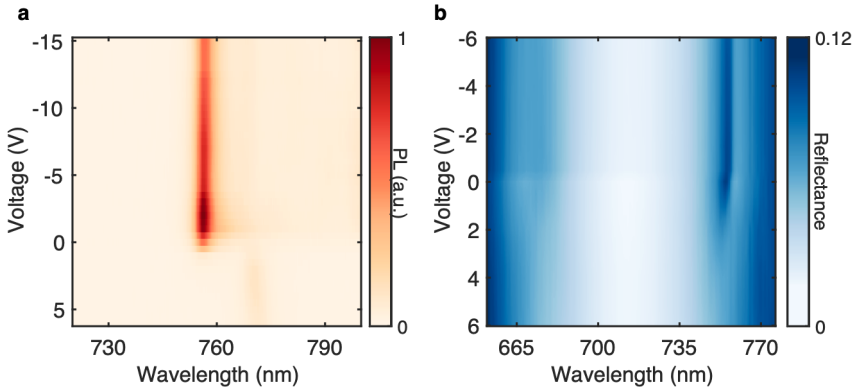

Figure S1.4. Characterization of $MoSe_2$ heterostructure at T = 100 K. (a) Gate-dependent PL spectra showing a prominent peak corresponding to the A exciton around 757 nm and a lower intensity peak corresponding to the trion around 771 nm. (b) Gate-dependent reflectance spectra on the same device with two peaks corresponding to the A exciton at 756 nm and B exciton at 677 nm.

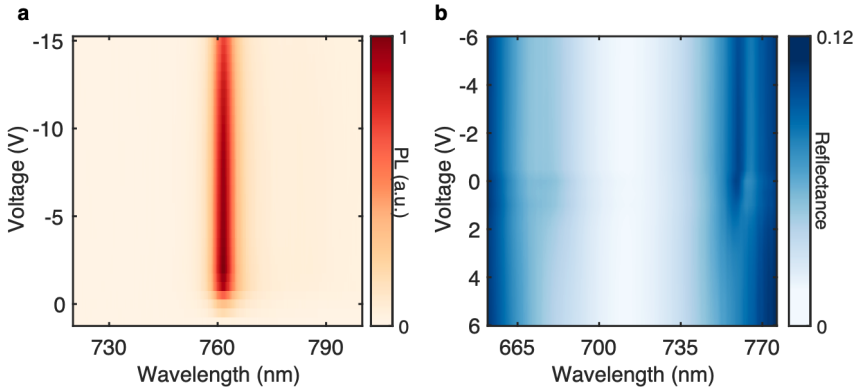

Figure S1.5. Characterization of $MoSe_2$ heterostructure at T = 150 K. (a) Gate-dependent PL spectra showing a distinct peak corresponding to the A exciton around 762 nm. The trion peak is no longer observed. (b) Gate-dependent reflectance spectra on the same device with a peak corresponding to the A exciton at 762 nm and a less prominent peak for the B exciton at 680 nm.

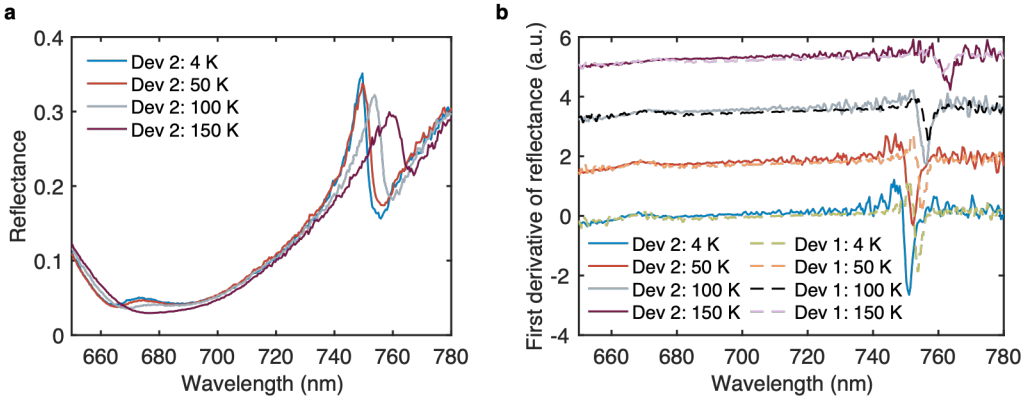

Figure S1.6. Reproducibility of results with another device. (a) Reflectance spectra on sample 2 for different temperatures. (b) First derivative of reflectance spectra for sample 2 (Dev 2) and the gated device studied in the manuscript (Dev 1). Both samples show similar temperature dependent trends in the A and B exciton linewidths and peak shifts.

APPENDIX B: S2. SUPPORTING INFORMATION FOR CHAPTER 3

Supplementary Figures

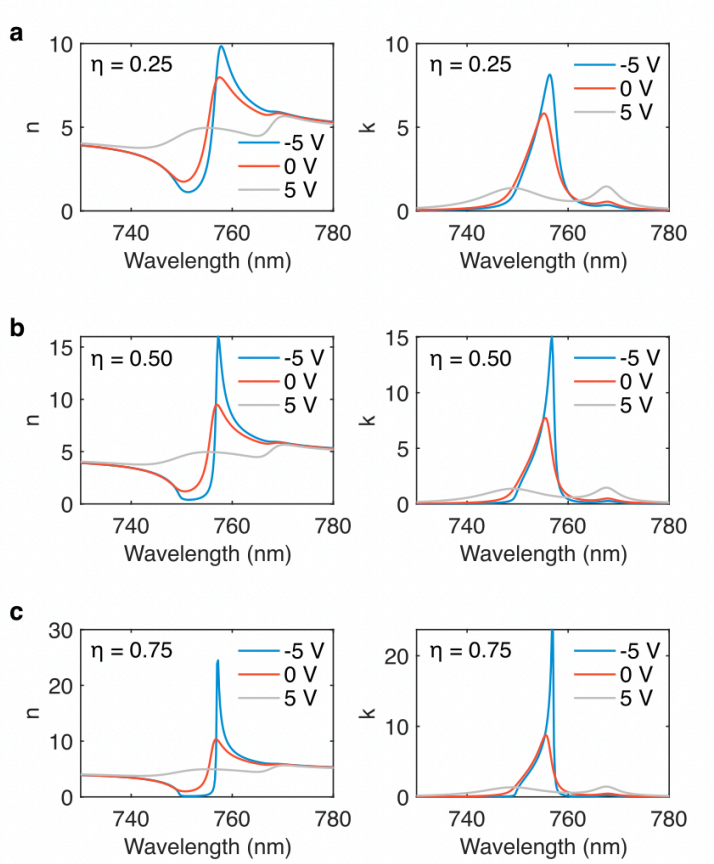

Figure S2.1. Voltage-dependent real and imaginary refractive index. Calculated real and imaginary refractive index of $MoSe_2$ for quantum yields of (a) $\eta = 0.25$, (b) $\eta = 0.5$ (c) $\eta = 0.75$.

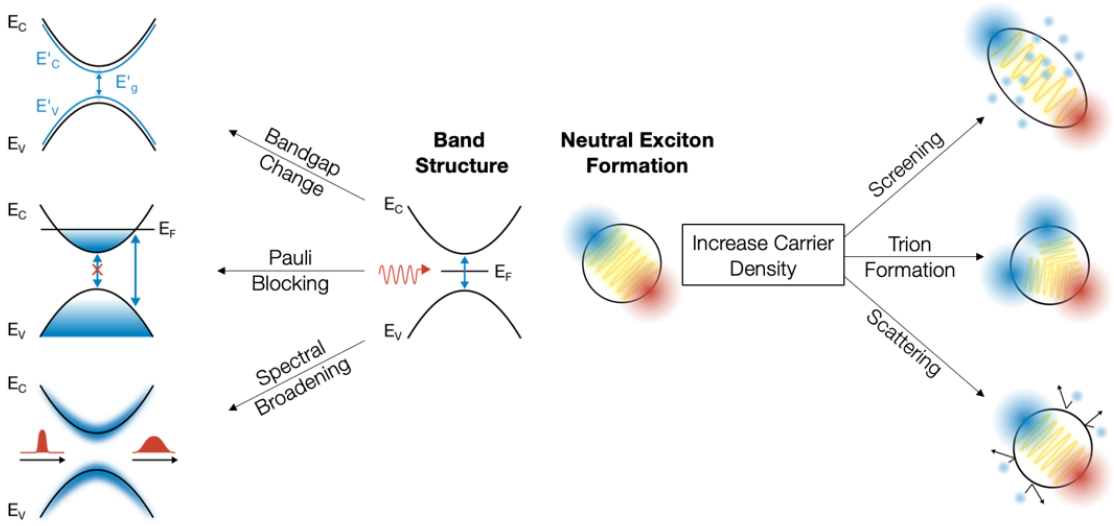

Figure S2.2. Electro-optic effects in TMDCs. Due to electrical gating, the carrier density increases, which results in a combination of effects on the exciton, including screening, scattering, and trion formation. These effects also result in changes in the band structure and allowed transitions for different Fermi levels.

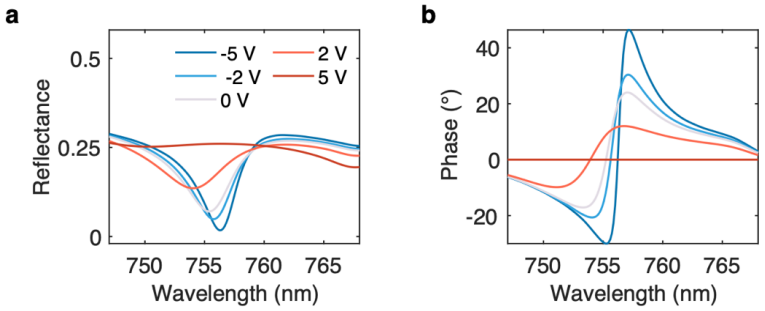

Figure S2.3. Simulated voltage-dependent spectra for y-polarization. (a) Reflectance spectra and (b) phase of the light scattered from the metasurface for different voltage for an $MoSe_2$ sample with quantum yield $\eta = 0.25$. Light polarization is parallel to the gold electrodes (y-polarization) using plane wave illumination and periodic boundary conditions. Corresponding beam steering result and analysis for $\eta = 0.5$ is shown in the main text Figure 3.2.

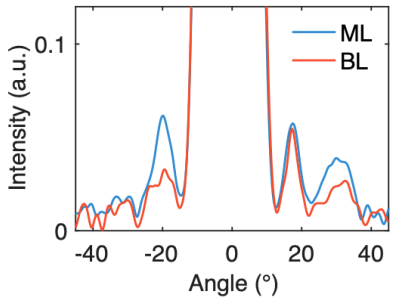

Figure S2.4. Measured deflection in bilayer $MoSe_2$. Reflected angular far field intensity for the monolayer (blue) and bilayer (red) regions at the exciton wavelength of 757 and 767 nm, respectively for V_1 = 5 V and V_3 = -5 V.

Supplementary Note S2.1: Material and Methods

Measurement Low temperature optical spectroscopy was performed using an attoDRY800 system, which allows for temperature control. The sample was mounted on a piezo-stage using Apiezon thermal grease and the stage was cooled by closed-cycle circulating liquid helium. For the optical characterization, broadband light from a supercontinuum laser (NKT SuperK Extreme) was impinged on the sample in a Köhler illumination configuration passing through a vacuum and low temperature compatible objective (NA = 0.82). The reflected light was collected by the same objective and directed to a CCD camera and a grating spectrometer (See Figure 3.5). For Fourier plane imaging, a Fourier plane was formed at the entrance slit of the spectrometer through a set of lenses.

Fabrication Samples were fabricated by mechanically exfoliating hBN and monolayer $MoSe_2$ from bulk crystals (hq-graphene and 2D semiconductors) onto polydimethylsiloxane (PDMS) stamps using blue Nitto tape. The hBN/$MoSe_2$/hBN heterostructure was then sequentially transferred from the PDMS to the patterned Au electrode array using the all-dry transfer technique. The Au electrode array and contact pads were fabricated with a sequential multistep process of electron beam lithography, evaporation, and lift-off, to allow for different thicknesses of the electrode array and

electric contact pads. To improve the adhesion of Au on SiO_2, a 2 nm thick Ti adhesion layer was used.

Simulations The numerical modeling of the nanostructures was carried out using a finite difference time domain (FDTD) method with the commercially available software *Lumerical*. The gate dependent reflection, phase and beam deflection (Figure 3.2) was simulated using periodic boundary conditions and a spatially coherent plane wave illumination. For the comparison between simulations and experiment (Figure 3.7), a gaussian illumination with a 24 μm beam diameter and perfectly matched layer boundary conditions were used. The effect of the numerical aperture of the imaging objective lens and the finite imaging aperture was accounted for through a set of Fourier transforms and spatial filtering in the Fourier and image plane. A constant refractive index $n = 1.45$ was used for thermal oxide and $n = 2.2$ for hBN. The smallest mesh refinement of 0.2 nm was used.

Supplementary Note S2.2: Discussion of electro-optic response in TMDCs

When the $MoSe_2$ is near the charge-neutral point, the optical response is strongly dominated by the neutral exciton resonance. We note our sample is intrinsically n-doped, and thus in our gating configuration the charge neutral point is defined as when the applied voltage is around -4 V to -5 V. As the voltage is tuned to positive or negative values, a two-dimensional electron gas (2DEG) forms at the interface of the $MoSe_2$ monolayer and bottom hBN. This effectively increases the carrier density and Fermi level of the $MoSe_2$, resulting in the following changes in the optical response:

- **Coulomb screening of exciton**: As the carrier density increases, the free carriers effectively screen the field between the electron-hole pair. This reduces the interaction strength of the dipole, which leads to a reduction in the exciton binding energy and lowers the oscillator strength or radiative rate.
- **Coulomb scattering of the exciton**: An increase in free carriers also results in the increase in probability of an exciton to elastically or inelastically scatter off an electron or hole. This leads to a reduction in the coherence lifetime of the exciton

and an increase in non-radiative processes, which results in spectral broadening corresponding to the excitonic transition.

- **Trions**: The probability of an exciton binding to a free charge to form a trion, or charged exciton, also increases. The trion peak is typically lower in energy than the exciton and is observed as a separate peak redshifted from the exciton peak. The oscillator strengths of trions are lower than the excitons, which can be seen from the lower steering efficiency at the trion resonance compared to the exciton resonance (Figure 3.8b).
- **Pauli blocking**: As the Fermi level increases into the conduction band (electron doping) or valence band (hole doping), the lowest optical transition gets blocked, resulting in a blue-shift in the absorption peak. This is observed from the spectral response in our voltage dependent steering efficiency in Figure 3.7.
- **Bandgap renormalization**: There can also be significant band-structure renormalization which leads to energy shifts in the absorption peak. This is typically observed by a red shift in the quasiparticle band gap. We note that this effect is cancelled out with the reduction in the binding energy and Pauli blocking, so this red shift is not directly observed with increase in carrier density here.

The listed effects are shown schematically in Figure S2.2 and the combined effect on the gate-dependent refractive index is shown in Figure S2.1. We note that there are also other effects that are typically observed in 2D semiconductors such as Stark shift where a vertical electric field can cause a reduction of the bandgap and red-shift the absorption peak. However, we believe this is a very weak effect in our gating scheme where a pure vertical displacement field in the absence of doping does not exist.

APPENDIX C: S3. SUPPORTING INFORMATION FOR CHAPTER 4

Supplementary Note 3.1: Electro-optic response in TMDCs

To electrically control the reflectance properties of our heterostructure devices, we control the carrier concentration in the TMDC with gate voltage. We first consider the carrier-dependent change in the complex refractive index in a monolayer $MoSe_2$.

Carrier Density Calculation

We calculate the carrier density by using a parallel plate capacitor model. In the one-layer $MoSe_2$ structure, the hBN is the dielectric capacitor, which enables the formation of a two-dimensional electron gas at the $MoSe_2$ monolayer. The capacitance is calculated as follows:

$$C = \frac{\epsilon_0 \epsilon_{hBN} A}{d} = \frac{Q}{\Delta V}$$

where, C = capacitance, ϵ_0 = vacuum permittivity, ϵ_{hBN} = relative dielectric permittivity of hBN[122] (ϵ_{hBN} = 4.7), A = area of the capacitor, d = thickness of the hBN flake, and Q is the charge. Thus, the charge density for electrons can be calculated from the capacitance per unit area between the silver back mirror and the $MoSe_2$ sample by:

$$n_e = \frac{Q}{A} = \frac{C}{A} * (V - V_{CNP}).$$

The charge neutral point, V_{CNP} = -5 V, is the typical gate voltage value associated with the hBN spacer thickness, d = 80 nm, that maximizes the exciton absorption. In our gating schematic, shown in Figure 4.1, when $V_g < V_{CNP}$, the sample is hole doped and for $V_g > V_{CNP}$, the sample is electron doped. In this work, we only consider electron doping (V > -5 V) and the conversion to carrier concentration for electrons is shown in Figure S3.1a.

Refractive Index Calculation

The dielectric function of $MoSe_2$ takes the form of a sum of Lorentz oscillators:

$$\epsilon = \epsilon_1 + i\epsilon_2 = \epsilon_\infty - \frac{\hbar c}{d_{MoSe_2}} \sum_j \frac{\hbar \gamma_{r_j}}{E_j (E - E_j + i\hbar \gamma_{nr_j}/2)}$$

where, ϵ_∞ is the background $MoSe_2$ dielectric constant, d_{MoSe_2} is the thickness of the monolayer, and E_j, γ_{r_j}, and γ_{nr_j} are the resonant energy, radiative, and nonradiative

emission rates of the j[th] oscillator, respectively. In our analysis, we model the dielectric function with a single oscillator corresponding to the A exciton for $MoSe_2$ and add a background dielectric constant, $\epsilon_\infty = 21$. Increasing the gate voltage and carrier density then modifies the radiative and non-radiative emission rates, and resonant energy (Figure S3.1b). Depending on the ratio of radiative and non-radiative rates, the $MoSe_2$ dielectric function takes a negative or positive value on resonance, yielding an epsilon-near-zero response and a tunable transition from metallic to dielectric near the exciton energy (Figure S3.1c and d).

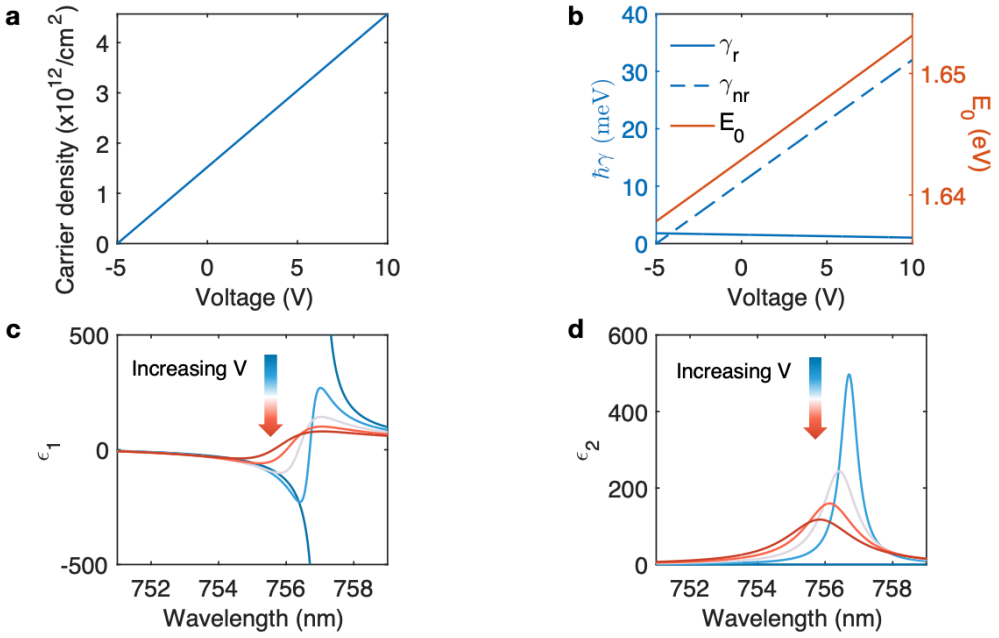

Figure S3.1. Voltage and carrier density dependent change of $MoSe_2$ dielectric function. (a) Conversion between voltage and carrier density of electrons in $MoSe_2$. (b) Effects of increasing voltage on the individual $MoSe_2$ exciton resonance parameters. (c,d) Voltage-dependent change in the real and imaginary part of the dielectric function, respectively.

Supplementary Note 3.2: Transfer Matrix Calculation for Complex Frequency Amplitude and Phase Response

The complex frequency response for the scattered amplitude and phase of multi-layer structures studied in the main text can be treated with the transfer matrix method to account

for the multiple reflections in our device. At normal incidence, the field in each layer can be decomposed into forward and backward waves that form the basis and can be computed by matrix multiplication where each matrix describes the light propagation at an interface between two materials. The (i+1)th amplitude can be related to the ith amplitude by the relation:

$$\underbrace{\begin{pmatrix} e^{ik_i z_i} & e^{-ik_i z_i} \\ k_i e^{ik_i z_i} & -k_i e^{-ik_i z_i} \end{pmatrix}}_{M_1} \begin{pmatrix} A_i \\ B_i \end{pmatrix} = \underbrace{\begin{pmatrix} e^{ik_{i+1} z_i} & e^{-ik_{i+1} z_i} \\ k_{i+1} e^{ik_{i+1} z_i} & -k_{i+1} e^{-ik_{i+1} z_i} \end{pmatrix}}_{M_2} \begin{pmatrix} A_{i+1} \\ B_{i+1} \end{pmatrix}$$

$$\begin{pmatrix} A_{i+1} \\ B_{i+1} \end{pmatrix} = J_i \begin{pmatrix} A_i \\ B_i \end{pmatrix} \; where \; J_i = M_2^{-1} M_1$$

$$\Rightarrow J_i = \frac{1}{2} \begin{pmatrix} e^{i(k_i - k_{i+1}) z_i} \left(1 + \frac{k_i}{k_{i+1}}\right) & e^{-i(k_i + k_{i+1}) z_i} \left(1 - \frac{k_i}{k_{i+1}}\right) \\ e^{i(k_i + k_{i+1}) z_i} \left(1 - \frac{k_i}{k_{i+1}}\right) & e^{-i(k_i - k_{i+1}) z_i} \left(1 + \frac{k_i}{k_{i+1}}\right) \end{pmatrix}$$

where k is the wavevector, z is the thickness, and i is the layer index. The wavevector k_i is scaled by the complex index of refraction $\tilde{n}_i = n_i + i\kappa_i$ of the material so that $k_i = \frac{2\pi \tilde{n}_i}{\lambda}$ and the frequency $\omega = \omega_r + i\omega_i$ is complex. Then, for N layers, we have:

$$\begin{pmatrix} t \\ 0 \end{pmatrix} = J_{N_{total}} \begin{pmatrix} 1 \\ r \end{pmatrix}, \quad where \quad J_{N_{total}} = J_N J_{N-1} \ldots J_2 J_1$$

and the reflectance and phase of the entire stack given by:

$$r = |r| e^{i\phi} \Rightarrow R = |r|^2.$$

Using the Lorentz oscillator model of the $MoSe_2$ dielectric function, we can then plot the complex frequency response of our device structure and show the effects of each exciton parameter on the spectral positions of the zero and pole. Figure S3.2a, S3.2b, and S3.2c show the effect of increasing the radiative, nonradiative, and resonance energy of the

exciton, respectively. As mentioned in the main text, an increase in the radiative rate results in a separation of the zero and poles across the real frequency axis. When the nonradiative rate is negative, corresponding to gain, (shown in the left panel of Figure 4.2b), the pole moves closer to the real axis. As we increase the nonradiative rate, corresponding to increasing loss, the zero and poles move towards the bottom half of the complex frequency plane below the real frequency axis. A blueshift in the resonance energy will result in a blueshift in the zero and pole along the real frequency axis.

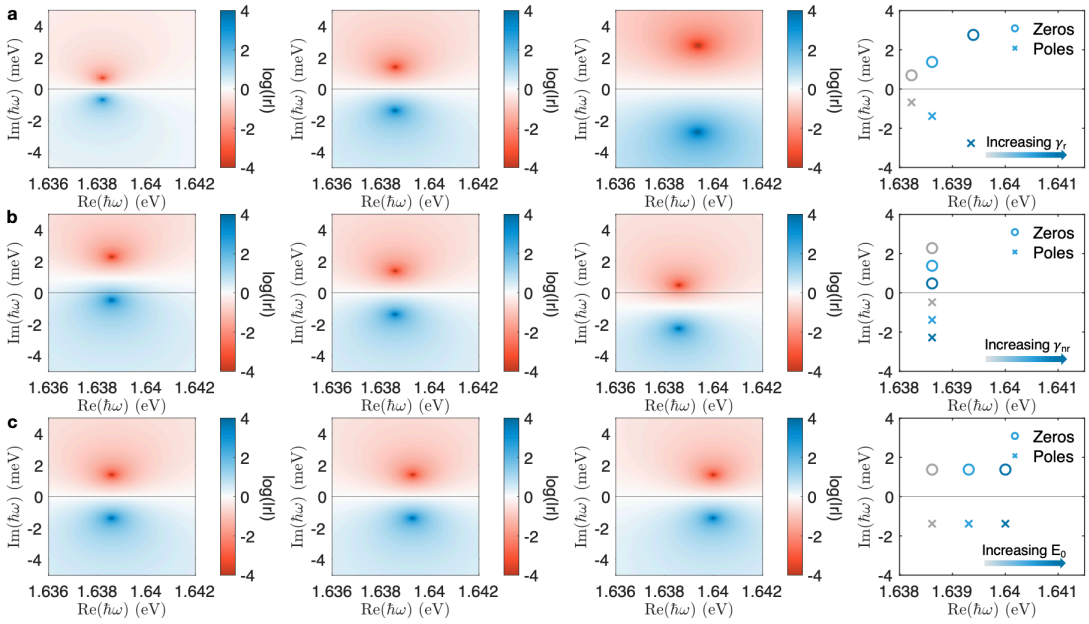

Figure S3.2. Effects of exciton parameters on zeros and poles. (a) Complex frequency planes for increasing (grey to dark blue) radiative rate, (b) nonradiative rate, and (c) resonance energy.

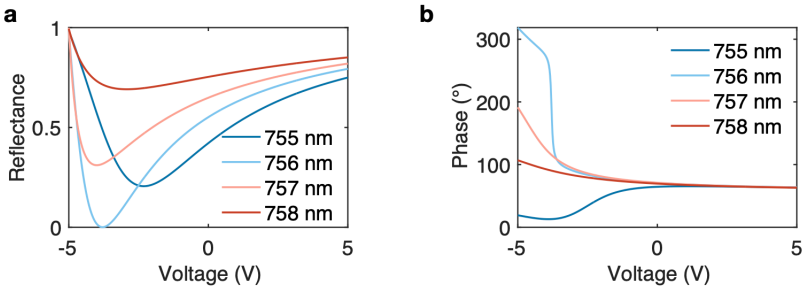

Figure S3.3. Voltage-dependent scattering response for single-layer $MoSe_2$. (a) Reflectance amplitude and (b) phase as a function of voltage for various wavelengths. The achievable gate-dependent phase shift is maximized for $\lambda_0 = 756\,nm$, where $\Delta\Phi = 252°$.

Label (From Figure 4.4a)	**n_1 ($x10^{12}/cm^2$)**	**n_2 ($x10^{12}/cm^2$)**	**n_3 ($x10^{12}/cm^2$)**	**Phase (°)**	**Reflectance**
1	0	0	0	-600	1
2	0.65	0	0	-437	0.46
3	0.12	0.06	0.03	-375	0
4	0.06	0.06	0.03	-272	0.1
5	0	0.01	0.07	-266	0.3
6	0.72	0.04	0.05	-120	0.41
7	0	0	0.65	-96	0.47
8	0.19	0.06	0.01	-26	0.04
9	0	0.65	0	118	0.99
10	0.65	0.65	0.65	191	0.69
11	0.32	0.32	0.32	201	0.52
12	0.61	0.07	0.07	233	0.4
13	0.19	0.06	0.03	277	0.04

Figure S3.4. Carrier concentration values of n_1, n_2, and n_3 used for the phase spectra for Figure 4.4a and the corresponding reflectance phase and amplitude values used for Figure 4.4b and 4.4c.

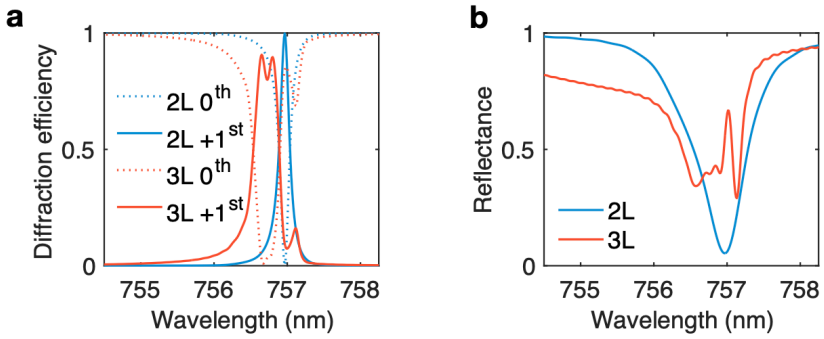

Figure S3.5. Beam steering for two- and three-layer $MoSe_2$ heterostructures. (a) Relative diffraction efficiency for the 0th order (dashed) and +1 order (solid) for the two-layer (blue) and three-layer (red) $MoSe_2$ structure from Figure 4.7e. The relative diffraction efficiencies for both structures are over 90%. (b) The total reflectance spectrum for the two-layer (blue) and three-layer (red) $MoSe_2$ structure, showing the total reflected power into the +1 order is much higher for the three-layer structure compared to the two-layer structure.

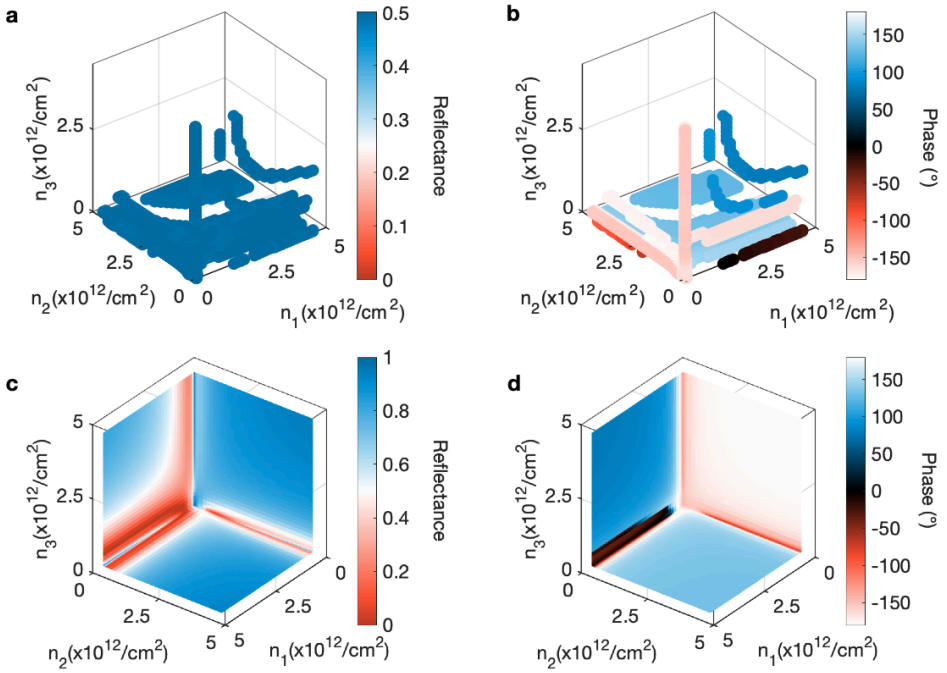

Figure S3.6. Gate-dependent reflectance amplitude and phase for three-layer $MoSe_2$ heterostructures. (a) Reflectance amplitude and (b) phase values through varying the carrier concentrations of three $MoSe_2$ layers where the reflectance is constant at 50% and the phase spans 2π. (c) Reflectance amplitude and (d) phase values projected on constant $n_1 = 0$, $n_2 = 0$, and $n_3 = 0$ planes.

BIBLIOGRAPHY

1. Yu, N. *et al.* Light Propagation with Phase Discontinuities: Generalized Laws of Reflection and Refraction. *Science.* **334**, 333–337 (2011).

2. Hsu, W.-L. *et al.* Review of Metasurfaces and Metadevices: Advantages of Different Materials and Fabrications. *Nanomaterials* **12**, 1973 (2022).

3. Biswas, S., Grajower, M. Y., Watanabe, K., Taniguchi, T. & Atwater, H. A. Broadband electro-optic polarization conversion with atomically thin black phosphorus. *Science.* **374**, 448–453 (2021).

4. van de Groep, J. *et al.* Exciton resonance tuning of an atomically thin lens. *Nat. Photonics* **14**, 426–430 (2020).

5. Li, M., Biswas, S., Hail, C. U. & Atwater, H. A. Refractive Index Modulation in Monolayer Molybdenum Diselenide. *Nano Lett.* **21**, 7602–7608 (2021).

6. Li, M., Hail, C. U., Biswas, S. & Atwater, H. A. Excitonic Beam Steering in an Active van der Waals Metasurface. *Nano Lett.* **23**, 2771–2777 (2023).

7. Lin, H. *et al.* Diffraction-limited imaging with monolayer 2D material-based ultrathin flat lenses. *Light Sci. Appl.* **9**, 137 (2020).

8. Mak, K. F., Lee, C., Hone, J., Shan, J. & Heinz, T. F. Atomically Thin MoS_2: A New Direct-Gap Semiconductor. *Phys. Rev. Lett.* **105**, 136805 (2010).

9. Scuri, G. *et al.* Large Excitonic Reflectivity of Monolayer $MoSe_2$ Encapsulated in Hexagonal Boron Nitride. *Phys. Rev. Lett.* **120**, 37402 (2018).

10. Back, P., Zeytinoglu, S., Ijaz, A., Kroner, M. & Imamoğlu, A. Realization of an electrically tunable narrow-bandwidth atomically thin mirror using monolayer $MoSe_2$. *Phys. Rev. Lett.* **120**, 037401 (2018).

11. Yu, Y. *et al.* Giant Gating Tunability of Optical Refractive Index in Transition Metal Dichalcogenide Monolayers. *Nano Lett.* **17**, 3613–3618 (2017).

12. Andersen, T. I. *et al.* Beam steering at the nanosecond time scale with an atomically thin reflector. *Nat. Commun.* **13**, 3431 (2022).

13. Butler, S. Z. *et al.* Progress, Challenges, and Opportunities in Two-Dimensional Materials Beyond Graphene. *ACS Nano* **7**, 2898–2926 (2013).

14. Wang, Q. H., Kalantar-Zadeh, K., Kis, A., Coleman, J. N. & Strano, M. S. Electronics and optoelectronics of two-dimensional transition metal dichalcogenides. *Nat. Nanotechnol.* **7**, 699–712 (2012).

15. Moody, G. *et al.* Intrinsic homogeneous linewidth and broadening mechanisms of excitons in monolayer transition metal dichalcogenides. *Nat. Commun.* **6**, 8315 (2015).

16. Splendiani, A. *et al.* Emerging Photoluminescence in Monolayer MoS_2. *Nano Lett.* **10**, 1271–1275 (2010).

17. Stier, A. V, Wilson, N. P., Clark, G., Xu, X. & Crooker, S. A. Probing the Influence of Dielectric Environment on Excitons in Monolayer WSe_2: Insight from High Magnetic Fields. *Nano Lett.* **16**, 7054–7060 (2016).

18. Stier, A. V. *et al.* Magnetooptics of Exciton Rydberg States in a Monolayer Semiconductor. *Phys. Rev. Lett.* **120**, 57405 (2018).

19. Raja, A. *et al.* Coulomb engineering of the bandgap and excitons in two-dimensional materials. *Nat. Commun.* **8**, 15251 (2017).

20. Aslan, O. B., Deng, M. & Heinz, T. F. Strain tuning of excitons in monolayer WSe_2. *Phys. Rev. B* **98**, 115308 (2018).

21. Lloyd, D. *et al.* Correction to Band Gap Engineering with Ultralarge Biaxial Strains in Suspended Monolayer MoS2. *Nano Lett.* **19**, 7548 (2019).

22. Olivieri, A. *et al.* Plasmonic Nanostructured Metal–Oxide–Semiconductor Reflection Modulators. *Nano Lett.* **15**, 2304–2311 (2015).

23. Park, J., Kang, J.-H., Liu, X. & Brongersma, M. L. Electrically Tunable Epsilon-Near-Zero (ENZ) Metafilm Absorbers. *Sci. Rep.* **5**, 15754 (2015).

24. Jun, Y. C. *et al.* Epsilon-Near-Zero Strong Coupling in Metamaterial-Semiconductor Hybrid Structures. *Nano Lett.* **13**, 5391–5396 (2013).

25. Dabidian, N. *et al.* Electrical Switching of Infrared Light Using Graphene Integration with Plasmonic Fano Resonant Metasurfaces. *ACS Photonics* **2**, 216–227 (2015).

26. Yao, Y. *et al.* Broad Electrical Tuning of Graphene-Loaded Plasmonic Antennas. *Nano Lett.* **13**, 1257–1264 (2013).

27. Hail, C. U., Michel, A.-K. U., Poulikakos, D. & Eghlidi, H. Optical Metasurfaces: Evolving from Passive to Adaptive. *Adv. Opt. Mater.* **7**, 1801786 (2019).

28. Huang, Y.-W. *et al.* Gate-Tunable Conducting Oxide Metasurfaces. *Nano Lett.* **16**, 5319–5325 (2016).

29. Shirmanesh, G. K., Sokhoyan, R., Wu, P. C. & Atwater, H. A. Electro-optically Tunable Multifunctional Metasurfaces. *ACS Nano* **14**, 6912–6920 (2020).

30. Kafaie Shirmanesh, G., Sokhoyan, R., Pala, R. A. & Atwater, H. A. Dual-Gated Active Metasurface at 1550 nm with Wide (>300°) Phase Tunability. *Nano Lett.* **18**, 2957–2963 (2018).

31. Zhou, Y. *et al.* Probing dark excitons in atomically thin semiconductors via near-field coupling to surface plasmon polaritons. *Nat. Nanotechnol.* **12**, 856–860 (2017).

32. Ajayi, O. A. *et al.* Approaching the intrinsic photoluminescence linewidth in transition metal dichalcogenide monolayers. *2D Mater.* **4**, 31011 (2017).

33. Cadiz, F. *et al.* Excitonic Linewidth Approaching the Homogeneous Limit in MoS_2-Based van der Waals Heterostructures. *Phys. Rev. X* **7**, 21026 (2017).

34. Datta, I. *et al.* Low-loss composite photonic platform based on 2D semiconductor monolayers. *Nat. Photonics* **14**, 256–262 (2020).

35. Dean, C. R. *et al.* Boron nitride substrates for high-quality graphene electronics. *Nat. Nanotechnol.* **5**, 722–726 (2010).

36. Wang, Z., Zhao, L., Mak, K. F. & Shan, J. Probing the Spin-Polarized Electronic Band Structure in Monolayer Transition Metal Dichalcogenides by Optical Spectroscopy. *Nano Lett.* **17**, 740–746 (2017).

37. Sidler, M. *et al.* Fermi polaron-polaritons in charge-tunable atomically thin semiconductors. *Nat. Phys.* **13**, 255–261 (2017).

38. Ross, J. S. *et al.* Electrical control of neutral and charged excitons in a monolayer semiconductor. *Nat. Commun.* **4**, 1474 (2013).

39. Qiu, D. Y., da Jornada, F. H. & Louie, S. G. Optical Spectrum of MoS_2: Many-Body Effects and Diversity of Exciton States. *Phys. Rev. Lett.* **111**, 216805 (2013).

40. Gao, S., Liang, Y., Spataru, C. D. & Yang, L. Dynamical Excitonic Effects in Doped Two-Dimensional Semiconductors. *Nano Lett.* **16**, 5568–5573 (2016).

41. Van Tuan, D. *et al.* Probing many-body interactions in monolayer transition-metal dichalcogenides. *Phys. Rev. B* **99**, 85301 (2019).

42. Goldstein, T. *et al.* Ground and excited state exciton polarons in monolayer $MoSe_2$. *J. Chem. Phys.* **153**, (2020).

43. Li, Y. *et al.* Measurement of the optical dielectric function of monolayer transition-metal dichalcogenides: MoS_2, $MoSe_2$, WS_2, and WSe_2. *Phys. Rev. B* **90**, 205422 (2014).

44. Kravets, V. G. *et al.* Measurements of electrically tunable refractive index of MoS_2 monolayer and its usage in optical modulators. *npj 2D Mater. Appl.* **3**, 36 (2019).

45. Hsu, C. *et al.* Thickness-Dependent Refractive Index of 1L, 2L, and 3L MoS_2, $MoSe_2$, WS_2, and WSe_2. *Adv. Opt. Mater.* **7**, 1900239 (2019).

46. Hecht, E. *Optics*. (Addison-Wesley, 2002).

47. Sherrott, M. C. *et al.* Anisotropic Quantum Well Electro-Optics in Few-Layer Black Phosphorus. *Nano Lett.* **19**, 269–276 (2019).

48. Zhou, Y. *et al.* Controlling Excitons in an Atomically Thin Membrane with a Mirror. *Phys. Rev. Lett.* **124**, 27401 (2020).

49. Sun, S. *et al.* High-Efficiency Broadband Anomalous Reflection by Gradient Meta-Surfaces. *Nano Lett.* **12**, 6223–6229 (2012).

50. Lin, D., Fan, P., Hasman, E. & Brongersma, M. L. Dielectric gradient metasurface optical elements. *Science.* **345**, 298–302 (2014).

51. Paniagua-Domínguez, R. *et al.* A Metalens with a Near-Unity Numerical Aperture. *Nano Lett.* **18**, 2124–2132 (2018).

52. Hail, C. U., Poulikakos, D. & Eghlidi, H. High-Efficiency, Extreme-Numerical-Aperture Metasurfaces Based on Partial Control of the Phase of Light. *Adv. Opt. Mater.* **6**, 1–8 (2018).

53. Ni, X., Kildishev, A. V. & Shalaev, V. M. Metasurface holograms for visible light. *Nat. Commun.* **4**, (2013).

54. Zheng, G. *et al.* Metasurface holograms reaching 80% efficiency. *Nat. Nanotechnol.* **10**, 308–312 (2015).

55. Holsteen, A. L., Cihan, A. F. & Brongersma, M. L. Temporal color mixing and dynamic beam shaping with silicon metasurfaces. *Science.* **365**, 257–260 (2019).

56. Zhang, X. *et al.* Reconfigurable Metasurface for Image Processing. *Nano Lett.* **21**, 8715–8722 (2021).

57. Park, J. *et al.* All-solid-state spatial light modulator with independent phase and amplitude control for three-dimensional LiDAR applications. *Nat. Nanotechnol.* **16**, 69–76 (2021).

58. Komar, A. *et al.* Dynamic Beam Switching by Liquid Crystal Tunable Dielectric Metasurfaces. *ACS Photonics* **5**, 1742–1748 (2018).

59. Zhang, Y. *et al.* Electrically reconfigurable non-volatile metasurface using low-loss optical phase-change material. *Nat. Nanotechnol.* **16**, 661–666 (2021).

60. Wang, Y. *et al.* Electrical tuning of phase-change antennas and metasurfaces. *Nat. Nanotechnol.* **16**, 667–672 (2021).

61. Kim, Y. *et al.* Phase Modulation with Electrically Tunable Vanadium Dioxide Phase-Change Metasurfaces. *Nano Lett.* **19**, 3961–3968 (2019).

62. Lewi, T., Evans, H. A., Butakov, N. A. & Schuller, J. A. Ultrawide Thermo-optic Tuning of PbTe Meta-Atoms. *Nano Lett.* **17**, 3940–3945 (2017).

63. Sherrott, M. C. *et al.* Experimental Demonstration of >230° Phase Modulation in Gate-Tunable Graphene–Gold Reconfigurable Mid-Infrared Metasurfaces. *Nano Lett.* **17**, 3027–3034 (2017).

64. Li, S.-Q. *et al.* Phase-only transmissive spatial light modulator based on tunable

dielectric metasurface. *Science.* **364**, 1087–1090 (2019).

65. Wu, P. C. *et al.* Dynamic beam steering with all-dielectric electro-optic III–V multiple-quantum-well metasurfaces. *Nat. Commun.* **10**, 1–9 (2019).

66. Yin, X. *et al.* Beam switching and bifocal zoom lensing using active plasmonic metasurfaces. *Light Sci. Appl.* **6**, 1–7 (2017).

67. Nicholls, L. H. *et al.* Ultrafast synthesis and switching of light polarization in nonlinear anisotropic metamaterials. *Nat. Photonics* **11**, 628–633 (2017).

68. Epstein, I. *et al.* Near-Unity Light Absorption in a Monolayer WS_2 Van der Waals Heterostructure Cavity. *Nano Lett.* **20**, 3545–3552 (2020).

69. Brongersma, M. L. The road to atomically thin metasurface optics. *Nanophotonics* **10**, 643–654 (2020).

70. Chen, C. *et al.* Widely tunable mid-infrared light emission in thin-film black phosphorus. *Sci. Adv.* **6**, eaay6134 (2022).

71. Xie, S., Zhu, H., Li, M. & Bulović, V. Voltage-controlled reversible modulation of colloidal quantum dot thin film photoluminescence. *Appl. Phys. Lett.* **120**, 211104 (2022).

72. Rowland, C. E. *et al.* Electric Field Modulation of Semiconductor Quantum Dot Photoluminescence: Insights Into the Design of Robust Voltage-Sensitive Cellular Imaging Probes. *Nano Lett.* **15**, 6848–6854 (2015).

73. Su, R. *et al.* Perovskite semiconductors for room-temperature exciton-polaritonics. *Nat. Mater.* **20**, 1315–1324 (2021).

74. Blancon, J.-C. *et al.* Extremely efficient internal exciton dissociation through edge states in layered 2D perovskites. *Science.* **355**, 1288–1292 (2017).

75. Epstein, I. *et al.* Highly confined in-plane propagating exciton-polaritons on monolayer semiconductors. *2D Mater.* **7**, (2020).

76. Arora, A., Nogajewski, K., Molas, M., Koperski, M. & Potemski, M. Exciton band structure in layered $MoSe_2$: from a monolayer to the bulk limit. *Nanoscale* **7**, 20769–20775 (2015).

77. Velický, M. *et al.* Mechanism of Gold-Assisted Exfoliation of Centimeter-Sized Transition-Metal Dichalcogenide Monolayers. *ACS Nano* **12**, 10463–10472 (2018).

78. Liu, F. *et al.* Disassembling 2D van der Waals crystals into macroscopic monolayers and reassembling into artificial lattices. *Science.* **367**, 903–906 (2020).

79. Amani, M. *et al.* Recombination Kinetics and Effects of Superacid Treatment in Sulfur- and Selenium-Based Transition Metal Dichalcogenides. *Nano Lett.* **16**, 2786–2791 (2016).

80. Kim, H., Uddin, S. Z., Higashitarumizu, N., Rabani, E. & Javey, A. Inhibited nonradiative decay at all exciton densities in monolayer semiconductors. *Science.* **373**, 448–452 (2021).

81. Chen, H. T., Taylor, A. J. & Yu, N. A review of metasurfaces: Physics and applications. *Reports Prog. Phys.* **79**, (2016).

82. Kamali, S. M., Arbabi, E., Arbabi, A. & Faraon, A. A review of dielectric optical metasurfaces for wavefront control. *Nanophotonics* **7**, 1041–1068 (2018).

83. Yu, N. & Capasso, F. Flat optics with designer metasurfaces. *Nat. Mater.* **13**, 139–150 (2014).

84. Overvig, A. & Alù, A. Diffractive Nonlocal Metasurfaces. *Laser Photonics Rev.* **16**, 1–16 (2022).

85. Yang, J., Gurung, S., Bej, S., Ni, P. & Howard Lee, H. W. Active optical metasurfaces: Comprehensive review on physics, mechanisms, and prospective applications. *Reports Prog. Phys.* **85**, (2022).

86. Shaltout, A. M., Shalaev, V. M. & Brongersma, M. L. Spatiotemporal light control with active metasurfaces. *Science.* **364**, (2019).

87. Thureja, P. *et al.* Toward a universal metasurface for optical imaging, communication, and computation. *Nanophotonics* **11**, 3745–3768 (2022).

88. Dorrah, A. H. & Capasso, F. Tunable structured light with flat optics. *Science.* **376**, (2022).

89. Li, L., Zhao, H., Liu, C., Li, L. & Cui, T. J. Intelligent metasurfaces: control, communication and computing. *eLight* **2**, (2022).

90. Avayu, O., Almeida, E., Prior, Y. & Ellenbogen, T. Composite functional metasurfaces for multispectral achromatic optics. *Nat. Commun.* **8**, 1–7 (2017).

91. Arbabi, A., Horie, Y., Bagheri, M. & Faraon, A. Dielectric metasurfaces for complete control of phase and polarization with subwavelength spatial resolution and high transmission. *Nat. Nanotechnol.* **10**, 937–943 (2015).

92. Khorasaninejad, M. & Capasso, F. Broadband Multifunctional Efficient Meta-Gratings Based on Dielectric Waveguide Phase Shifters. *Nano Lett.* **15**, 6709–6715 (2015).

93. Ren, H. *et al.* Complex-amplitude metasurface-based orbital angular momentum holography in momentum space. *Nat. Nanotechnol.* **15**, 948–955 (2020).

94. Yuan, Y. *et al.* Independent phase modulation for quadruplex polarization channels enabled by chirality-assisted geometric-phase metasurfaces. *Nat. Commun.* **11**, 1–9 (2020).

95. Khorasaninejad, M. *et al.* Metalenses at visible wavelengths: Diffraction-limited focusing and subwavelength resolution imaging. *Science.* **352**, 1190–1194 (2016).

96. Colom, R. *et al.* Crossing of the Branch Cut: The Topological Origin of a Universal 2π-Phase Retardation in Non-Hermitian Metasurfaces. *Laser Photonics Rev.* **17**, 1–30 (2023).

97. Berkhout, A. & Koenderink, A. F. Perfect Absorption and Phase Singularities in Plasmon Antenna Array Etalons. *ACS Photonics* **6**, 2917 (2019).

98. Kravets, V. G. *et al.* Singular Phase Nano-Optics in Plasmonic Metamaterials for Label-Free Single-Molecule Detection. *Nat. Mater.* **12**, 304 (2013).

99. Elsawy, M. *et al.* Universal Active Metasurfaces for Ultimate Wavefront Molding by Manipulating the Reflection Singularities. *Laser Photonics Rev.* **17**, (2023).

100. Li, Q. *et al.* A Purcell-enabled monolayer semiconductor free-space optical modulator. *Nat. Photonics* **17**, 897–903 (2023).

101. Mikheeva, E. *et al.* Asymmetric Phase Modulation of Light with Parity-Symmetry Broken Metasurfaces. *Optica* **10**, 1287 (2023).

102. Qu, C. *et al.* Tailor the Functionalities of Metasurfaces Based on a Complete Phase Diagram. *Phys. Rev. Lett.* **115**, 235503 (2015).

103. Overvig, A. C., Malek, S. C. & Yu, N. Multifunctional Nonlocal Metasurfaces. *Phys. Rev. Lett.* **125**, 17402 (2020).

104. Walling, M. A., Novak, J. A. & Shepard, J. R. E. Quantum Dots for Live Cell and In Vivo Imaging. *International Journal of Molecular Sciences* **10**, 441–491 (2009).

105. Livache, C. *et al.* A colloidal quantum dot infrared photodetector and its use for intraband detection. *Nat. Commun.* **10**, 2125 (2019).

106. Carey, G. H. *et al.* Colloidal Quantum Dot Solar Cells. *Chem. Rev.* **115**, 12732–12763 (2015).

107. Tepliakov, N. V, Leonov, M. Y., Baranov, A. V, Fedorov, A. V & Rukhlenko, I. D. Quantum theory of electroabsorption in semiconductor nanocrystals. *Opt. Express* **24**, A52–A57 (2016).

108. Park, S.-J., Link, S., Miller, W. L., Gesquiere, A. & Barbara, P. F. Effect of electric field on the photoluminescence intensity of single CdSe nanocrystals. *Chem. Phys.* **341**, 169–174 (2007).

109. Menéndez-Proupin, E. & Trallero-Giner, C. Electric-field and exciton structure in CdSe nanocrystals. *Phys. Rev. B* **69**, 125336 (2004).

110. Galland, C. *et al.* Two types of luminescence blinking revealed by spectroelectrochemistry of single quantum dots. *Nature* **479**, 203–207 (2011).

111. Efros, A. L. & Nesbitt, D. J. Origin and control of blinking in quantum dots. *Nat. Nanotechnol.* **11**, 661–671 (2016).

112. Moebius, M. *et al.* Using quantum dot photoluminescence for load detection. *AIP Adv.* **6**, 85309 (2016).

113. Korlacki, R., Saraf, R. F. & Ducharme, S. Electrical control of photoluminescence wavelength from semiconductor quantum dots in a ferroelectric polymer matrix. *Appl. Phys. Lett.* **99**, 153112 (2011).

114. Nirmal, M. *et al.* Observation of the 'Dark Exciton' in CdSe Quantum Dots. *Phys. Rev. Lett.* **75**, 3728–3731 (1995).

115. Panfil, Y. E., Oded, M. & Banin, U. Colloidal Quantum Nanostructures: Emerging Materials for Display Applications. *Angew. Chemie Int. Ed.* **57**, 4274–4295 (2018).

116. Berkinsky, D. B. *et al.* Narrow Intrinsic Line Widths and Electron–Phonon Coupling of InP Colloidal Quantum Dots. *ACS Nano* **17**, 3598–3609 (2023).

117. Gellen, T. A., Lem, J. & Turner, D. B. Probing Homogeneous Line Broadening in CdSe Nanocrystals Using Multidimensional Electronic Spectroscopy. *Nano Lett.* **17**, 2809–2815 (2017).

118. Dement, D. B., Puri, M. & Ferry, V. E. Determining the Complex Refractive Index of Neat CdSe/CdS Quantum Dot Films. *J. Phys. Chem. C* **122**, 21557–21568 (2018).

119. Markel, V. A. Introduction to the Maxwell Garnett approximation: tutorial. *J. Opt. Soc. Am. A* **33**, 1244–1256 (2016).

120. Bruggeman, D. A. G. Berechnung verschiedener physikalischer Konstanten von heterogenen Substanzen. I. Dielektrizitätskonstanten und Leitfähigkeiten der Mischkörper aus isotropen Substanzen. *Ann. Phys.* **416**, 636–664 (1935).

121. Koshelev, K. *et al.* Subwavelength dielectric resonators for nonlinear nanophotonics. *Science.* **367**, 288–292 (2020).

122. Levinshtein, M. E., Rumyantsev, S. L. & Shur, M. S. *Properties of Advanced Semiconductor Materials: GaN, AIN, InN, BN, SiC, SiGe*. (Wiley, 2001).